RADAR DETECTION OF BURIED LANDMINES IN FIELD SOILS

by

Timothy W. Miller

Submitted in Partial Fulfillment of the Requirements of the Degree of Master of Science
in Hydrology

August 2002

New Mexico Institute of Mining and Technology
Socorro, New Mexico

ABSTRACT

The contrast in the dielectric constant between a landmine and the surrounding soil is one of the most important parameters to be considered when using ground penetrating radar (GPR) for landmine detection. For most geologic materials the dielectric constant (relative permittivity) lies within a range of 3-30, with dry sand at the lower end of this range at about 3-5. Nonmetallic antitank landmines have dielectric constants within a range of about 3-10 depending on the type of material they are composed of and the presence of minor metallic components. Metallic landmines have a much higher dielectric constant, approaching infinity since they are conductors of electricity. In previous work, a MATLAB model was developed that is able to predict whether or not field conditions are appropriate for use of GPR instruments. In this study the predictions of this model are validated using GPR in different field soils and at various soil water contents. Three soils were chosen based on their sand, silt and clay contents. To vary the water content of the field soils, a sprinkler system was designed to uniformly water the study areas. Time domain reflectometry (TDR) probes were used to measure the soil water content at each site and GPR profiles were collected under dry, intermediate, and wet field soil conditions. GPR data from the sand and silt soils provide convincing evidence that increasing the soil water content above a nonmetallic landmine improves detections. Data for the clay soils suggests that under elevated soil water conditions detections of buried landmines are not improved; instead radar images in these soils become worse with increasing soil water content. Data suggests that detections of metallic landmines also degrades with increasing soil water content. The field data are in agreement with the model predictions.

ACKNOWLEDGMENTS

This work is funded by a grant from the Army Research Office (Project 38830-EL-LMD). I would like to thank Drs. Brian Borchers, Jan Hendrickx, Rob Bowman Harold Tobin and Russell Harmon for their valuable advice and support.

TABLE OF CONTENTS

LIST OF TABLES

LIST OF FIGURES

1 - INTRODUCTION

Sixty-five to 110 million landmines are believed to be scattered throughout 62 countries of the world, with Afghanistan, Angola, and Cambodia together totaling about 28 million mines (US Department of State, 1994). Detection and removal of these landmines is difficult because of the many variables involved, including soil type, climate, topography, and vegetation. Minefields are designed to be very complex since military engineers are taught to integrate minefields with natural obstacles such as steep slopes, watercourses, ditches, and dense vegetation (Ackenhusen et al., 2001). Because landmines are so difficult to detect, most landmines remain buried for many years and continue to threaten the people in these countries. The expense of de-mining is also an important factor hindering landmine removal. With a cost estimated at $300 to $1000 per removal of each mine, the total cost for de-mining these countries is staggering (Ackenhusen et al., 2001).

There are many sensors that have been developed for use in the detection of metallic and non-metallic landmines. The following list includes the most up-to-date sensors in mine detection: Visible Broadband, Broadband Infrared, Active Thermal Sensing, Spectral, Polarimetric, Streak-Tube Imaging LIDAR, Acoustic-Excited Laser Vibrometry, Sonar, Electromagnetic Induction, Magnetometer, Passive Microwave Radiometry, Close-In Ground Penetrating Radar, Stand-off Ground Penetrating Radar, Sensing of Water Wave Disturbances, Nuclear Quadrupole Resonance, Electro/Chemical

Detection, and Penetrating Radiation. All of these sensors can be referenced in Ackenhusen et al. (2001) for a complete assessment of the sensors performance under many environmental conditions and with various mine types. Electromagnetic induction sensors work well for metallic landmines due to the high electrical conductivity of these types of landmines (Ackenhusen et al., 2001). However, newer mines are composed of nonmetallic parts, which have essentially zero electrical conductivity and can elude many electromagnetic conductivity based sensors. Ultra-wideband-frequency-modulated-continuous-wave-radar has proven to be a useful sensor for detecting plastic anti-personnel landmines buried at shallow depths (Koh, 2000). These types of sensors depend more on the relative dielectric properties of the landmine-soil environment and less on the electrical conductivity of the landmine. The ground penetrating radar (GPR) system is one of the most widely used sensors of this sort. It has been used for many subsurface explorations including but not limited to the following: groundwater investigations, contaminant plume mapping, location of buried fuel tanks, ice sheet thickness mapping, permafrost investigations, integrity test of building materials, and even location of ancient grave sites (Reynolds, 1997).

A ground penetrating radar system utilizes the contrast in dielectric constants between the object that is to be detected and the material the radar wave passes through. Reflections are produced as the GPR encounters interfaces between objects with large dielectric contrast. In landmine investigations, the radar signals are passing through soil, which is a three-phase material containing solids, water, and air. The soil can also contain non-aqueous phase liquids in the case of contaminated vadose zones, which may introduce a fourth phase. Saline soils can be considered a good example of contaminated soils and radar response in these types of soils will also be discussed in this thesis.

Because the physical properties of soils are different, the speed of the radar waves are affected differently depending on the overall bulk density, texture, and soil water content (Hallikainen et al., 1985; Dobson et al., 1985; Topp et al., 1980; Wang and Schmugge, 1980). Reynolds (1997) states that the electromagnetic properties of materials are related to their composition and water content, both of which exert the main control over the speed of radar wave propagation and the attenuation of electromagnetic waves in materials. Because the electrical characteristics of a soil can be affected by these properties, they must be investigated prior to the use of radar-based equipment for landmine detection. Borchers et al. (2000) developed a computer model that predicts the soil electrical properties based on the soil dielectric properties. This model combines empirical equations from the literature and fundamental soil physics equations to predict ideal soil conditions for landmine detection using ground penetrating radar.

The goal of this study is to test a ground penetrating radar system using field soils found in Socorro, New Mexico and Yuma, Arizona and compare these results with model predictions. In order to place this study in context, a brief literature review follows presenting factors that researchers have determined to affect radar response in soils.

Effects of Soil Water Variability on Radar Response

Due to climatic and weather conditions the water content of the soil around a landmine can change dramatically within the course of hours, days, and years (Das et al., 2000; Borchers et al., 1999; Hendrickx et al., 1990). This variability in soil water content around the landmine can strongly effect landmine detection. Topp et al. (1980) studied the dependence of apparent dielectric constant on the volumetric water content of different soil mixtures. In their study they chose a radar system with a 1-MHz to 1-GHz variable frequency range. A series of 18 different experiments were carried out to determine the influence of selected parameters on the relationship between water content and the apparent dielectric constant (Topp et al., 1980). For these experiments the apparent dielectric constant was measured, which assumed that the electrical loss was insignificant and that the apparent dielectric constant was approximately equal to the real part (See Equation (6)) of the dielectric constant (Topp et al., 1980). Since the effects of electrical loss existed in their estimate of the real part of the dielectric constant (ε'), they called the measured dielectric constant an apparent dielectric constant (ε_a) (Topp et al., 1980). Thus for low-loss, nearly homogenous materials it is assumed that:

$$\varepsilon' \approx \varepsilon_a \tag{1}$$

From their experiments using many different soil types they were able to find the following empirical relationship between the apparent dielectric constant (ε_a) and volumetric soil water content (θ).

$$\varepsilon_a = 3.03 + 9.3\,\theta + 146.0\,\theta^2 - 76.7\,\theta^3 \tag{2}$$

Effects of Bound Water on Radar Response

To further the attempts at modeling the dielectric constant of soils, Dobson et al. (1985) studied the effects of bound water on the dielectric constant of soils. If the soil matrix is examined on the molecular level it is evident that there are water molecules in the pores of the soil matrix and there are water molecules attached to the mineral grains.

These attached water molecules in the past have been considered insignificant in attempts at modeling the microwave dielectric behavior of soil water mixtures as functions of increasing water content. However, in the Dobson et al. (1985) study they modeled the bound and free water layers using Stern-Gouy double-layer theory (Mitchell, 1976). A four-component mixing model was used to estimate the dielectric constant for each of the five soils used in the study which included the following: Sandy Loam (51.51% sand, 35.06% silt, and 13.43% clay), Loam (41.96% sand, 49.51% silt, and 8.53% clay), Silt Loam (30.63% sand, 55.89% silt, and 13.48% clay), Silt Loam (17.16% sand, 63.84% silt, and 19% clay), and Silty Clay (5.02% sand, 47.38% silt, and 47.38% clay) (See Figure 1.1) between 1.4 and 18 GHz (Dobson et al., 1985). The four-component mixing model has inputs for the volume of free water (Gouy Layer) and the bound water (Stern Layer).

$$\varepsilon_m = \frac{3\varepsilon_S + 2V_{fw}\left(\varepsilon_{fw} - \varepsilon_S\right) + 2V_{bw}\left(\varepsilon_{bw} - \varepsilon_S\right) + 2V_a\left(\varepsilon_a - \varepsilon_S\right)}{3 + V_{fw}\left(\frac{\varepsilon_S}{\varepsilon_{fw}} - 1\right) + V_{bw}\left(\frac{\varepsilon_S}{\varepsilon_{bw}} - 1\right) + V_a\left(\frac{\varepsilon_S}{\varepsilon_a} - 1\right)} \tag{3}$$

The general form of their four-component mixing model for the dielectric constant of the mixture ε_m is seen in Equation (3), where V refers to the volume fractions of the inclusions and the subscripts *fw*, *bw*, and *a* are for the free water, bound water, and air component respectively.

Incorporating the fractions of bound and free water into the estimate for the complex dielectric constant of a soil-water mixture did improve the fit of the predicted curve to that of the actual measured data. The four component mixing model improved the r-squared values from 0.982 to 0.985 and the standard error estimate from 0.87 to 0.93 for all the 809 measurements. However, use of this four-component mixing model

Figure 1.1 USDA classification of the five soils from Dobson et al. (1985) labeled field 1-5 and four soils from Peplinski et al. (1995) labeled field 6-9.

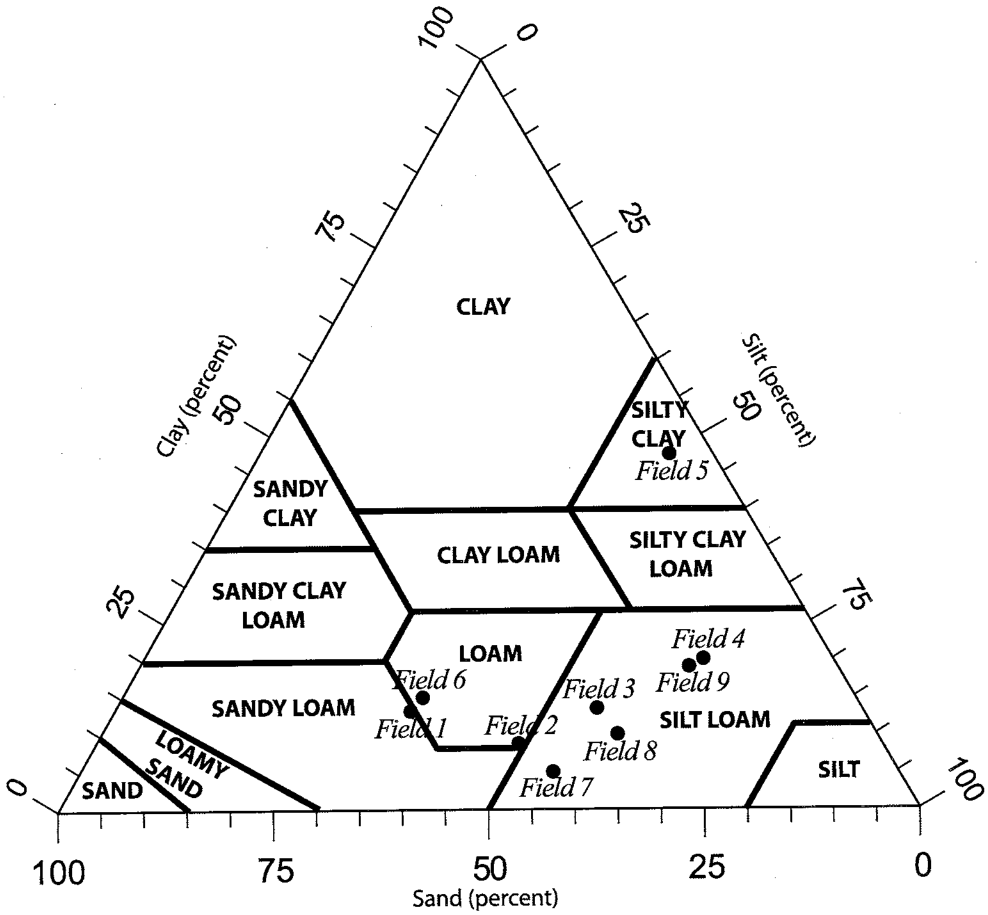

did not prove to be practical in field studies because of the complications in estimating the volumes of bound and free water in the soils. Furthermore, the authors pointed out that not all of the input quantities (fraction of bound and free water, dielectric constants for the bound water) used by the model are readily available for specific soils, and some of these parameters are not constant over time for a given soil. Therefore, for certain applications like field investigations, simple empirical models (Topp et al., 1980; Dobson et al., 1985; Peplinski et al., 1995 semiempirical models) are more convenient with input parameters that can be easily determined. The simplest approach is given by polynomial expressions that relate the dielectric constant to the volumetric soil water content and the percentage of sand and clay fractions at a specific frequency (Dobson et al., 1985).

Effects of Soil Texture on Radar Response

Water content is not the only factor affecting the attenuation of electromagnetic waves; it has also been shown that the texture of the soil and the bulk density are also key factors that can have an effect on electromagnetic waves (Hallikainen et al., 1985; Dobson et al., 1985; Peplinski et al., 1995). Peplinski et al. (1995) studied this phenomenon over the 0.3-1.3 GHz range of frequency. In their study they took dielectric measurements of various disturbed field soils. They used a dielectric probe inserted into 19 sets of distinctive soil conditions, distributed among four soil types and several moisture conditions. And for each soil condition, the real and imaginary parts of the relative complex dielectric constant (ε) were measured at 21 equally spaced frequency points, covering the range between 0.3 and 1.3 GHz. These measurements corresponded to 399 data points for the real part (ε') and the same number for the imaginary part (ε'') (Peplinski et al., 1995).

These dielectric measurements were performed on four soil types that were classified using the USDA soil classification scheme as the following: Silt Loam (15% sand, 65% silt, and 20% clay), Silt Loam (30% sand, 60% silt, and 10% clay), Silt Loam (40% sand, 55% silt, and 5% clay), and Loam (50% sand, 35% silt, and 15% clay) (See Figure 1.1). The dielectric measurements were also taken at 5, 10, 15, 20, and 25% volumetric water contents. Over the 0.3-1.3 GHz range, they found that both the relative dielectric constant and the effective conductivity of the soils were directly related to the soil texture and volumetric water content.

Landmine Detection Using GPR

Field experiments with ground penetrating radar have shown that soil conditions can have a very large effect on the performance of GPR systems for buried landmine detection. Under some soil conditions the landmine signature is of high quality while under others no signature can be detected at all. Fritzsche (1995) showed through modeling that GPR signals at 900 MHz would be strongly attenuated in moist soils and in clay soils especially. Trang (1996) found in both simulations and actual experiments with a GPR operating in the 600-800 MHz frequency range that it was easier to detect nonmetallic mines when the soil was moist. Johnson and Howard (1999) found that elevated soil moisture actually improves detection by improving the contrast between arid soils and plastic mines at the Energetic Materials Research and Testing Center (New Mexico Tech, Socorro, New Mexico). Scheers et al. (2000) modeled the performance of an ultra wide band GPR operating in the 1-5 GHz range for detection of metallic mines, and found that the maximum depth at which the mine could be detected decreased as the soil moisture increased.

Study Objective

Little work has been done in actually applying these semiempirical models to predict field soil conditions that would be beneficial for the use of ground penetrating radar in locating nonmetallic antitank landmines. To achieve this, field soils were chosen in various parts of the Socorro, New Mexico area and in Yuma, Arizona based on their soil texture classification. The aim of the study was to select soils that fall in the three sand, silt, and clay extremes of the USDA soil textural triangle. After the field sites were chosen, samples of the soils were analyzed by New Mexico Tech soil science students for bulk density and particle size distributions. Then a MATLAB code (Borchers et al., 2000) which uses field soil properties as inputs was employed to predict the amount of attenuation of the radar wave and the dielectric constant of the soils. From these model predictions the performance of the GPR system under various field water contents were analyzed. With these estimates, the GPR system was then taken to the field and tested. Furthermore, other soil conditions, outside the model's capabilities, were also analyzed in order to determine how ground penetrating radar systems function in saline soils and with metallic landmines.

2 - THEORY

2.1 Introduction to Ground Penetrating Radar

The basic theory behind the ground penetrating radar system has been in use since the early 1900s. The first known use of electromagnetic signals to locate remotely buried objects is attributed to Hulsmeyer with a German patent in 1904 (Reynolds, 1997). The system that Hulsmeyer used was a continuous wave transmission radar system. The pulse radar system, very much like present GPR systems, was not developed until the mid 1900s. In 1962, Husenbeck developed the first pulsed radar system to investigate buried features (Reynolds, 1997). Today, pulse GPR systems are manufactured commercially for use in many geophysical fields. Sensors & Software Ltd., Canada, manufactures the pulseEKKO line of radar systems, one of which was used for this research.

The pulse radar system is comprised of a signal generator, transmitting and receiving antennas, and a data storage device. The data storage device in most cases is a portable computer which allows for data processing and data display (See Figure 2.1). There are two basic antenna arrangements for GPR systems, monostatic and bistatic. Monostatic mode is when one antenna is used as both a transmitter and a receiver, whereas bistatic mode is when two separate antennae are used with one serving as a transmitter and the other as a receiver (Reynolds, 1997). The pulseEKKO 1000 system, used for this research, uses a bistatic antenna arrangement. In operation, the pulseEKKO radar system generates a pulse through the transmitter antenna. The pulse is determined

Figure 2.1 Basic theory of GPR operation in bistatic mode.

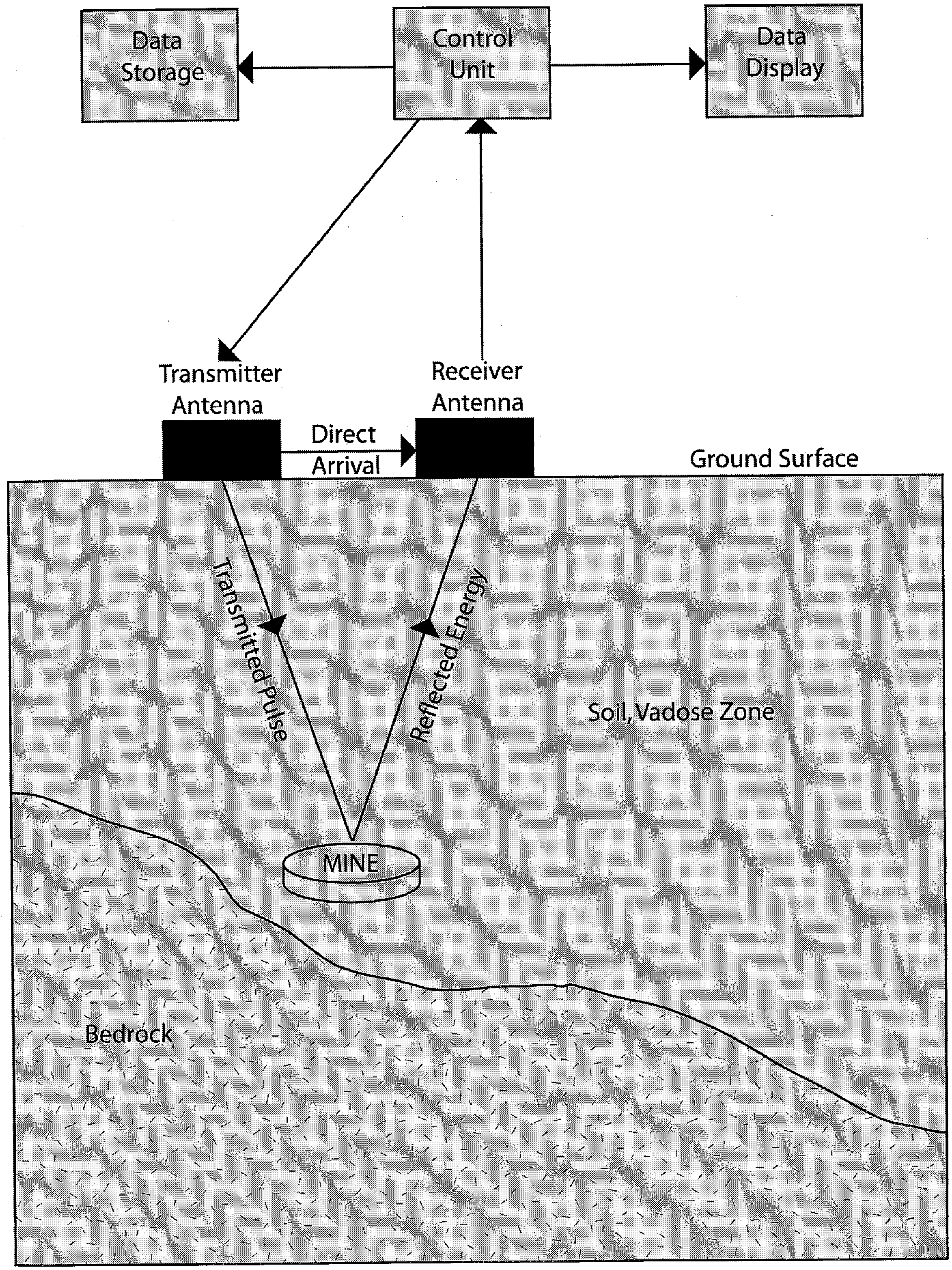

by the frequency of the antenna and is emitted about 50,000 times per second. At the same time the receiver scans at a fixed rate up to 32 scans per second (Reynolds, 1997).

Each scan is then displayed on a computer screen in the form of a two-way travel time versus horizontal position plot. In Figure 2.1, the line marked "Transmitted Pulse" is a ray that is perpendicular to the cone of radar waves that are radiating out from the antenna. This transmitted pulse represents one ray path that strikes the surface of the buried mine and is reflected off and back to the receiving antenna. In reality there are many other rays that follow very different paths than shown in Figure 2.1. Some are reflected by the landmine, others are scattered, and some are even absorbed by the landmine and the soil. One common form of scattering that occurs with radar waves in the subsurface is Mie scattering (Reynolds, 1997). The particles that cause Mie scattering have diameters that are roughly equivalent to the wavelength of the scattered radar waves (Campbell, 1996). Absorption of the rays occurs in the form of heat since electromagnetic energy is eventually turned into heat as it travels through the soil.

2.2 Wave Propagation Theory

The basics of ground penetrating radar technology are found in wave propagation theory. Materials transmit electromagnetic energy in different ways. In geologic applications, the main materials encountered are soil, water, and air, with the vadose zone being a unique combination of these three phases. The pulse radar system sends a short pulse of high frequency (10-1000 MHz) electromagnetic energy into the ground (Davis and Annan, 1989). The propagation of this electromagnetic energy depends on the electrical properties of the ground, which are directly controlled by the water content of the soil (Topp et al., 1980). Electromagnetic wave propagation in some cases can be affected by the magnetic permeability of the soil, however for nonmagnetic materials the magnetic permeability is equal to unity and the only factor that influences the speed and attenuation of the radar wave is the dielectric constant of the soil. For the range of frequencies used with GPR equipment, the electrical conductivity of the material plays little role in the transfer of electromagnetic energy. Instead the dielectric constant or relative permittivity is used to describe the high frequency electrical properties of materials, because at these frequencies the displacement (polarization) properties dominate the conductive properties for many geologic materials (Davis and Annan, 1989). Since the bulk soil electrical conductivity only plays a small part in the propagation of electromagnetic waves under typical GPR frequencies and minimal pore fluid salinity levels, the following discussion will focus more on the complex dielectric constant.

2.2.1 Dielectrics

A dielectric substance is nothing more than a non-conductor of electricity or an insulator. If a parallel plate capacitor is envisioned and an electromagnetic field is applied to the plates then the molecules in the material between the plates (the dielectric) will polarize. This polarization creates a layer of opposite charge on the surface of the dielectric, which in turn causes an increase in the capacitance of the plates. The ease with which a substance polarizes under an electrical field is what classifies substances as good or poor dielectrics. The easier materials polarize the greater their dielectric constant. For example, pure water has a dielectric constant of 80 and air has a dielectric constant of 1 (See Table 2.1). Water will increase the capacitance of a parallel plate capacitor by a factor of 80 over that of air. Dielectrics can be further explained in terms of the creation of dipole moments under the application of an electric field. Mathematically it is expressed by the following equation:

$$D = \varepsilon * E \tag{4}$$

where D is the dipole moment density (F*V/m^2), ε is the permittivity of the material in units of Faradas per meter (F/m), and E is the applied electric field in volts per meter (V/m). The dielectric constant (ε_r) is given by the ratio of the material permittivity to the permittivity of free space, $\varepsilon_o = 8.854 \times 10^{-12}$ (F/m).

$$\varepsilon_r = \frac{\varepsilon}{\varepsilon_o} \tag{5}$$

The complex dielectric constant (ε^*) for non-conductive materials is given by:

$$\varepsilon^* = \varepsilon' - \varepsilon'' i \tag{6}$$

where the ε' is the real part of the dielectric constant and ε" is the imaginary or loss part of the dielectric constant. The imaginary part of the complex dielectric constant accounts for the absorption of energy within the dielectric material, which is used to quantify the absorption of radar waves within the soil. When the material is conductive the $\frac{\sigma_{dc}}{\omega\varepsilon_o}$ term, included within the loss part of the dielectric constant (ε"), can become significant. In this term, σ_{dc} is the direct current (d.c.) conductivity (S/m) and ω is the angular frequency ($2\pi f$). At low frequencies this term dominates since conduction currents predominate over displacement currents (Nabighian, 1987). For example, consider a sand soil with an electrical conductivity of 0.01 S/m, at a frequency of 100 KHz, this term contributes

Table 2.1 **Dielectric constant (ε), conductivity (σ), velocity (ν), and attenuation (α) of different materials from Annan (2001).**

MATERIAL	ε	σ (mS/M)	ν (m/ns)	α (dB/m)
Air	1	0	0.3	0
Distilled Water	80	0.01	0.033	2e-3
Fresh Water	80	0.5	0.033	0.1
Sea Water	80	3e3	0.01	103
Dry Sand	3-5	0.01	0.15	0.01
Saturated Sand	20-30	0.1-1	0.06	0.03-0.3
Limestone	4-8	0.5-2	0.12	0.4-1
Shales	5-15	1-100	0.09	1-100
Silts	5-30	1-100	0.07	1-100
Clays	5-40	2-1000	0.06	1-300
Granite	4-6	0.01-1	0.13	0.01-1
Dry Salt	5-6	0.01-1	0.13	0.01-1
Ice	3-4	0.01	0.16	0.01

about 2e3 to the imaginary part of the complex dielectric constant. If a frequency of 900 MHz, which is a practical GPR frequency, is considered for the same sandy soil this term contributes about 0.2 to the imaginary part of the complex dielectric constant. The first example at 100 KHz contributes more than 90% and the second at 900 MHz contributes less than 5% to the complex dielectric constant of the soil.

Over the high frequency range, it has been shown that the complex dielectric constant of water and soils is not constant but varies with frequency and temperature (Hipp, 1974). Figure 2.2 shows this relationship between frequency and the complex dielectric constant of water at two different temperatures, 0°C and 25°C. However, for most geologic investigations with soil electrical conductivities less than 100 mS/m and GPR frequencies between 10 and 1000 MHz, Davis and Annan (1989) suggest that the amount of electrical loss is insignificant. Thus, over this range of frequencies it is safe to assume that the complex dielectric constant is invariant with respect to frequency. The bulk dielectric constant of soil water systems may be assumed constant over normal GPR frequencies, however it cannot be assumed constant over a range of soil water contents.

2.2.2 Effects of Water Content on Bulk Soil Dielectric Constant and Landmine Detection

Recall from Table 2.1 that fresh water has a dielectric constant of 80 and dry sandy soils have a dielectric constant of 3 to 5. When these two substances are combined together the effective dielectric constant of the soil will increase significantly. This new effective dielectric constant of the soil water mixture can be as high as 20 to 30 in wet

Figure 2.2 **The relationship between dielectric constant and frequency for water, where ε' is the real part and ε'' is the imaginary part of the dielectric constant from Hoesktra and Delaney (1974).**

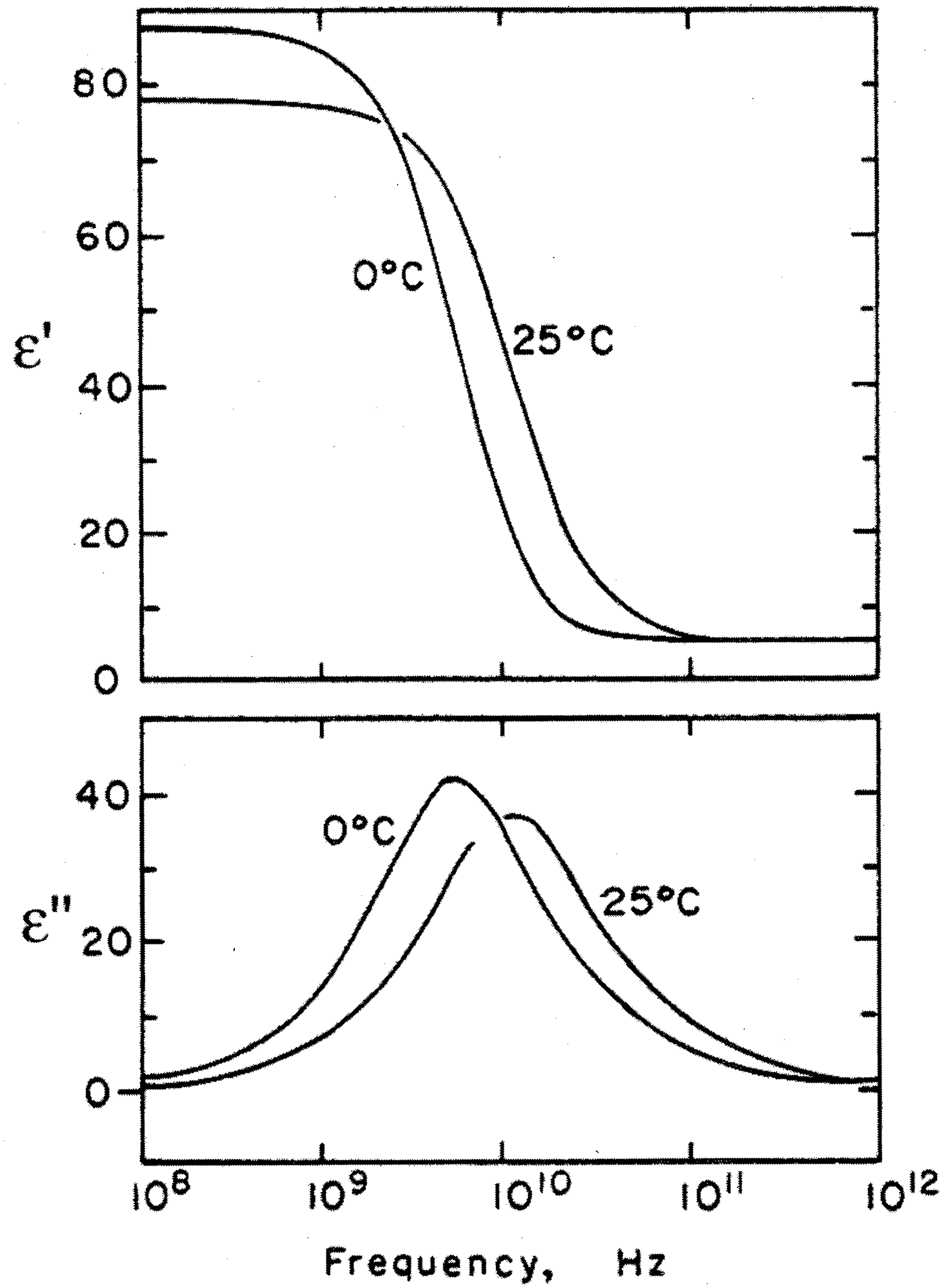

sandy soils (Davis and Annan, 1989). Because of the magnitude of the dielectric constant of fresh water, when a small amount of fresh water is applied to a dry soil, an increase in the bulk dielectric constant will be observed. When the soil is fully saturated, the bulk dielectric constant of the soil mixture can be very large. Topp et al. (1980) proposed an empirical relationship for calculating the bulk dielectric constant of soil based on the volumetric soil water content (See Equation (2)). Equation (2) was the result of a best-fit curve for soils measured in their experiments (See Topp et al., 1980 for details). A plot of this equation for various water contents can be seen in Figure 2.3. Because the bulk dielectric constant of soil can become very large, approaching 45 at 60 % water content, this phenomenon can be used to enhance landmine detection when using ground penetrating radar.

For this research project, plastic antitank landmines with a dielectric constant of about 3 were used. From Table 2.1, the dielectric constant for dry soils with high sand and silt contents tends to be low (around 3-5). This range overlaps with the dielectric constant of the plastic antitank landmine, so during dry field conditions detection will be difficult, in theory, using ground penetrating radar sensors. However, if water is added to the soil, the dielectric constant of the plastic landmine will remain the same because of its non-porous texture, yet the dielectric constant of the soil will rise, which should enhance detection.

2.2.3 Velocity, Attenuation and Reflection of Radar Waves

The ability of the ground penetrating radar system to locate buried objects depends on the properties of the soil to allow transmission of electromagnetic energy. As

Figure 2.3 Volumetric water content versus dielectric constant using Topp's empirical equation (See Equation (2)).

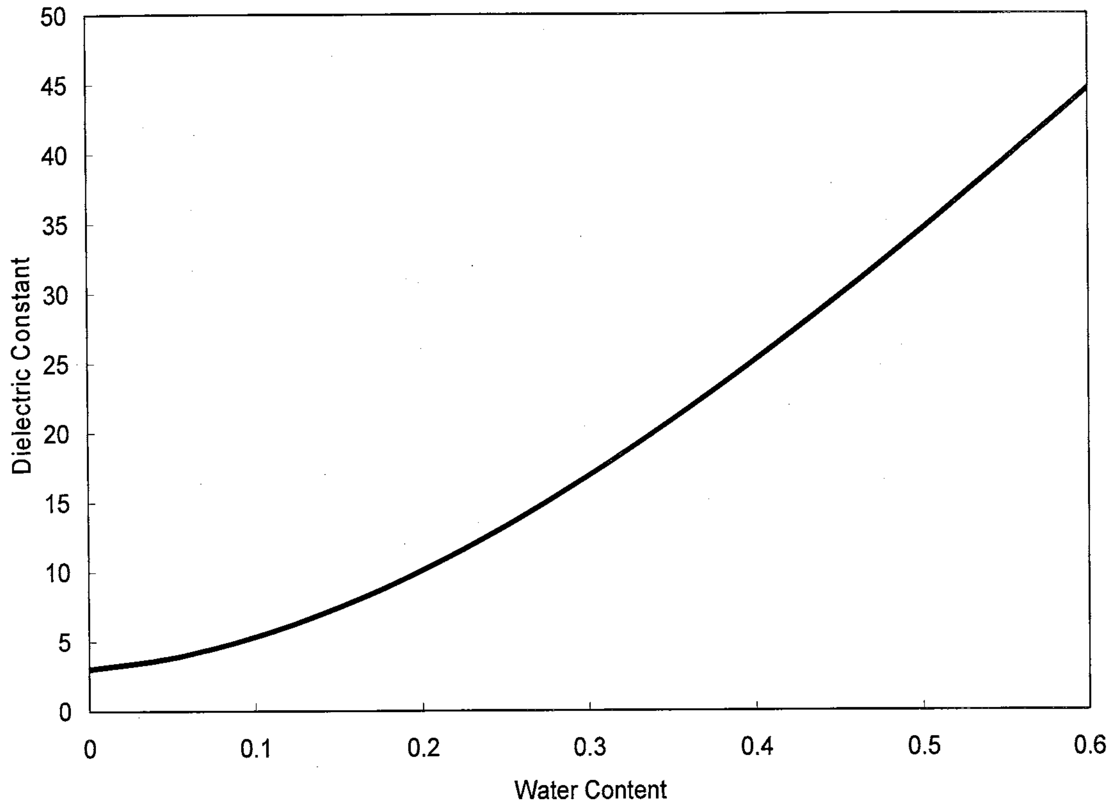

stated before, the main electrical property that controls how radar waves propagate through the subsurface is the complex dielectric constant. Consequently, the velocity of the radar wave is dependent upon this too. The velocity of an electromagnetic wave traveling through soil is given by:

$$V = \frac{c}{\left\{\left(\frac{\varepsilon'}{2}\right)\left[\left(1+\tan^2\delta\right)+1\right]\right\}^{0.5}} \tag{7}$$

where c is the speed of light in free space, c = 2.997x10^8 m/s, and

$$\tan\delta = \frac{\sigma' + \omega\varepsilon''}{\sigma'' + \omega\varepsilon'}. \tag{8}$$

In Equation (8) σ' is the real part and σ'' is the imaginary part of the complex conductivity. For dielectric media at high frequencies where $\omega\varepsilon'' >> \sigma'$ and $\omega\varepsilon' >> \sigma''$, (which was the condition for our 900 MHz GPR system and the soils used in this research) Equation (8) can be approximated by,

$$\tan\delta \approx \frac{\varepsilon''}{\varepsilon'} \text{ (Nabighian, 1987).} \tag{9}$$

In low-loss materials, where $\tan\delta \approx 0$, Equation (7) reduces to the following expression,

$$V \approx \frac{c}{\left(\varepsilon'\right)^{0.5}}. \tag{10}$$

Equation (10) is an approximation, which assumes that the imaginary part of the complex dielectric constant can be ignored; however, electrical loss will affect the velocity of the signal in soils to some extent. Topp et al. (1980) stated that the electrical loss has been small and has not significantly altered the measured propagation velocity in his experiments. From our own calculations we found that the error in Equation (10) was typically less than 5% for real soils. Thus for most studies, the velocity of the radar wave can be approximated with Equation (10).

As GPR signals travel through the soil, they are attenuated at a rate determined by the complex dielectric constant of the soil. The one way attenuation loss in units of decibels per meter (db/m) is given by

$$\text{Attenuation Loss} = 8.6855 d\alpha \tag{11}$$

where d is the depth to the object from which the GPR signal is reflecting, and α is given by

$$\alpha = \frac{2\pi f}{c}\sqrt{\left(\frac{\varepsilon^{'}}{2}\left(\sqrt{1+\left(\frac{\varepsilon^{''}}{\varepsilon^{'}}\right)^{2}}-1\right)\right)} \tag{12}$$

where c is the speed of light in free space (2.997×10^{8} m/s), $\frac{\varepsilon^{''}}{\varepsilon^{'}}$ is the ratio of the real part to the imaginary part of the complex dielectric constant, and f is the frequency of the radar wave. The attenuation factor (α) is a fundamental cause of loss of energy and is a function of the dielectric constant, magnetic, and electric properties of the media and the frequency of the signal (Reynolds, 1997). From Equation (12) it is evident that attenuation is directly proportional to frequency, the square root of the real part of the complex dielectric constant, and bulk conductivity (σ), since $\tan\delta \approx \frac{\varepsilon''}{\varepsilon'}$. At high frequencies, the total attenuation of the electromagnetic waves will increase. Since the soil conductivity and the square root of the dielectric constant are also directly proportional to the attenuation factor, the overall soil composition will greatly alter the amount of attenuation. For water-saturated soils, the electrical conductivity of the pore water can cause increased amounts of attenuation in direct relation to the porosity of the soil. For soils containing large amounts of clay, the attenuation will be greater due to the large amount of bound water within the clay lattice structure. For low loss media, the attenuation can be simplified by the following equation:

$$\alpha = \frac{1.69x10^3 \sigma}{(\varepsilon')^{0.5}} \tag{13}$$

where $\sigma = \sigma_{DC} + \omega\varepsilon''\varepsilon_o$ combines both the d.c. conductivity and dielectric losses. For this equation to be correct, $\frac{\sigma}{\omega\varepsilon'\varepsilon_0}$ must be much less than unity (Davis and Annan, 1998).

As the GPR is moved along the surface of the soil, the antenna emits and receives electromagnetic energy. In order for detection of a buried object to occur, the object must reflect some of the incident electromagnetic energy. When this happens a reflection is produced. In order for the buried object to reflect the incident radio waves, it must have a different dielectric constant than the surrounding material. It is the contrast in relative dielectric constants between adjacent layers that gives rise to reflection of incident electromagnetic radiation (Reynolds, 1997). The amount of reflected energy (R) is given by the contrast in relative dielectric constants,

$$R = \frac{\sqrt{\varepsilon_1} - \sqrt{\varepsilon_2}}{\sqrt{\varepsilon_1} + \sqrt{\varepsilon_2}} \tag{14}$$

where ε_1 and ε_2 are the unit less relative dielectric constants of two different layers which for landmine detection is the landmine and the soil. If the two layers have vastly different dielectric constants then there will be a large amount of reflection, but if the layers have similar dielectric constants then the distinction between the two layers will disappear and detection is impossible. Table 2.2 shows the reflection coefficients for various boundaries. The reflection coefficient going from saturated soil to a plastic landmine will be very similar to the wet soil to rock example given in this table, which is 0.28.

For Equation (14) to be accurate, the reflecting subsurface layer must be very large in comparison to the wavelength of the electromagnetic wave. However, when the reflecting layer is a landmine, the wavelength of the electromagnetic wave may be very close to the diameter of the landmine, thus plane wave reflection theory should not be used since it may under-predict reflections.

Although this is the case for the landmines used in this project, a qualitative discussion of the reflection coefficient from metallic and nonmetallic landmines is in order. Plastic landmines usually have dielectric constants that are low, very close to the dielectric constant of dry soil, where metallic landmines have dielectric constants that approach infinity since they are conductors. So metallic landmines will produce perfect reflections under all soil conditions where nonmetallic landmines will produce reflections governed by the contrast in the dielectric constant of the soil and the landmine.

The depth to which the electromagnetic signal has decreased in amplitude to 1/e percent of its original value is called the skin depth and is defined as one over the attenuation. The skin depth varies over a wide range of geologic materials. The skin depth should only be used as a rough estimate of the depth of electromagnetic wave penetration. To find the true radar range, the properties of the GPR instrument have to be factored in along with the properties of the subsurface media. The total path loss for a given distance is made up of five terms: antenna losses, transmission losses between the

Table 2.2 Reflection coefficients (R) for various boundaries from Annan (2001).

FROM		TO		REFLECTION COEFFICIENT
Air	K = 1	Dry Soil	K = 5	-0.38
Dry Soil	K = 5	Wet Soil	K = 25	-0.38
Dry Soil	K = 5	Rock	K = 8	-0.12
Wet Soil	K = 25	Rock	K = 8	0.28
Water	K = 81	Gyttja	K = 50	0.12
Water	K = 81	Rock	K = 8	0.52
Ice	K = 3.2	Water	K = 81	0.67
Frozen Soil	K = 6	Wet Soil	K = 25	0.34
Soil	K = 3-50	Metal	K = ∞	-1

air and the ground, losses caused by the geometrical spreading of the radar beam, attenuation within the ground as a function of the material properties, and losses due to scattering of the radar signal from the target itself (Reynolds, 1997). To read a full description of the radar system characterizations see Davis and Annan (1989).

2.2.4 Models of Soil Electrical Properties and Radar Response

The dielectric properties of a soil depend on a number of factors, including its bulk density, the texture of the soil particles (sand, silt, or clay), the density of the soil particles, typically about 2.66 g/cm^3 (Jury et al., 1991), the volumetric water content of the soil, the temperature, and the frequencies of interest (Hoekstra and Delaney, 1974; Topp et al., 1980; and Ulaby et al., 1986). Recent research has also shown that the dielectric properties of soil depend on the amount of "bound water" which is in close contact with minerals in the soil (Wang and Schmugge, 1980; Dobson et al., 1985). Theoretical and empirical models of the dielectric properties of the different components of the soil have been combined into semi-empirical mixing models which can be used to predict the dielectric properties of field soils (Hoekstra and Delaney, 1974; Wang and Schmugge, 1980; Dobson et al., 1985; Wobschall, 1977; Peplinski et al., 1995).

This section summarizes the earlier model of Dobson, Ulaby, Hallikainen, and El-Rayes (1985), and the later model of Peplinski, Ulaby, and Dobson (1995). The earlier model was calibrated for frequencies ranging from 1.4 to 18 GHz (Hallikainen et al., 1985) and the latter was calibrated by fitting the model to a set of experimental observations with a variety of soil textures, soil water contents, and frequencies from 0.3 to 1.3 GHz (Peplinski et al., 1995).

The inputs to the 1985 model of Dobson, Ulaby, Hallikainen, and El-Rayes consist of the volumetric soil water content θ, the frequency *f*, the fraction of sand particles *S*, the fraction of clay particles *C*, the density of the soil particles ρ_S (a typical value is 2.66 g/cm^3), and the bulk density of the soil ρ_B. An empirically derived formula for effective soil conductivity is the following

$$\sigma_{eff} = -1.645 + 1.939\rho_B - 2.013S + 1.594C. \tag{15}$$

The sand and clay fractions also enter the model through two constants which depend on the soil type but are independent of the frequency and soil water content.

$$\beta^{'} = 1.2748 - 0.519S - 0.152C \tag{16}$$

$$\beta^{''} = 1.33797 - 0.603S - 0.166C \tag{17}$$

The real ($\varepsilon^{'}_{fw}$) and imaginary ($\varepsilon^{''}_{fw}$) parts of the dielectric constant (ε_{fw}) for the free water are given by

$$\varepsilon_{fw} = \varepsilon^{'}_{fw} - \varepsilon^{''}_{fw} i \tag{18}$$

$$\varepsilon^{'}_{fw} = \varepsilon_{w\infty} + \frac{\varepsilon_{w0} - \varepsilon_{w\infty}}{1 + (2\pi f \tau_w)^2} \tag{19}$$

and

$$\varepsilon^{''}_{fw} = \frac{2\pi f \tau_w(\varepsilon_{w0} - \varepsilon_{w\infty})}{1 + (2\pi f \tau_w)^2} + \frac{\sigma_{eff}}{2\pi\varepsilon_0 f}\frac{(\rho_S - \rho_B)}{\rho_S \theta}. \tag{20}$$

In these formulas, ε_0 is the dielectric permittivity of free space, ε_{w0} is the static dielectric constant of water (80.1 at 20° C), $\varepsilon_{w\infty}$ is the high frequency limit of $\varepsilon^{'}_{fw}$ (4.9), and τ_w is the relaxation time of water (9.23x10^{-12} s at 20° C). The dielectric constant of the soil particles (ε_S) is given by the empirical model

$$\varepsilon_S = (1.01 + 0.44\rho_S)^2 - 0.062. \tag{21}$$

Finally, the real (ε') and imaginary (ε'') parts of the dielectric constant for the bulk soil are estimated by

$$\varepsilon = \varepsilon' - \varepsilon'' i \tag{22}$$

where

$$\varepsilon' = \left[1 + \frac{\rho_B}{\rho_S}\left(\varepsilon_S^{\alpha} - 1\right) + \theta^{\beta'} \varepsilon_{fw}^{'\alpha} - \theta\right]^{\frac{1}{\alpha}} \tag{23}$$

and

$$\varepsilon'' = \left[\theta^{\beta''} \varepsilon_{fw}^{''\alpha}\right]^{\frac{1}{\alpha}}. \tag{24}$$

In these formulas, $\alpha = 0.65$ is a constant that has been empirically fitted to experimental data.

The 1995 model of Peplinski, Ulaby, and Dobson which covers a lower frequency range (0.3-1.3 GHz) is identical except the conductivity is given by

$$\sigma_{eff} = 0.0467 + 0.2204\rho_B - 0.4111S - 0.6614C \tag{25}$$

and the real part of the complex dielectric constant is given by

$$\varepsilon' = 1.15\left[1 + \frac{\rho_B}{\rho_S}\left(\varepsilon_S^{\alpha} - 1\right) + \theta^{\beta'} \varepsilon_{fw}^{'\alpha} - \theta\right]^{\frac{1}{\alpha}} - 0.68. \tag{26}$$

The high frequency model was compared to 809 measurements of the real and imaginary parts of the dielectric constant. The r-squared value for the real part (ε') was

0.982 where the r-squared value for the imaginary part (ε'') was 0.988 (Dobson et al., 1985). The low frequency model was compared to 399 measurements of the real and imaginary part of the dielectric constant and the r-squared values were 0.985 for the real part (ε') and 0.940 for the imaginary part (ε'') (Peplinski et al., 1995).

2.3 Time Domain Reflectometry

Time Domain Reflectometry (TDR) probes were used at each site to determine the dielectric constant and soil water content. The theory behind TDR probes is very similar to that of ground penetrating radar. TDR probes measure the dielectric constant of the soil and use this measurement to calculate the soil water content. For details on dielectric theory see Section 2.2.1. The measurement of the dielectric constant of the soil is obtained by placing a pair of stainless steel rods connected to a Tektronix 1502b metallic cable tester into the ground (three rods are sometimes used instead of two). The rods work as conductors and the soil between the rods acts like the dielectric medium, which is the same in theory as the parallel plate capacitor described in Section 2.2.1. A step voltage pulse with a rise time of 200 ps and frequency range of 16.6 kHz to 1.75 GHz (Tektronix, 1987) is sent down a coaxial cable connected to the stainless steel rods. The electromagnetic pulse is then reflected at the tips of the stainless steel rods and returns to the cable tester. The two-way travel time is recorded, and using the fixed length of the coaxial transmission line, the dielectric constant of the soil can be calculated using the following equation:

$$\varepsilon_r = \left(\frac{ct}{2L}\right)^2 \qquad (27)$$

where c is the velocity of electromagnetic waves in a vacuum ($3x10^8$ m/s), t is the travel time from the cable tester to the probe and back to the cable tester again, and L is the length of the coaxial transmission cable. To calculate the water content, Topps equation is often used (See Equation (2)). It is claimed that the volumetric water content of soils can be determined with this method and Topps equation to an accuracy of ±2% and a precision of ±1% (Hillel, 1998).

3 - MATERIALS AND METHODS

3.1 Sprinkler System

To test the mathematical model described in the previous section, three sites were chosen based on their particle size distributions. The sites required uniformly high volumetric soil water contents (30 to 40%); so to achieve these values, a sprinkler system was constructed. The three sites were located about 20 miles from Socorro, and because of this the sprinkler system needed to be mobile. PVC plastic tubing was used because it is inexpensive and lightweight. The frame for the sprinkler system was built out of ½ inch PVC tubing in the shape of a square measuring 3 by 3 meters. The top and bottom sections of the frame were constructed of eight 1.5 meter segments that screwed into elbow joints on both ends and into tee joints in the center (See Figure 3.1 for details). This was done so that when the system was taken apart it would not measure any longer than 1.5 meters, which made it convenient for travel. When assembled, the sprinkler frame measured 1 meter tall. This height was chosen based on the angle of spray and the radius of throw from the sprinkler nozzles. The center of the sprinkler system had a cross-shaped joint which had steel pipe extending to all four sides. Steel conduit piping was chosen for the upper section of the sprinkler frame because of its strength, since the center pipe extended the full length of the sprinkler system. The center pipe had the spray nozzles attached to it, and was fully removable from the system so that the nozzle tips could be easily adjusted (See Figure 3.1). Due to the severe wind patterns in the

Figure 3.1 Diagram showing the geometry of the sprinkler system.

TOP VIEW

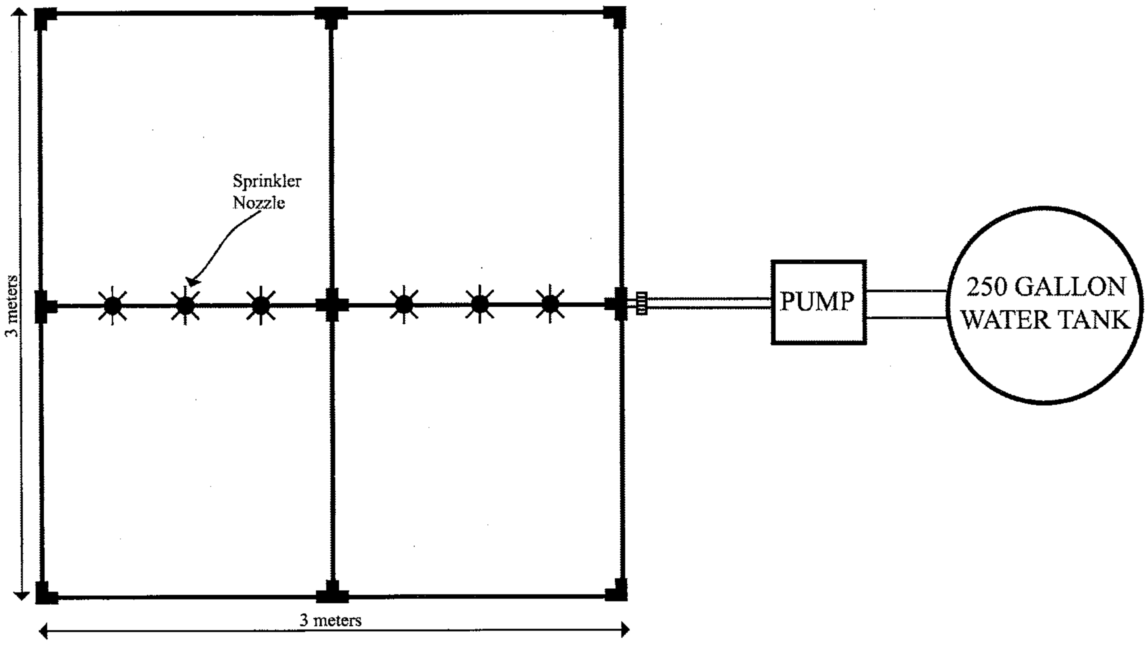

SIDE VIEW

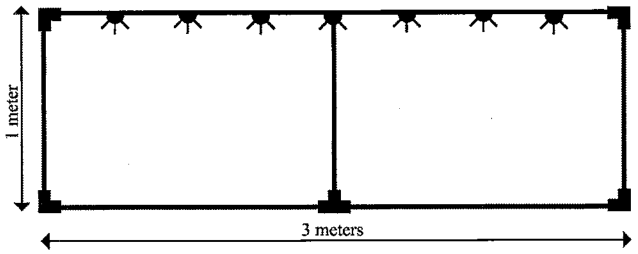

Sevilleta National Wildlife Refuge, the entire sprinkler system was enclosed by a plastic tarp. The tarp was fastened to the system with metal snaps, allowing for easy removal when the system needed to be taken apart and moved.

Rain Bird XS-360TS-1032 sprinkler nozzles were chosen because they gave the best spray coverage, and they have adjustable ball valve heads which allowed for adjustment of spray radius during operation. The hose pressure chosen for the system was 40 psi.

Table 3.1 A tabulated description of the XS-360TS-1032 spray nozzle in upward position.

Pressure (psi)	GPH	Radius of Throw (m)
15	0-17.3	1.4
20	0-19.8	1.7
30	0-24.5	2.0

The data in Table 3.1 refers to the nozzle spraying in an upright position and fully opened, 22 clicks. The ball valve heads on the Rain Bird XS-360TS-1032 sprinkler nozzle opened by clicks, zero clicks was the closed position and 22 clicks were fully open. For the sprinkler system, the nozzles were positioned in an upside down orientation; which changed some of the information seen in Table 3.1, since gravity pulling down on the spray will tend to shrink the radius of throw. From experimentation it was determined that at one meter above the horizontal plane, 40 psi hose pressure, the XS-360TS-1032 nozzle omitted a throw radius of 1.5 meters. Seven XS-360TS-1032 spray nozzles were spaced 30 cm apart along the central steel tube (See Figure 3.1). At the end of the tubing a ½ inch adapter was installed, which could be connected to an ordinary garden hose. To supply water to the sprinkler system, a 3.5 horsepower gasoline water pump was used. The pump had a 2 inch intake and a ½ inch outlet. The intake was connected to a 250 gallon water tank and the outlet was connected to a 12 foot garden hose that fed the sprinkler system.

To test the effectiveness of the sprinkler system, the JE Christiansen's Uniformity Coefficient (CU) was calculated. This is the most widely accepted measure of irrigation uniformity in the turf industry (Zoldoske et al., 1994).

$$CU = 100(1-D/M) \tag{28}$$

$$D = (1/n)\Sigma|X_i - M| \tag{29}$$

$$M = (1/n)\Sigma X_i \tag{30}$$

In Equations (28) through (30), D is the average absolute deviation from the mean, M is the mean application, X_i is the individual application amount, and n is the total number of individual application amounts. To measure the uniformity coefficient (CU), a grid of 2 by 1 meters was drawn on a piece of plastic tarp. The grid squares were spaced 10 cm apart. Fifty 8 ounce cups, spaced 20 cm apart, were placed on the grid at the intersection of the squares. Then the sprinkler was positioned over the tarp with the cups and left running for 20 minutes. After this, each cup was weighed and recorded in matrix form matching the grid layout. Each matrix was then inputted into a MATLAB program utilizing Equations (28) through (30). A contour plot of the results can be seen in Figure 3.2. The highest coefficient of uniformity calculated was 82% (Figure 3.2 (A)) and the worst was 78% (Figure 3.2 (B)).

Figure 3.2 **Two contour plots showing the distribution of the mass (mg) of water produced by the sprinkler system over a 20 minute period. Plot (A) shows a uniformity coefficient of 82% and (B) shows a uniformity coefficient of 78%.**

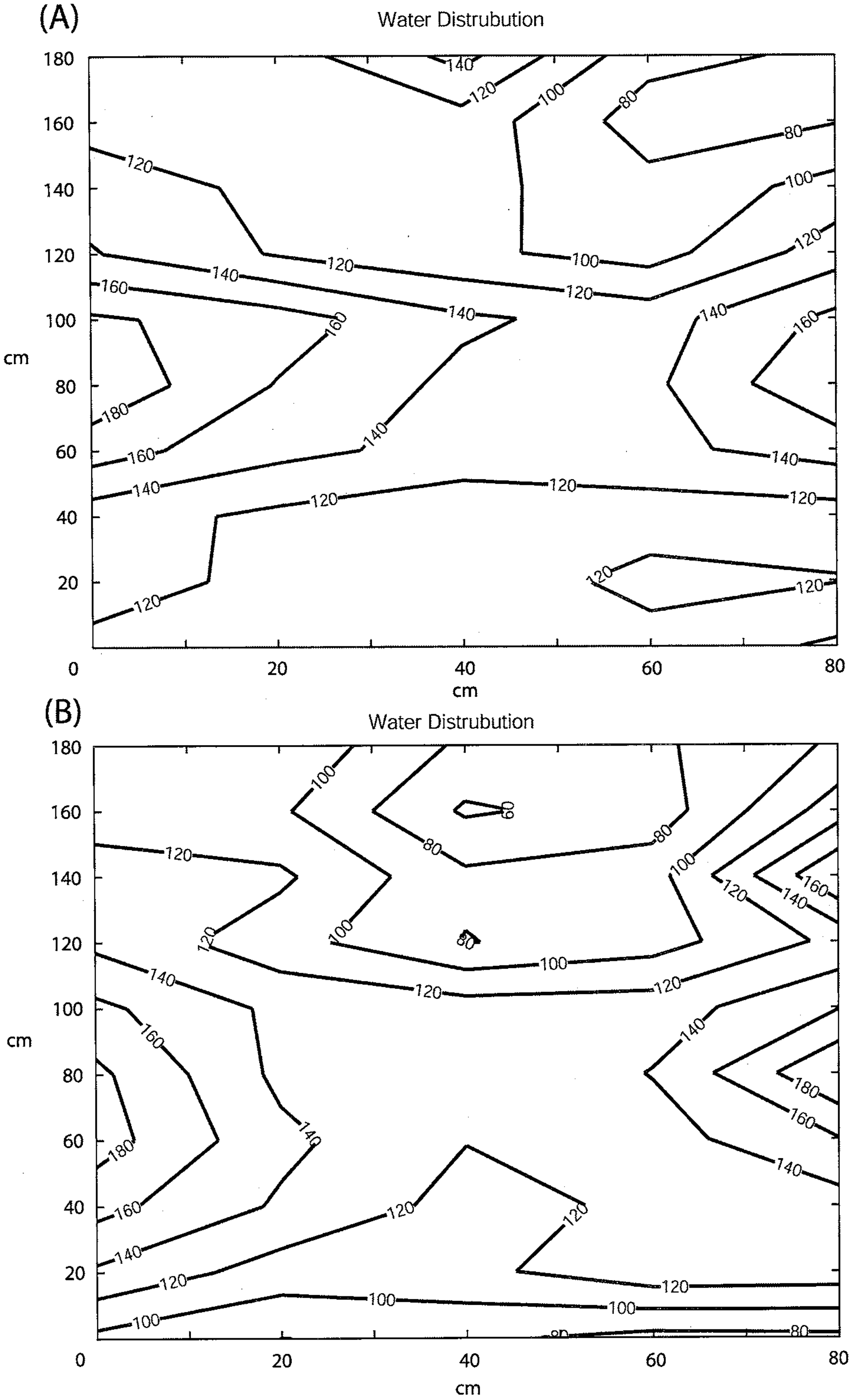

3.2 Ground Penetrating Radar Frame

To guide the ground penetrating radar system over each landmine site with accuracy, a positioning frame was constructed. The frame was constructed entirely out of wood to minimize the interference between it and the electromagnetic instruments. The dimensions of the frame were 2 meters long by 1 meter wide by 12 cm tall (See Figure 3.3 (A)). The frame had removable inner guides that elevated the transmitting and receiving antennas of the radar system 4 cm above the ground. These inner guides had one hundred, ½ cm deep dados spaced 2 cm apart along the entire length of the guides. A small block of wood fit into the dados on each guide and was used as a back stop for the radar antenna. When used in the field, the radar system was placed inside the guides (See Figure 3.3 (B)), with the block of wood placed into the dado directly in front of the antenna. After the trace was collected, the block was removed and the antennas were moved forward one dado spacing (2 cm). This process was repeated over the entire length of the GPR frame.

3.3 Simulant Antitank Landmines

The simulant landmines used in this experiment were completely inert and composed of Dow Corning 3110 RTV Silicon Rubber. They are designed to simulate a Netherlands landmine of type NR26, which is a nonmetallic landmine and has dimensions of 30.0 cm in diameter and 11.5 cm in height. The TNO Physics and Electronics Laboratory in the Netherlands, which specializes in producing inert landmines for detection purposes, manufactured these landmines (See Figure 3.4).

Figure 3.3 GPR frame used to guide movement of radar system over landmine plots (A) shows dimensions and (B) shows field setup.

(A)

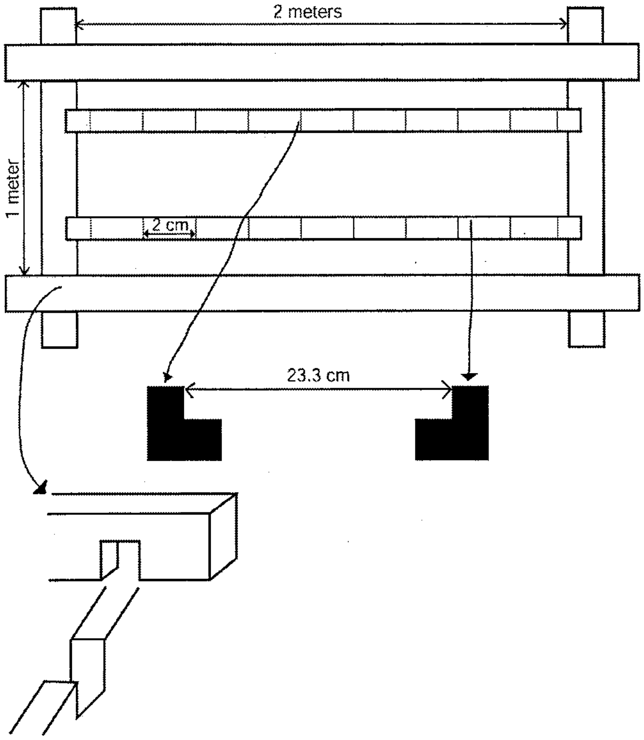

(B)

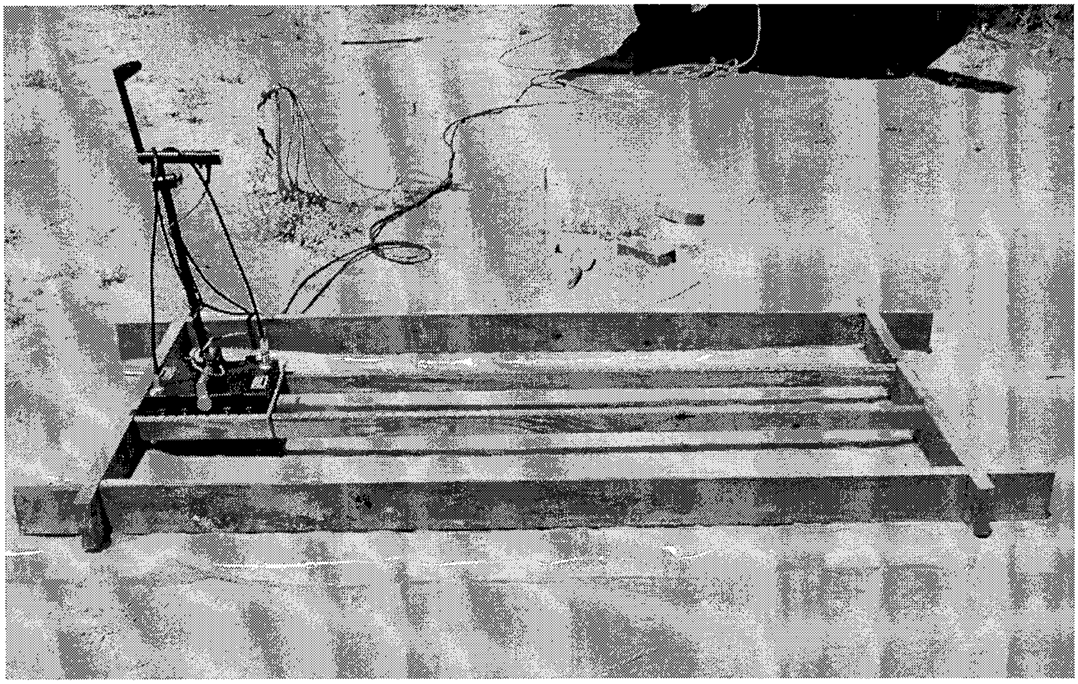

Figure 3.4 Netherland type NR26 simulant landmine (left) and U.S. Army edition inert target landmine (right).

3.4 Field Sites in Socorro, NM

Three field sites were chosen based on their particle size and soil mineralogy. The three types of soils chosen were sand, silt, and clay. The sand and silt sites were located in the Sevilleta National Wildlife Refuge, and the clay site was located in the Bosque Del Apache National Wildlife Refuge. The Sevilleta National Wildlife Refuge is a long-term study area funded by the National Science Foundation. It is located in central New Mexico and originated as a Spanish land grant. Today it is managed by the U.S. Fish and Wildlife Service and is used by scientists to conduct environmental research studies. The entire area of the Sevilleta is about 3,600 square kilometers. The Bosque Del Apache National Wildlife Refuge is located at the northern edge of the Chihuahuan Desert and straddles the Rio Grande approximately 20 miles south of Socorro, New Mexico. The refuge contains about 12,900 acres total; 3,800 acres are active floodplain of the Rio Grande and 9,100 acres are areas where water is diverted to create extensive wetlands, farmlands, and riparian forests. The remainder of Bosque Del Apache consists of arid foothills and mesas, bounded by the Chupadera Mountains on the west and the San Pascual Mountains on the east.

The sand and silt sites were located in the Rio Salado area of the Sevilleta (See Figure 3.5). The sand site was located near the Rio Salado sand dunes and the soil had a composition of 95% sand, 2% silt, and 3% clay, and a bulk density of 1.6 g/cm^3. The silt site was located closer to the Rio Salado floodplain and the soil had a composition of 2.4% sand, 65.7% silt, and 31.9% clay, and a bulk density of 1.3 g/cm^3. Using the USDA classification scheme (Klute, 1986), the sand site soil was classified as sand and the silt site soil was classified as a silty clay loam (See Figure 3.6).

Figure 3.5 Map of Socorro County with arrows indicating research sites.

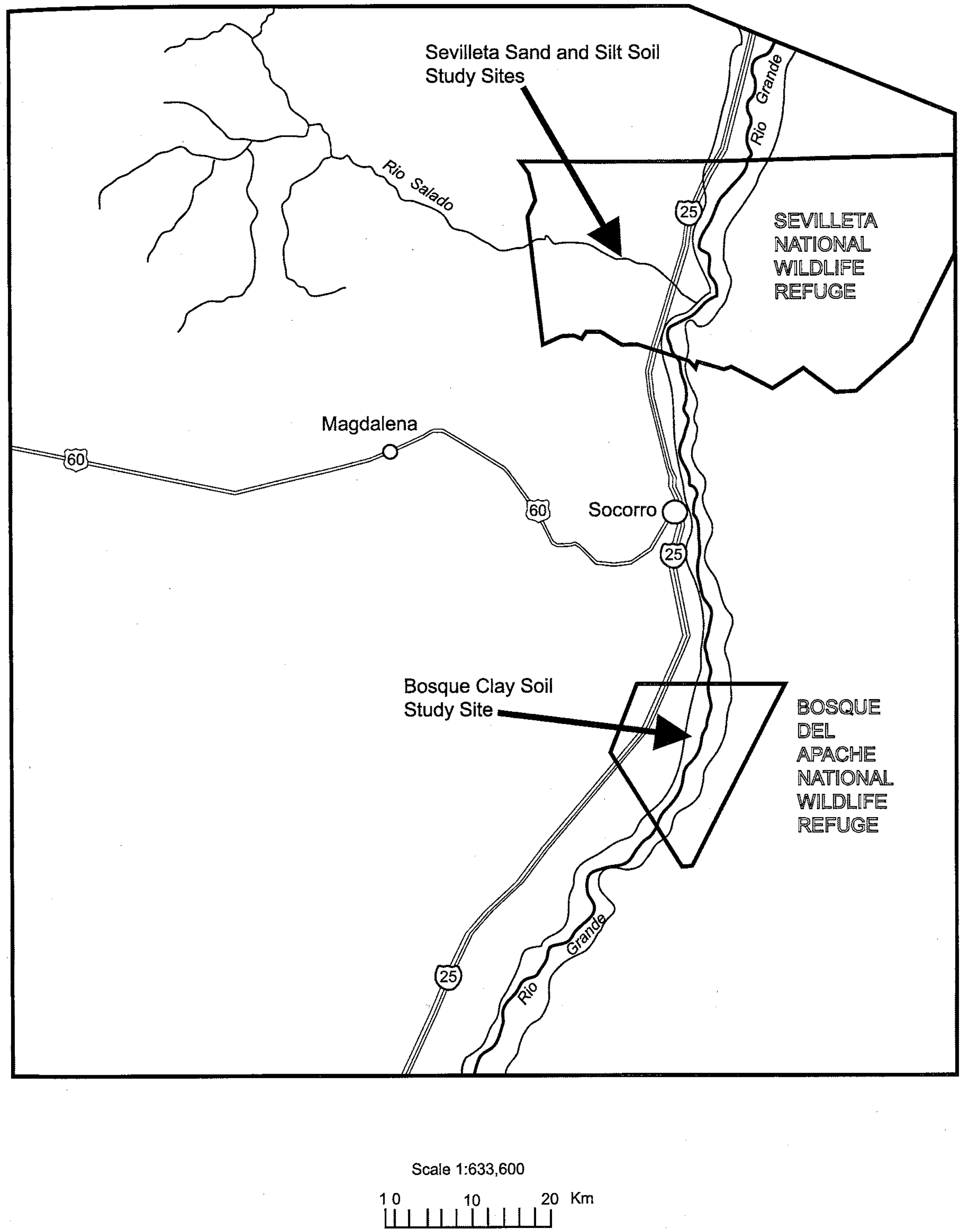

Figure 3.6 USDA classification of the soil types found at each study site.

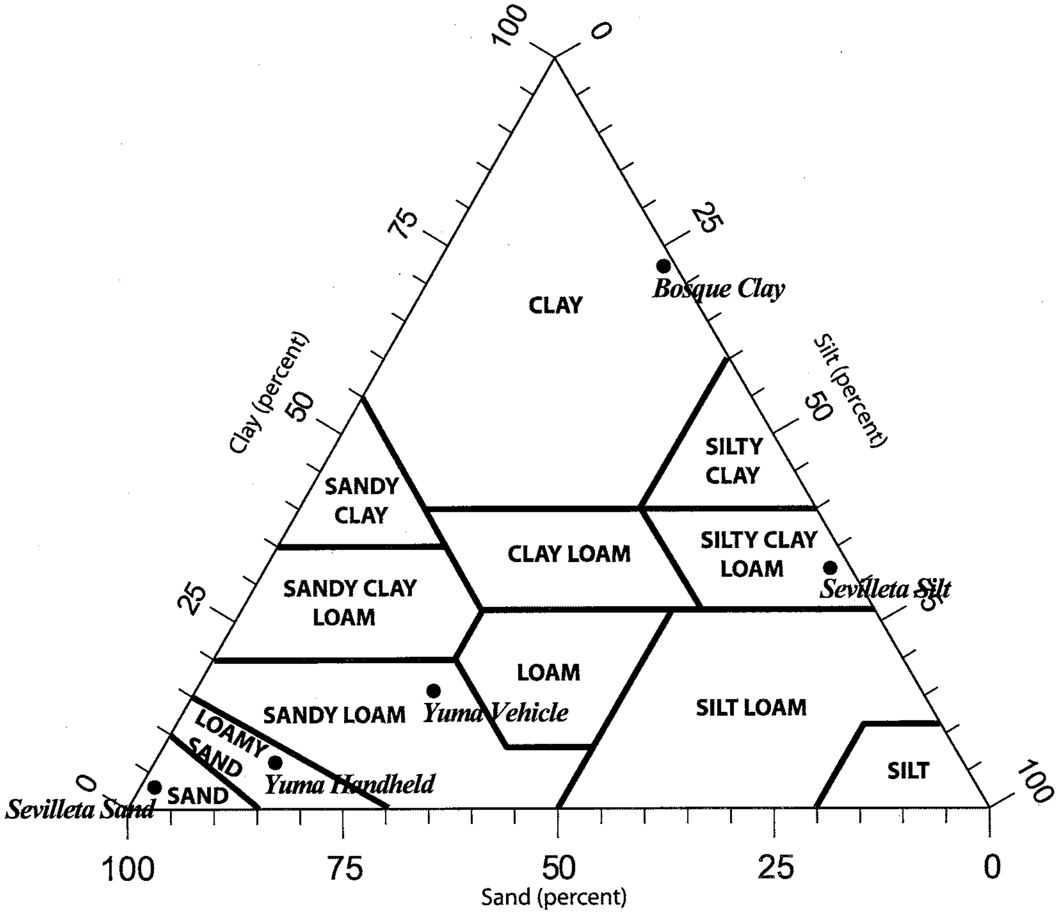

The clay site was located on the floodplain of the Rio Grande River in the Bosque Del Apache Refuge (See Figure 3.5). The soil had a textural composition of 1.3% sand, 26.5% silt, and 72.2% clay and a bulk density of 1.54 g/cm^3. It was classified by the USDA system as clay (See Figure 3.6).

The following describes the general procedures used for burying the landmines and Time Domain Reflectometry (TDR) probes at each of the sites listed above. First, a 3 by 3 meter plot was cleared of any grass, shrubs, or other obstacles. Then the soil surface was leveled so that the surface was flat without any sloping edges. Within this cleared area, a 2 by 1 meter area was chosen for the GPR frame. Inside the frame area two landmines were buried. First the antitank mine was buried 11 cm deep, 60 cm from the end of the frame, and 50 cm from the side (See Figure 3.7 (A) and (C)). An antipersonnel mine was buried 5 cm deep, 40 cm from the opposite end of the frame and 50 cm from the side (See Figure 3.7 (A)). The following procedures were used to bury the TDR probes. First a 1 meter line was measured from the center of the GPR frame out toward the edge of the site. Then a shallow hole was dug and an antitank landmine was placed in the hole. TDR probes labeled A, B, C, and D were buried at the following depths from the ground surface above and below the mine: probe A was buried at 3 cm, probe B at 8 cm, probe C at 23 cm, and probe D at 28 cm (See Figure 3.7 (B) and (D)).

3.5 Saline Water Infiltration Site

Beach environments with buried landmines have very saline soils, so to simulate this environment saline water with a concentration of approximately 34.5 g/L, the same as ocean water (Langmuir, 1997), was infiltrated into the Sevilleta sand soil (Refer to

Figure 3.7 Landmine and TDR probe burial geometry.

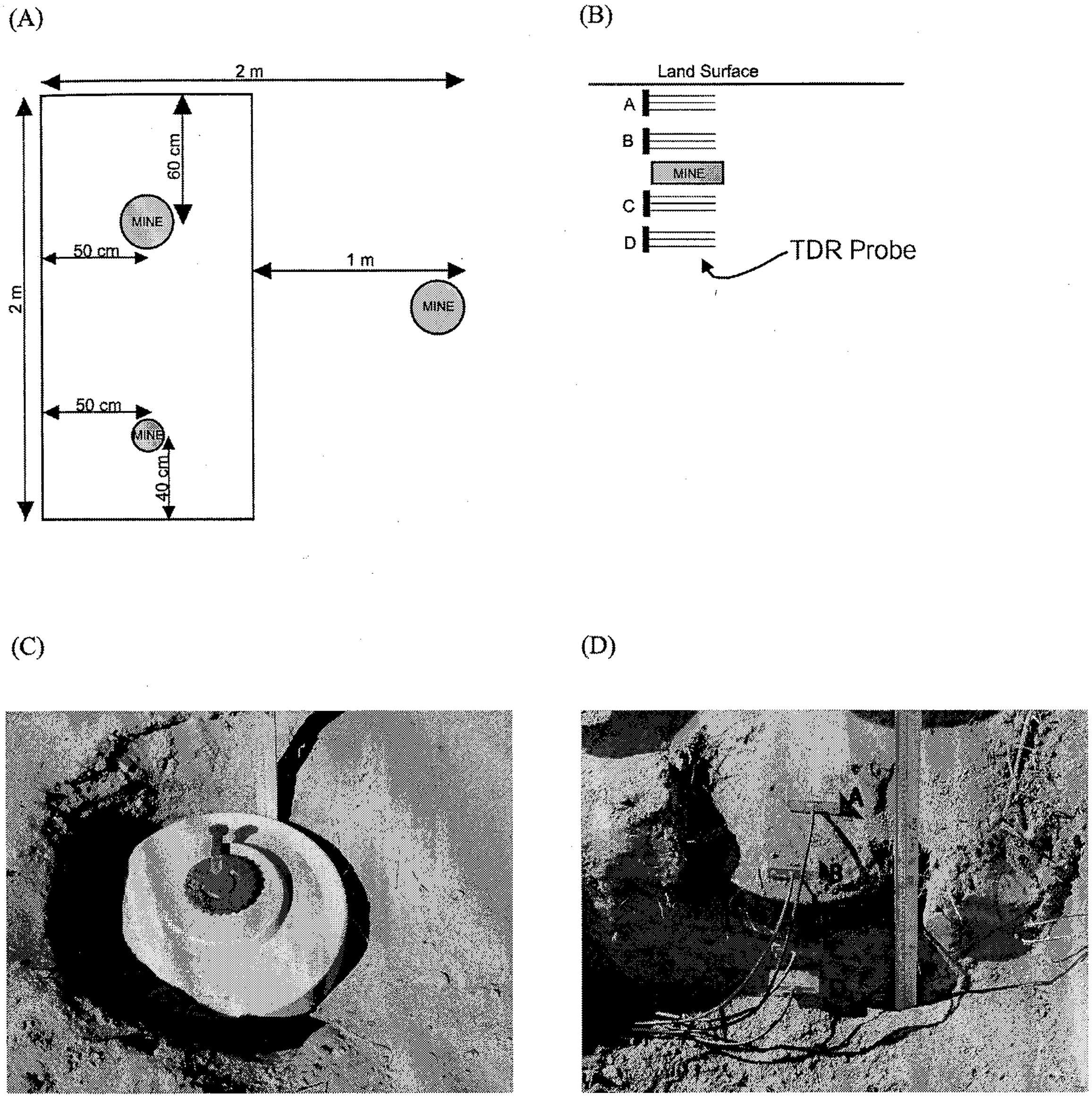

Section 3.4 for Soil and Site Description). The saline water mixture was prepared by adding 23 kilograms of granular road salt to 660 liters of water. The solution was then well mixed and the total dissolved solids (TDS) were measured using a HATCH ® TDS probe. The saline solution was applied to the site using the sprinkler system described in Section 3.1.

3.6 Field Sites in Yuma, AZ

The U.S. Army's Yuma Proving Grounds is located near the Arizona-California border, adjacent to the Colorado River, approximately 24 miles north of the city of Yuma, Arizona. The Countermine Testing and Training Range is located in the Kofa region of the area. In the Countermine Testing and Training Range there are two types of landmine lanes, first are the Handheld Detector Mine Lanes and second are the Vehicle-mounted Detector Mine Lanes. Both of these lanes have a mixture of nonmetallic and metallic, foreign and domestic defused antitank landmines. The soil types for these two mine lanes can be seen in Figure 3.6. The Yuma Handheld Detection Mine Lane has a soil composition of 79.6% sand, 13.9% silt, and 6.5% clay and is classified by the USDA classification scheme as a loamy sand. The Vehicle-mounted Detector Mine Lane has a soil composition of 57.1% sand, 28.4% silt, and 14.5% clay and is classified as a sandy loam.

3.7 GPR Operation and Basic Image Processing Techniques

Recall that the ground penetrating radar system used for landmine detection in this study was the pulseEKKO 1000 series. This model is manufactured by Sensors &

Software Ltd., Canada (See Figure 3.8). It comes with a transmitter and receiver that are connected to a central console. The console can then be connected to a portable computer, which is used to record a survey profile. The transmitter and receiver are attached to two separate antennas. There are several different antennas available for this model. The pulseEKKO 1000 can use the following frequency antennas: 110 MHz, 225 MHz, 450 MHZ, 900MHz, and 1200 MHz antennas. To select the right antenna, the user must know the approximate depth at which the objects to be located are buried. The 110 MHz antenna is used for deep exploration having a maximum depth of around 5+ meters. The 225 MHz is also used for deep explorations but is smaller, weighs less, and is more portable than the 100 MHz antenna. It has a maximum depth of penetration of around 2+ meters. The 450 MHz is used for deep explorations too, and it provides better resolution than the 110 and 225 MHz antennas. It has a maximum depth of about 2 meters. The 900 MHz antenna is designed for high resolution applications. It provides high spatial resolution for shallow objects and has a maximum depth of about 0.5 meters. The highest frequency antenna that is designed to be used with the pulseEKKO 1000 system is the 1200 MHz antenna. This antenna is for high resolution mapping of near subsurface objects. It has the highest spatial resolution and can be used for locating buried pipes and cables, and mapping concrete thickness.

To detect landmines or other objects with GPR the wavelength of the radar wave needs to be the same size or smaller than the object. In this study the 900 MHz antenna was chosen for detection of antitank landmines since the diameter of the landmines were 30 cm and one wavelength at 900 MHz, using the velocity of radar waves in air (2.997×10^8 m/s), measures 33.3 cm. Since the velocity of radar waves in soil will be

Figure 3.8 Diagram of GPR pulseEKKO 1000 system from Sensors & Software (1996).

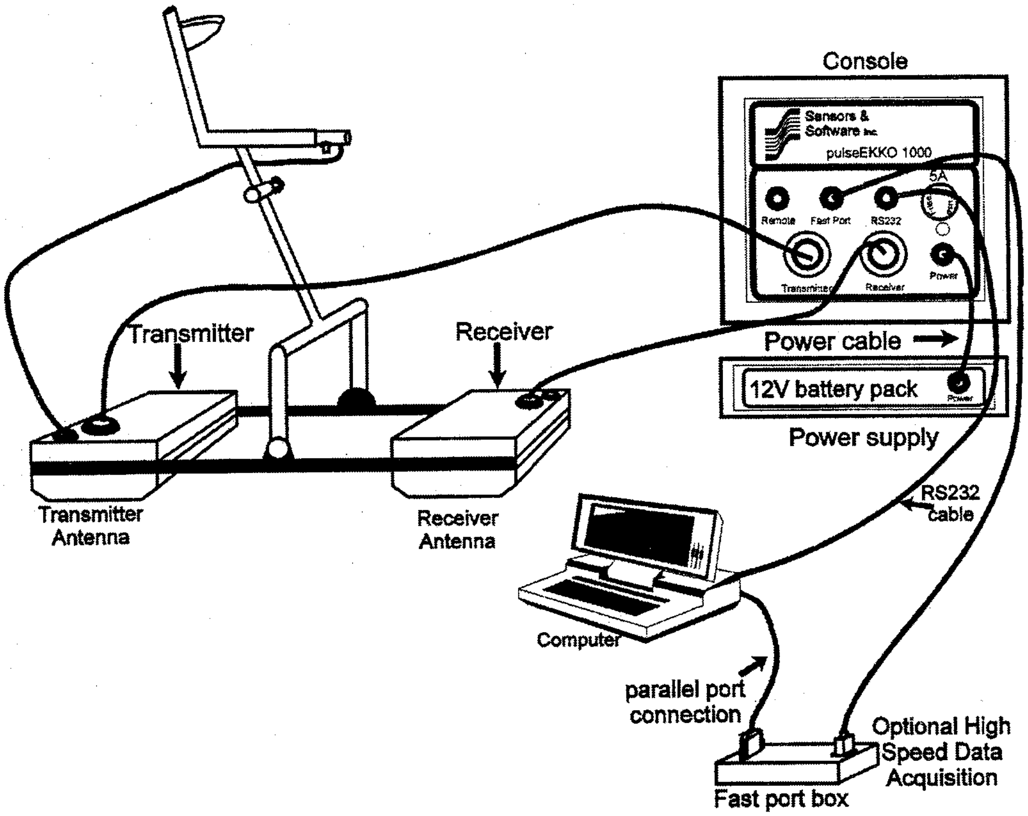

significantly slower than in air the wavelength will be less than the 33.3 cm.

For each antenna configuration described above, the antenna separation must be set to the correct distance. To calculate the correct antenna separation Equation (31) can be utilized.

$$S = \frac{2 * D}{\sqrt{(\varepsilon' - 1)}} \text{ (Sensors \& Software, 1996)} \qquad (31)$$

In Equation (31), S is the antenna separation distance, D is the depth to the buried object, and ε' is the relative permittivity (dielectric constant) of the host material. If the relative permittivity is not known for the survey area, a safe rule-of-thumb is to set S equal to 20% of the target depth. The 900 MHz GPR system requires an antenna separation of 17 cm and a step size of ≤2.5 cm is used when collecting surveys. If the spatial sampling (step size) is too large, the reflections arising from small targets (in our case landmines) may be effectively smoothed (aliased) and missed (Reynolds, 1997).

The following procedure was used to collect survey profiles at each soil site with the pulseEKKO 1000 radar system. First the system was assembled similarly to what is shown in Figure 3.8. After connecting the various cables and instruments, the system was placed on the GPR frame marked off in 2cm increments of the step size. At each point along the survey, multiple traces were collected and the average trace was recorded, this process is referred to as stacking. The number of stacks used at each point can be set in the software setting options and increasing the number of stacks helps to increase data quality. It is recommended to use a large number of stacks in environments that are cluttered and produce lots of noise. At each landmine test site 64 stacks were used. After the traces were collected, the GPR was moved along the transect collecting more traces while moved from point to point. The final product is a profile showing the subsurface arrangement.

There are a few processing settings that can be adjusted prior to data collection. Setting the gains was the only option utilized. There are six different types of gains available with the Sensors & Software package which includes the following: AGC, SEC, constant gain, no gain, auto gain, and user defined gain. The AGC gain stands for automatic gain control. It works by applying a gain that is inversely proportional to the signal strength, which works well in defining continuity of reflecting events, yet it does not preserve relative amplitude information. Hence, once the data has this type of gain applied to it, the strength of any particular reflector in relation to another can no longer be compared. Because this type of gain is inversely proportional to the signal strength, very small signals produce very large gains. As a consequence, some types of gain limiting standards need to be set.

AGC has two gain limiting settings. First is gain max manual, which allows the user to manually enter a maximum gain that is fixed for the whole data set. The second type is gain max auto. This type of gain limiting feature changes from trace to trace. The maximum gain is computed by finding the average signal level in the region. The maximum gain is then the value needed to increase the average signal to the percent imputed.

The second type of gain is the SEC, which stands for spreading and exponential compensation. This type of gain is a composite of a linear time gain and an exponential time gain. Due to its exponential form, this type of gain also has a gain limiting feature. The mathematical model is seen in Equation (32),

$$g(t) = C + \left(1 + \frac{\tau}{\tau_W}\right) e^{\beta\tau} \text{ (Sensors \& Software, 1996)} \qquad (32)$$

where C is a constant, $\tau = (\tau - (\tau_W + \tau_O))$, τ_W is the pulse width, τ_O is time zero, $\beta = \alpha * v/8.69$, α is the radar wave attenuation, and v is the radar wave velocity.

The third type of gain is constant gain. This applies a constant value that is multiplied by all data points in the profile. The fourth is no gain and this is used when no gain is necessary. The fifth is auto gain and this calculates and applies a gain based on calculating the decay of the average signal strength over time. The last type of gain is the user defined gain. For this gain the user makes an ASCII file with time in one column and the gain to be applied in the other column. This file is then loaded into the program and the computer applies the gain at each point corresponding to the ASCII file. For each of the landmine test sites, AGC gains were used with a gain max of 500.

For all GPR profiles of buried landmines presented in Section 4, Seismic Unix was used for post data collection image processing. Seismic Unix is a signal processing software package developed by the Center for Wave Phenomena at the Colorado School of Mines. This software offers many options for advanced signal processing (Stockwell and Cohen, 2001). One of the most common data processing techniques is filtering. Using Seismic Unix, a zero-phase, sine-squared tapered filter was applied to each image. The SUFILTER command was used to apply a highpass filter to each image. Then the SUWIND command was used to “zoom in” on the traces around where the landmine was located in the profile. Significant ground bounce appeared in the upper part of each GPR profile. This was caused by the signal bouncing off the ground and ringing between the two antennas. To delete this noise from the images the SUZERO command was used.

This has the effect of setting the amplitude to zero over a defined minimum and maximum range. After this the traces were plotted using the SUXWIGB command. This command generates an X-windows bitmap of the entire profile.

4 - RESULTS AND DISCUSSION

4.1 Model Predictions

The mathematical models described in Section 2.2.3 have been integrated into a MATLAB package (Borchers et al., 2000). In this section the soil properties of three field soils from the Socorro, New Mexico area (See Section 3.4 for details) are used as inputs into the MATLAB program to predict the effects that soil physical properties can have on soil electrical properties. The soil physical properties measured include bulk density and sand, silt, and clay distributions. The particle density was assumed to be 2.66 g/cm^3 for all of the soils used in this model.

4.1.1 Dielectric Constant versus Soil Water Content Predictions

Figures 4.1, 4.2, and 4.3 show how the complex dielectric constant changes with soil water content for the three soils described. In these figures the predicted real part of the dielectric constant (solid line) increases as the soil water content is raised, where the imaginary part (dashed line) remains almost constant over the entire range of soil water contents.

Figure 4.1 predicts that the real part of the dielectric constant will be 9.6 at 7% soil water content and 29.3 at 29% volumetric soil water content for the Sevilleta sand soil. Figure 4.2 predicts a value of 4.5 at 9% soil water content and 21.2 at 38% soil water content for the real part of the dielectric constant of the Sevilleta silt soil. Figure 4.3 predicts a value of 4 at 5% soil water content and 26.9 at 38% soil water content for the real part of the dielectric constant of the clay soil.

Relating this to landmine detection, if a nonporous plastic landmine is buried in a sand, silt, or clay soil then as the soil water content increases, the bulk dielectric constant of the soil also increases, while the dielectric constant of the landmine remains the same (about 3). This elevation in dielectric constant of the bulk soil will lead to a larger reflection coefficient (approaching unity), which in theory will lead to an improved image of the landmine. However, if the bulk dielectric constant and soil water content are the only factors examined when detecting nonmetallic landmines, one may come to the erroneous conclusion that for all soils landmine detection will improve with increasing soil water content because the dielectric constant contrast increases with elevated soil water contents.

Figure 4.1 **Dielectric constant versus soil water content for Sevilleta sand at 900MHz.**

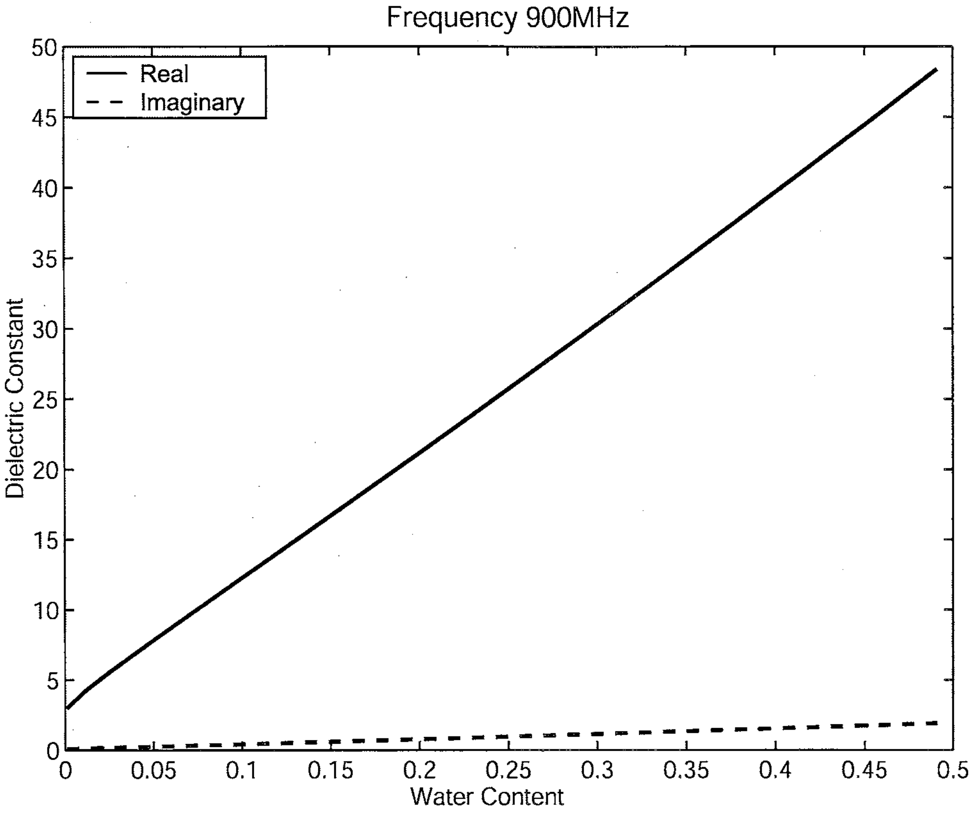

Figure 4.2 **Dielectric constant versus soil water content for Sevilleta silt at 900 MHz.**

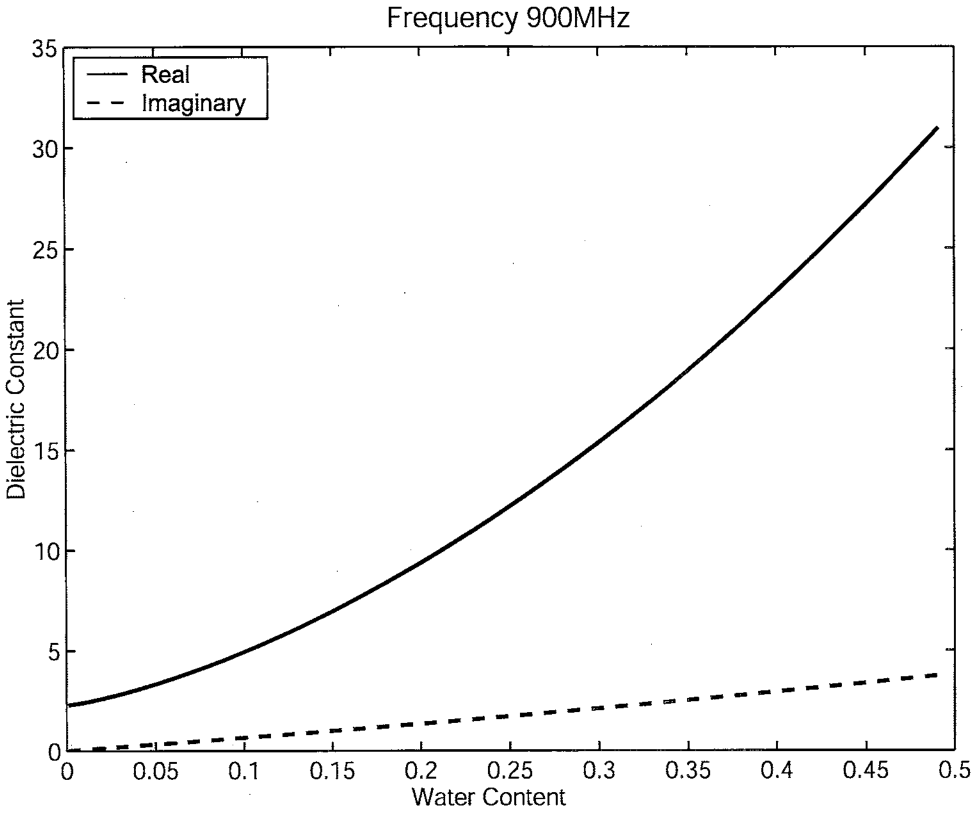

Figure 4.3 **Dielectric constant versus soil water content for Bosque Del Apache clay at 900 MHz.**

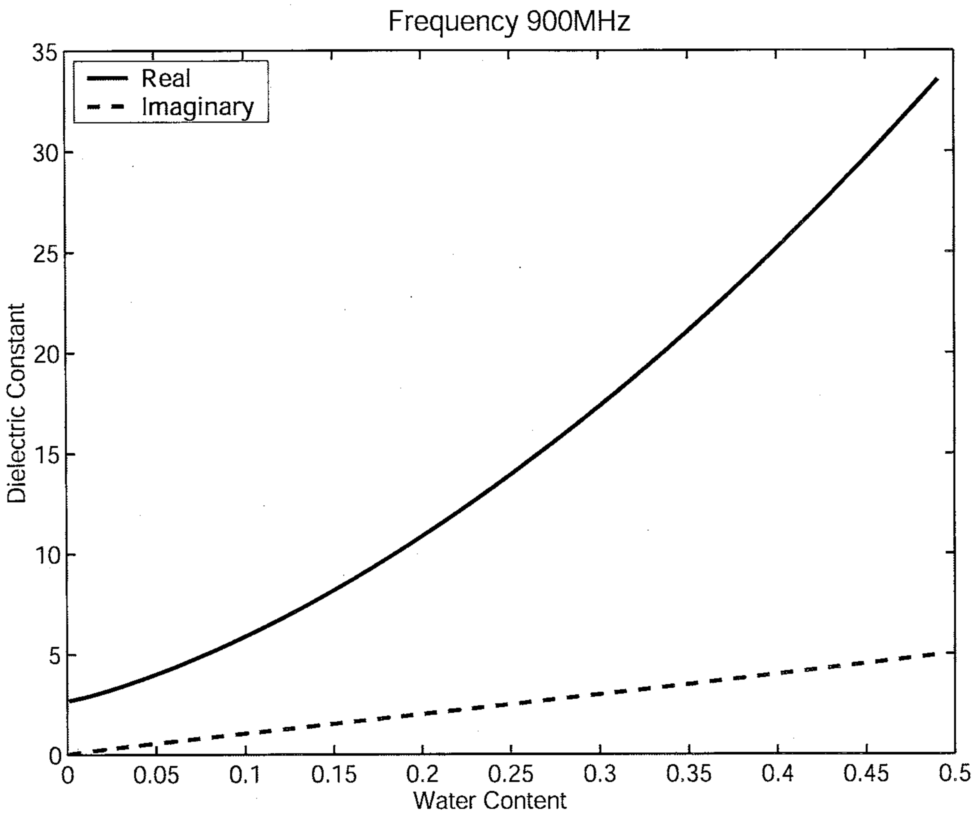

4.1.2 Dielectric Constant versus Frequency Predictions

The bulk dielectric constant of a soil will also change in response to the frequency of the radar waves. Figures 4.4, 4.5, and 4.6 show how the complex dielectric constant varies with frequency for the same soils at dry and saturated soil water conditions. The discontinuities seen in the lines predicting the real and imaginary parts of the dielectric constant over the 1.3 to 1.4 GHz range are caused because the high (Dobson) and low (Peplinski) frequency models were integrated together. These two models mentioned in Section 2.2.3 are only approximations and because of this they do not produce consistent results over the 1.3 to 1.4 GHz range.

In Figure 4.4, over the 0.3 to 1.3 GHz range, the imaginary part of the dielectric constant for sand is basically invariant for both the dry and saturated soil water conditions and does not appear to contribute a significant influence to the overall complex dielectric constant. Similarly, the real part is also constant over this low frequency range and at the two soil water contents. Over the high frequency range (1.3 to 6 GHz) the imaginary part of the dielectric constant increases slightly while the real part decreases for both soil water contents.

For the silt soil, the imaginary part of the dielectric constant decreases significantly over the 0.3 to 1.3 GHz range for both the dry and saturated soil water conditions. Over the 1.3 to 6 GHz range, the imaginary part of the dielectric constant increases slightly at 5% soil water content. The real part is invariant over the low frequency range for both dry and saturated soil water conditions, while the real part of the dielectric constant tends to decrease with increasing frequency, especially for the saturated soil water conditions (See Figure 4.5).

For the clay soil over the low frequency range (0.3 to 1.3 GHz), the imaginary part or loss term is extremely significant when the soil is saturated, changing by 7 over this range (See Figure 4.6). When the soil is dry, the imaginary part of the dielectric constant decreases but is not as significant (changing by 1 over this range) as when the soil is saturated. Over the high frequency range (1.4 to 6 GHz), the imaginary part of the dielectric constant increases when the soil is saturated and decreases slightly when the soil is dry. The real part over this range is constant for the dry clay soil and decreases slightly for the saturated clay soil.

Thus, from Figures 4.4, 4.5, and 4.6, it is clear that the frequency of the GPR system can cause the bulk dielectric constant of the soil to either increase or decrease depending on the frequency range used. Furthermore, over the lower frequency range (0.3 to 1.3 GHz), high clay content plays a significant role in elevating the imaginary part of the complex dielectric constant, as seen in the clay and silt soils.

Figure 4.4 **Dielectric constant versus frequency for Sevilleta sand at 7% and 29% volumetric soil water contents.**

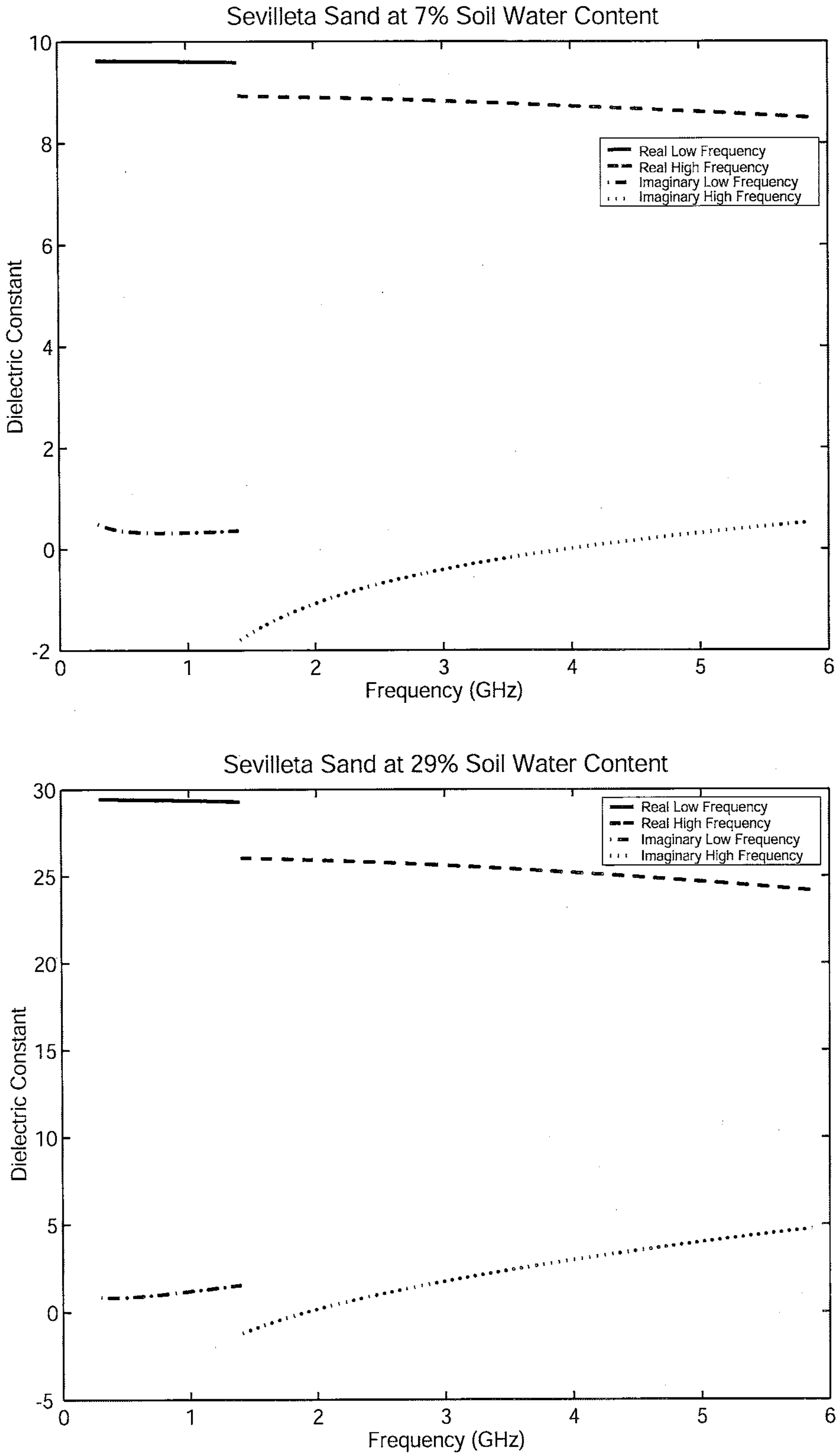

Figure 4.5 **Dielectric constant versus frequency for Sevilleta silt at 9% and 38% volumetric soil water contents.**

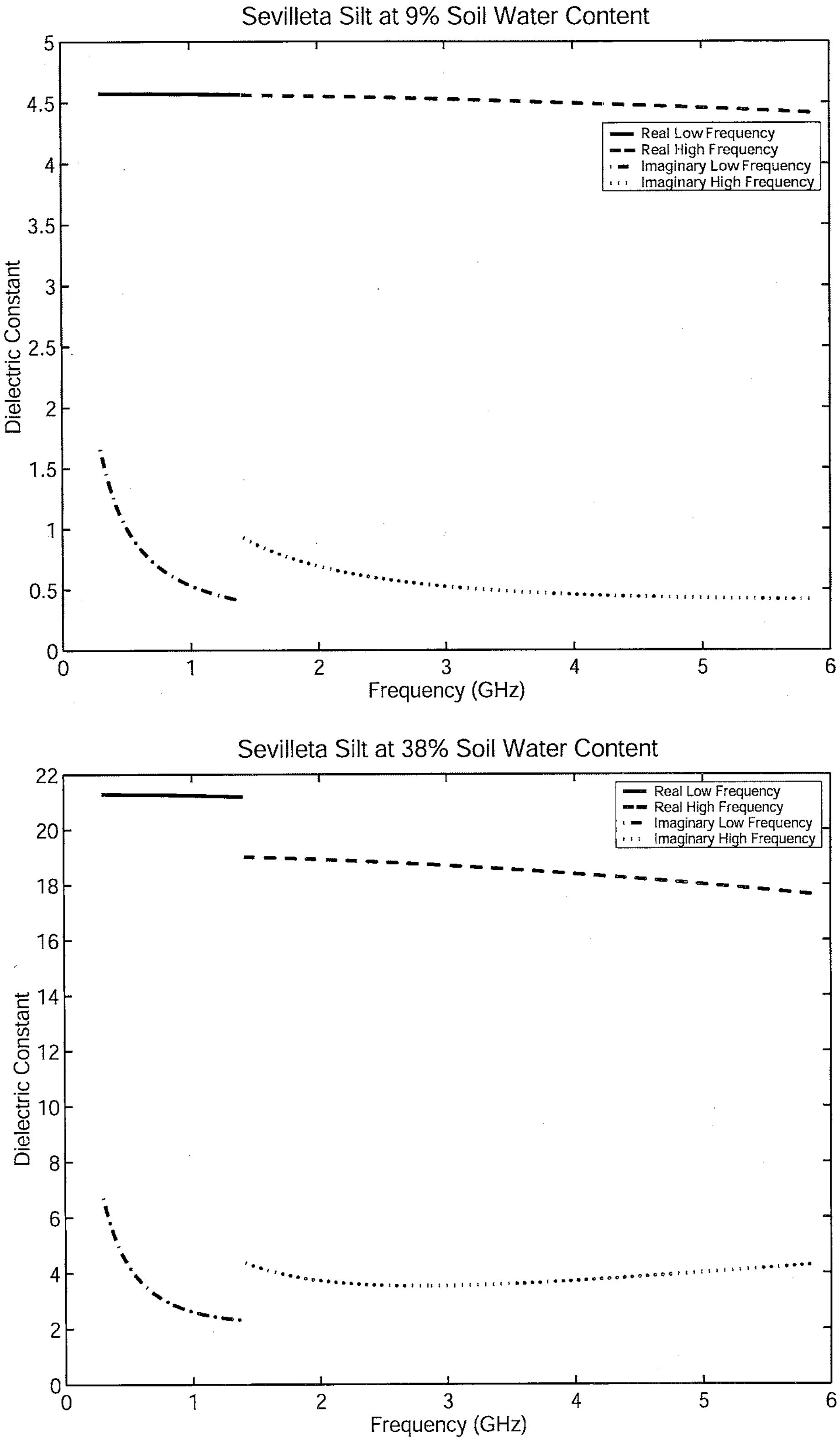

Figure 4.6 Dielectric constant versus frequency for Bosque Del Apache clay at 5% and 42% volumetric soil water contents.

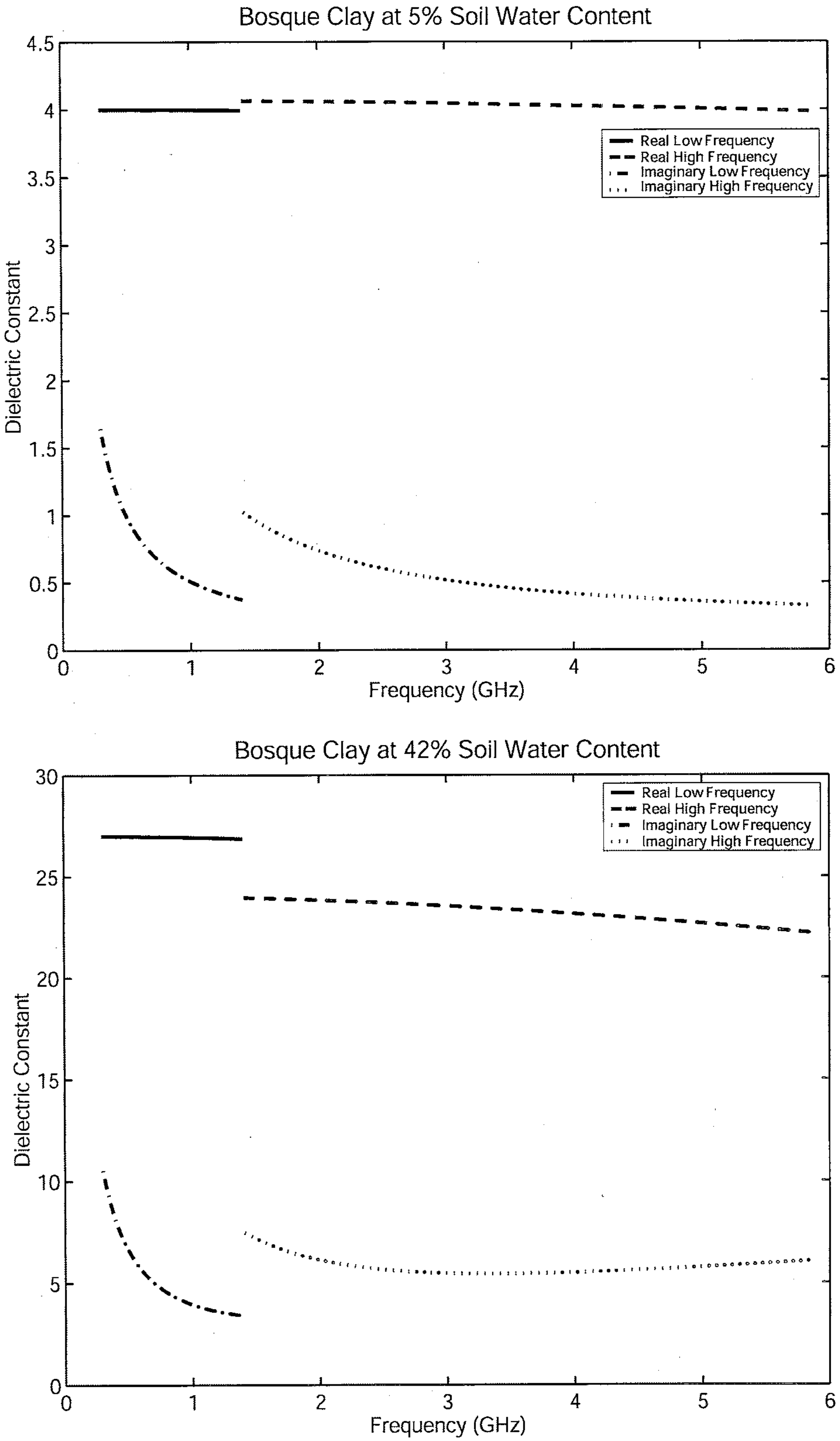
Bosque Clay at 5% Soil Water Content

Bosque Clay at 42% Soil Water Content

4.1.3 Dielectric Constant versus Soil Bulk Density Predictions

Along with frequency and soil water content, the complex dielectric constant will slightly change with variations in the bulk density of a soil. Figure 4.7 contains two plots showing how the complex dielectric constant of the Sevilleta sand soil changes as the bulk density is varied from 1.3 g/cm^3 to 1.9 g/cm^3 for both 7% and 29% volumetric soil water contents at 900 MHz. The imaginary part of the dielectric constant shows very little increase and can be assumed as constant as the bulk density is varied over the defined range. The real part of the dielectric constant over this same range of bulk densities increases slightly for both soil water conditions. The same is also true for the real part of the complex dielectric constant in the Sevilleta silt and Bosque clay soils; however, the Sevilleta silt and Bosque clay soils show a slight decrease in the imaginary part of the complex dielectric constant as the bulk density is increased (See Figures 4.8 and 4.9).

4.1.4 Dielectric Constant versus Soil Particle Density Predictions

Soil particle density appears to have a trivial effect on the complex dielectric constants of sand, silt, and clay soils. Figures 4.10, 4.11, and 4.12 are plots showing the relationship between particle density and dielectric constant for the Sevilleta sand and silt soils and the Bosque clay soil at 900 MHz for both dry and saturated soil water contents. In these figures, both the real and imaginary parts of the dielectric constant are invariant over the 2.4 to 2.8 g/cm^3 range. The Sevilleta silt soil shows a slight increase in the real and imaginary parts of the dielectric constant when the soil is dry (See Figure 4.11). The Bosque clay soil shows a slight increase in both the real and imaginary parts of the

Figure 4.7 **The relationship between bulk density and the dielectric constant for the Sevilleta sand soil at 900 MHz, 7% and 29% volumetric soil water contents.**

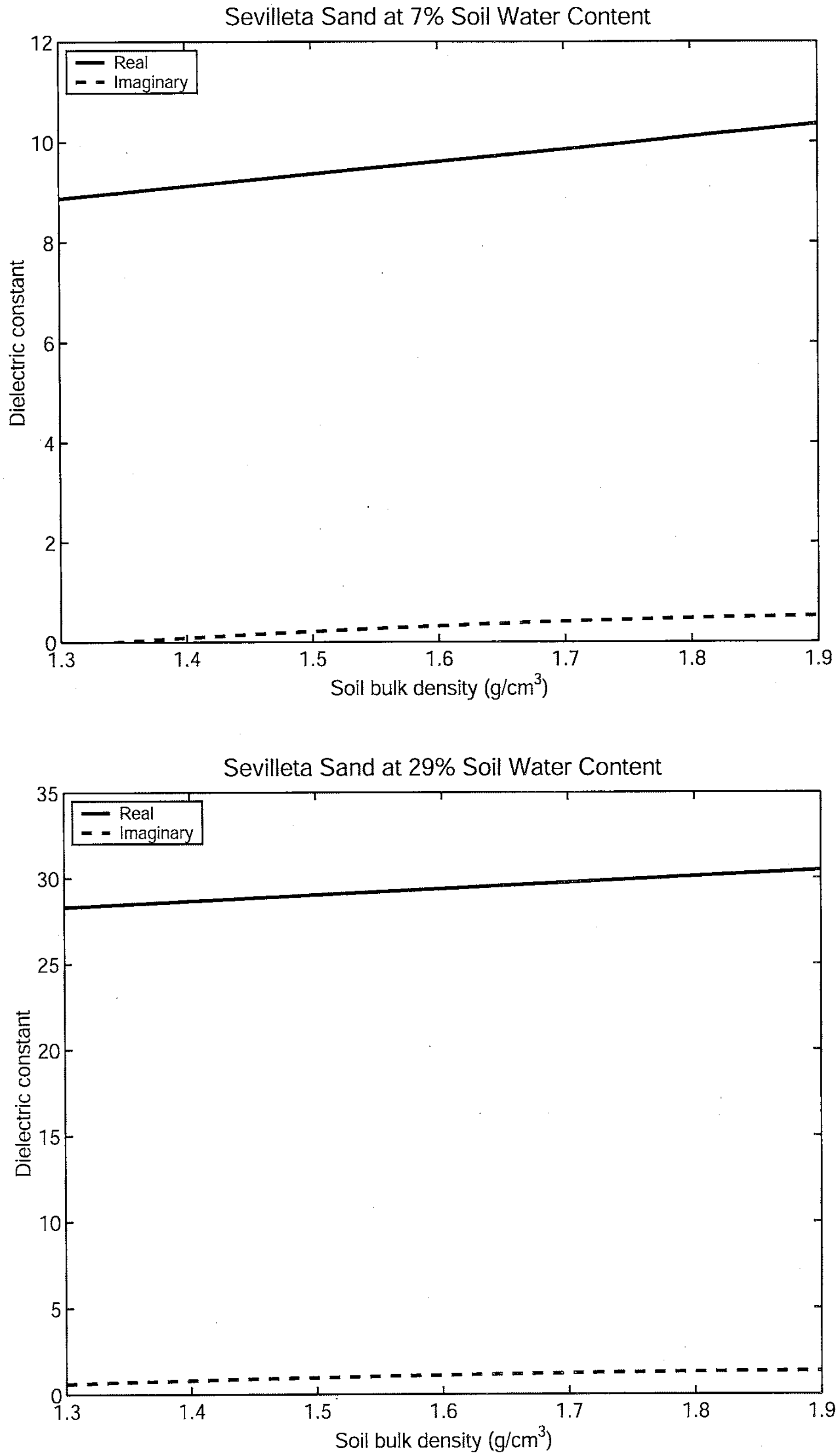

Figure 4.8 **The relationship between bulk density and the dielectric constant for the Sevilleta silt soil at 900 MHz, 9% and 38% volumetric soil water contents.**

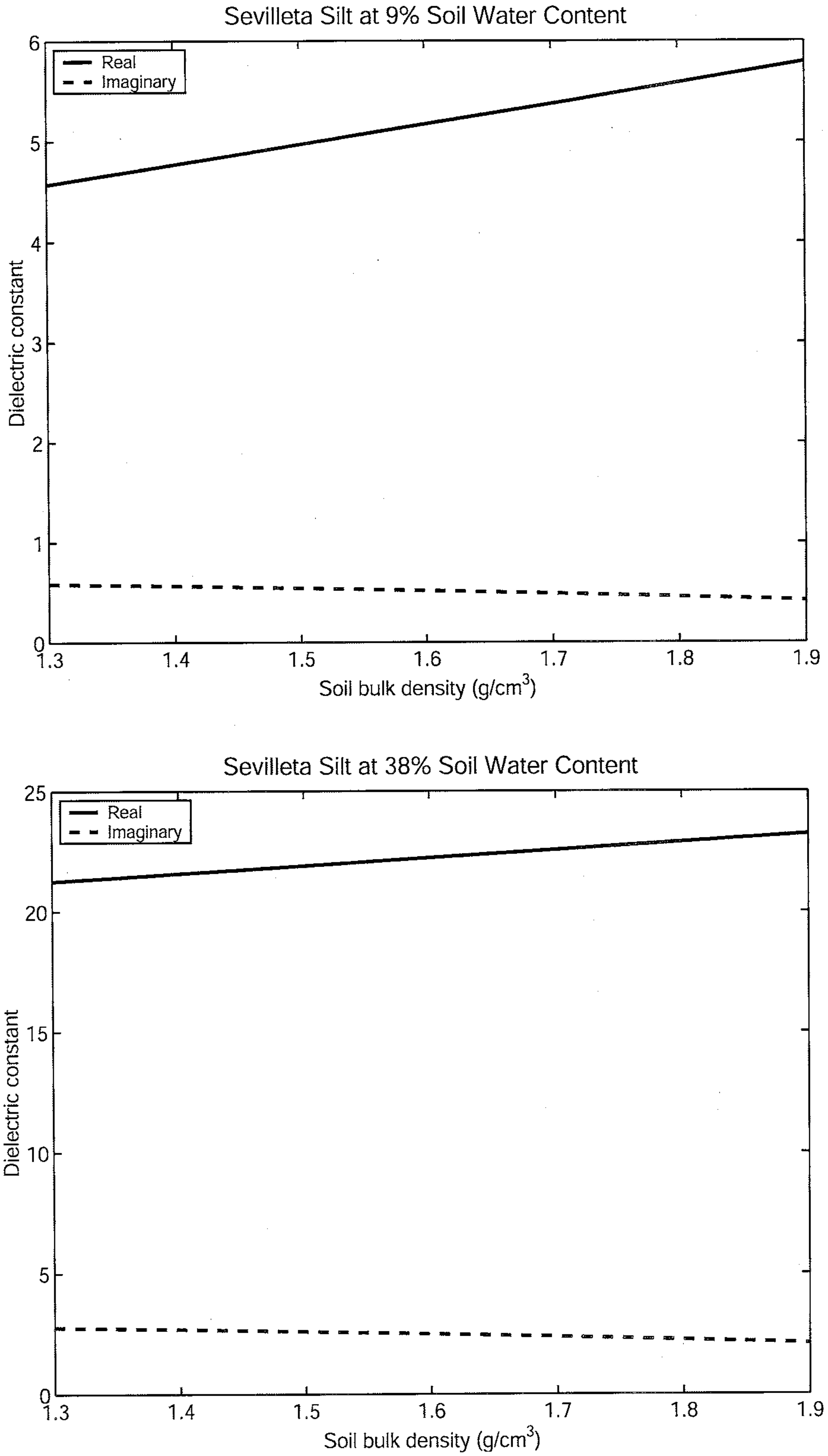

Figure 4.9 **The relationship between bulk density and the dielectric constant for the Bosque clay soil at 900 MHz, 5% and 42% volumetric water contents.**

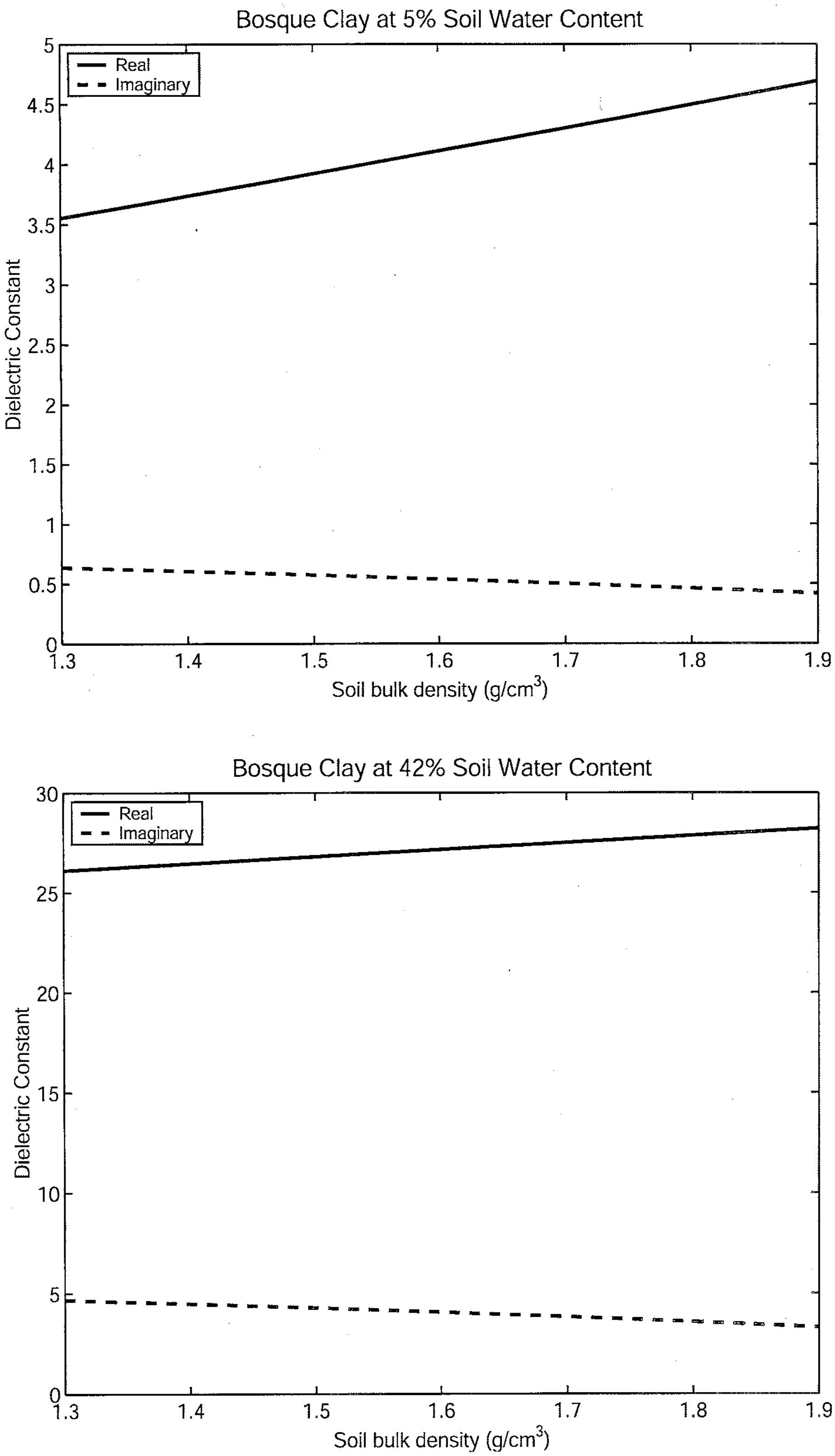

Figure 4.10 **The relationship between particle density and the dielectric constant for the Sevilleta sand soil at 900 MHz, and 7% and 29% volumetric soil water contents.**

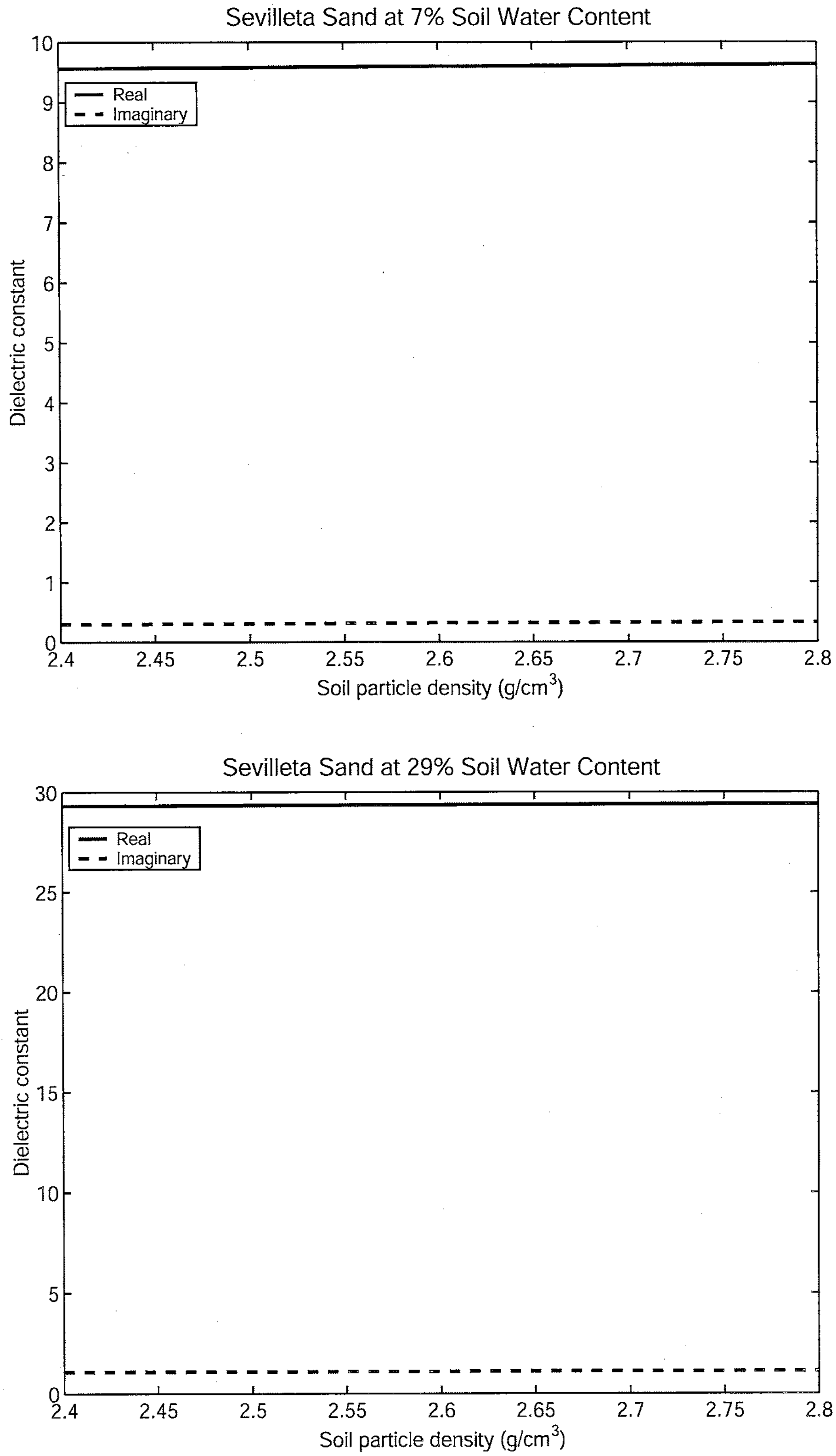

Figure 4.11 The relationship between particle density and the dielectric constant for the Sevilleta silt soil at 900 MHz, and 9% and 38% volumetric soil water contents.

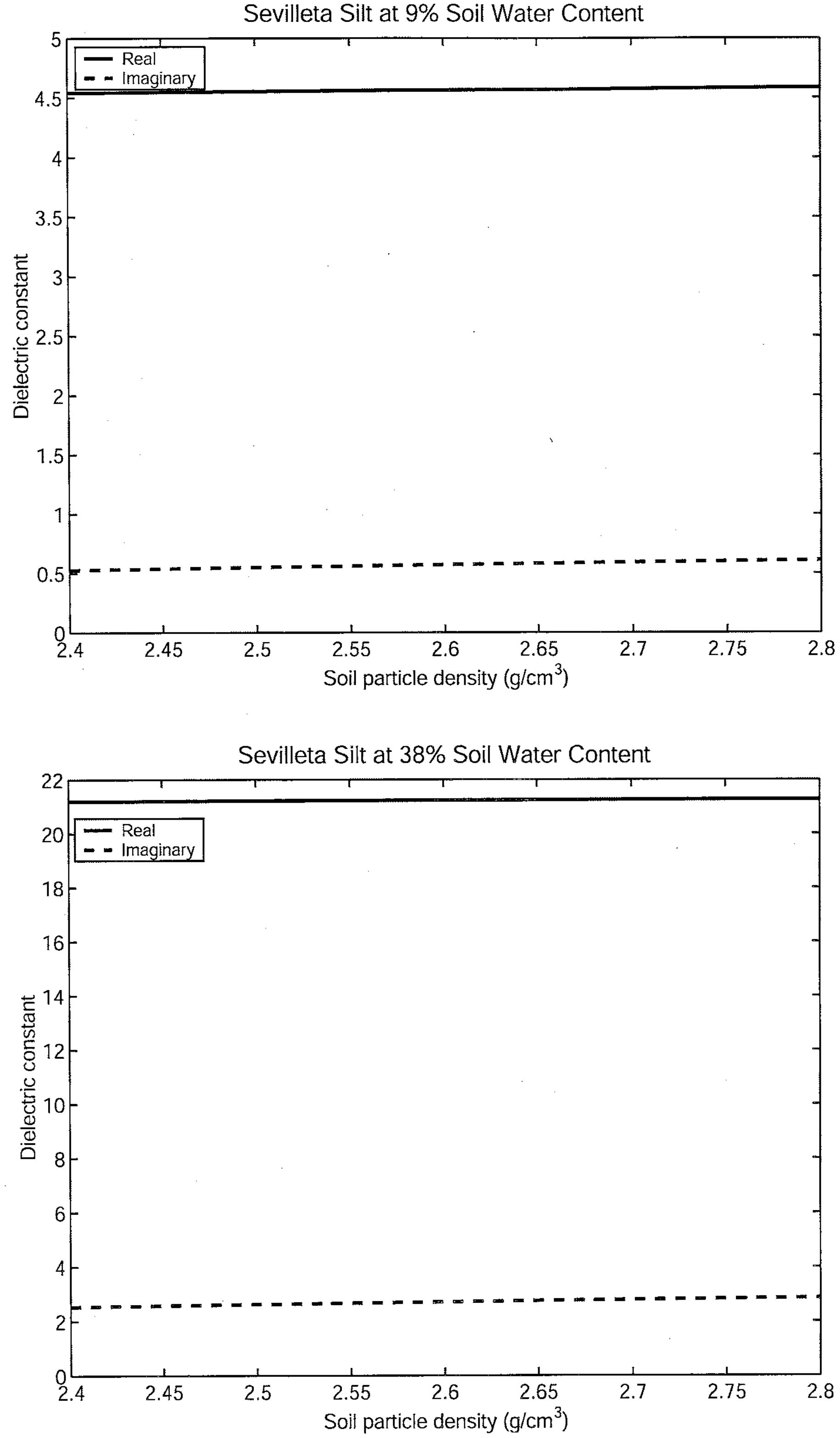

Figure 4.12 The relationship between particle density and the dielectric constant for the Bosque clay soil at 900 MHz, and 5% and 42% volumetric water contents.

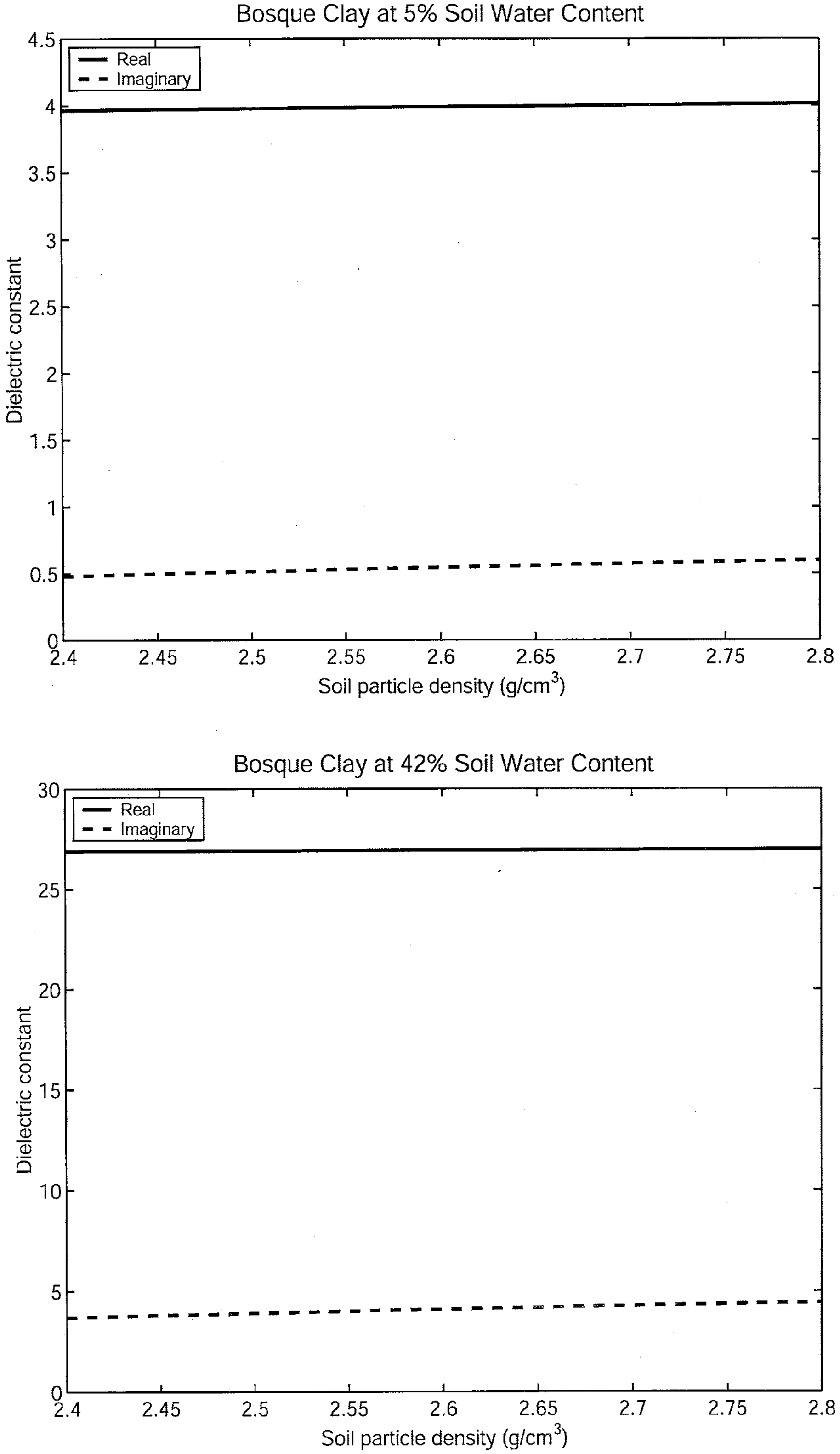

complex dielectric constant at higher particle densities under both dry and saturated soil water conditions (See Figure 4.12). Figures 4.7 through 4.12 illustrate that the bulk density and particle density of soils contribute very little to the variability of the complex dielectric constant when the soil is dry and saturated.

4.1.5 Attenuation and Radar Response

From Equations (11) and (12) it is clear that radar wave attenuation should increase as the frequency of the radar increases and as the ratio between the imaginary to real part of the dielectric constant increases. This ratio of real to imaginary part will generally increase as the soil water content is increased at a given frequency. In Figures 4.13, 4.14, and 4.15, the attenuation that corresponds with a range of soil water contents have been plotted for the three soils at 900 MHz using Equation (11). From these figures, it is obvious that as the clay content of the soil increases, so does the amount of attenuation at the higher soil water contents. The Sevilleta sand soil will attenuate about 20 db/m, where the Sevilleta silt soil will attenuate about 50 db/m, and the Bosque clay soil will attenuate about 65 db/m at 40% soil water content (Compare Figures 4.13, 4.14, and 4.15).

Figures 4.16, 4.17, and 4.18 show how changes in frequency relate to radar wave attenuation. As frequency increases, the attenuation of the GPR signal in sand, silt, and clay soils increases rapidly. The break in the plots between 1.3 and 1.4 GHz is again caused because of the integrating of the high and low frequency models together. High frequency radar is often used to enhance resolution because resolution increases with frequency, but as shown in these figures, signal attenuation increases quite dramatically at higher frequencies levels in all three types of soils.

Figure 4.13 **Attenuation versus soil water content for Sevilleta sand soil at 900 MHz.**

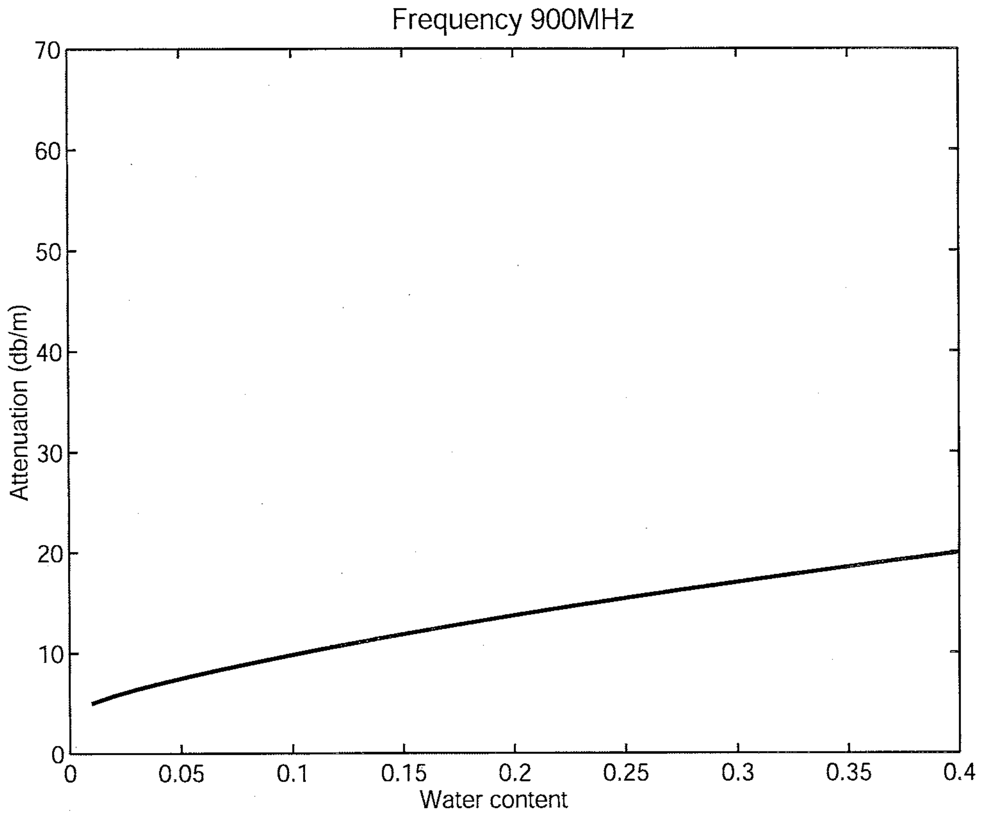

Figure 4.14 Attenuation versus soil water content for Sevilleta silt soil at 900 MHz.

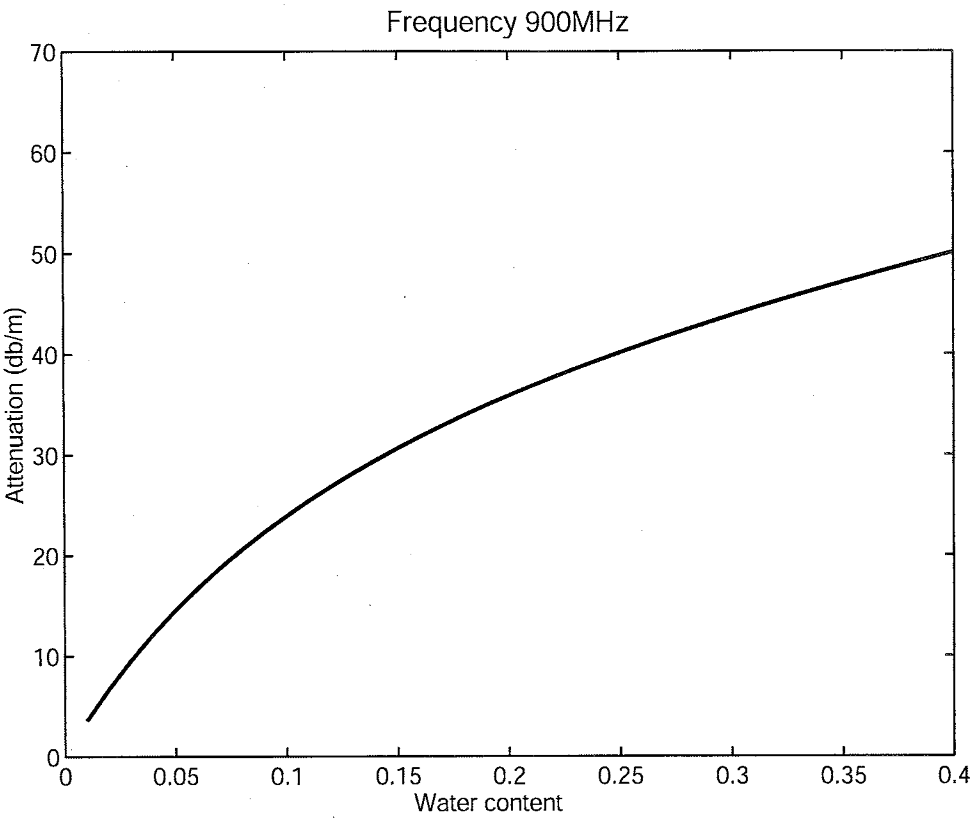

Figure 4.15 **Attenuation versus soil water content for Bosque Del Apache clay soil at 900 MHz.**

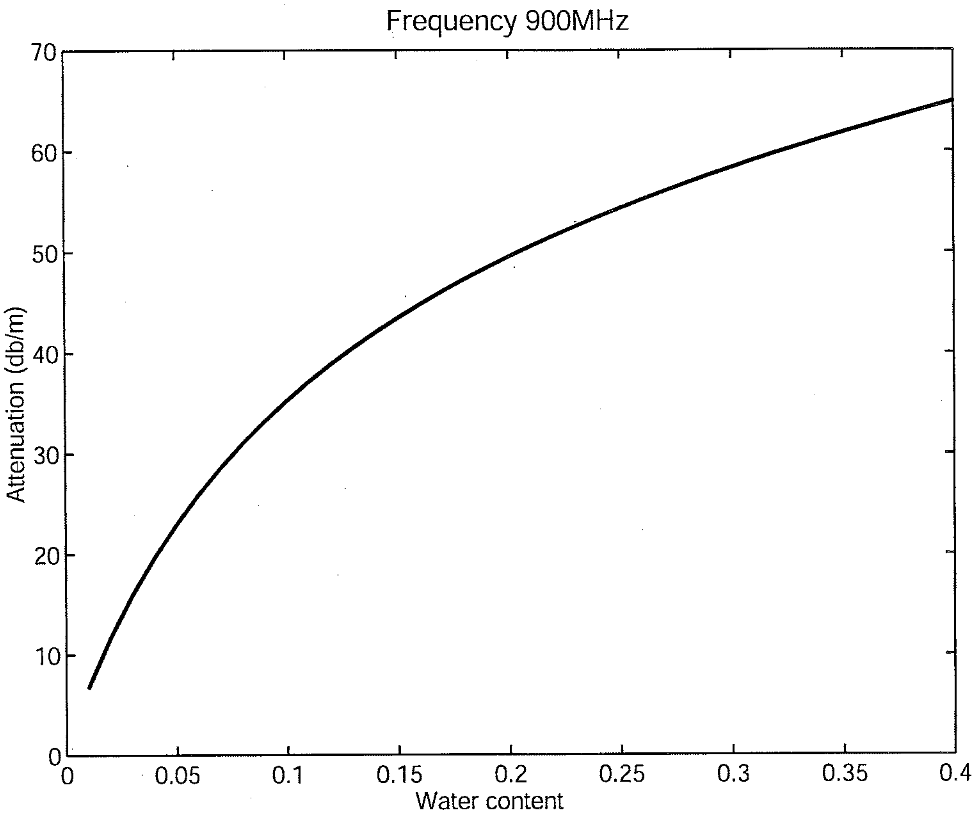

Figure 4.16 **Attenuation versus frequency for the Sevilleta sand soil at 7% (upper plot) and 29% (lower plot) volumetric soil water contents.**

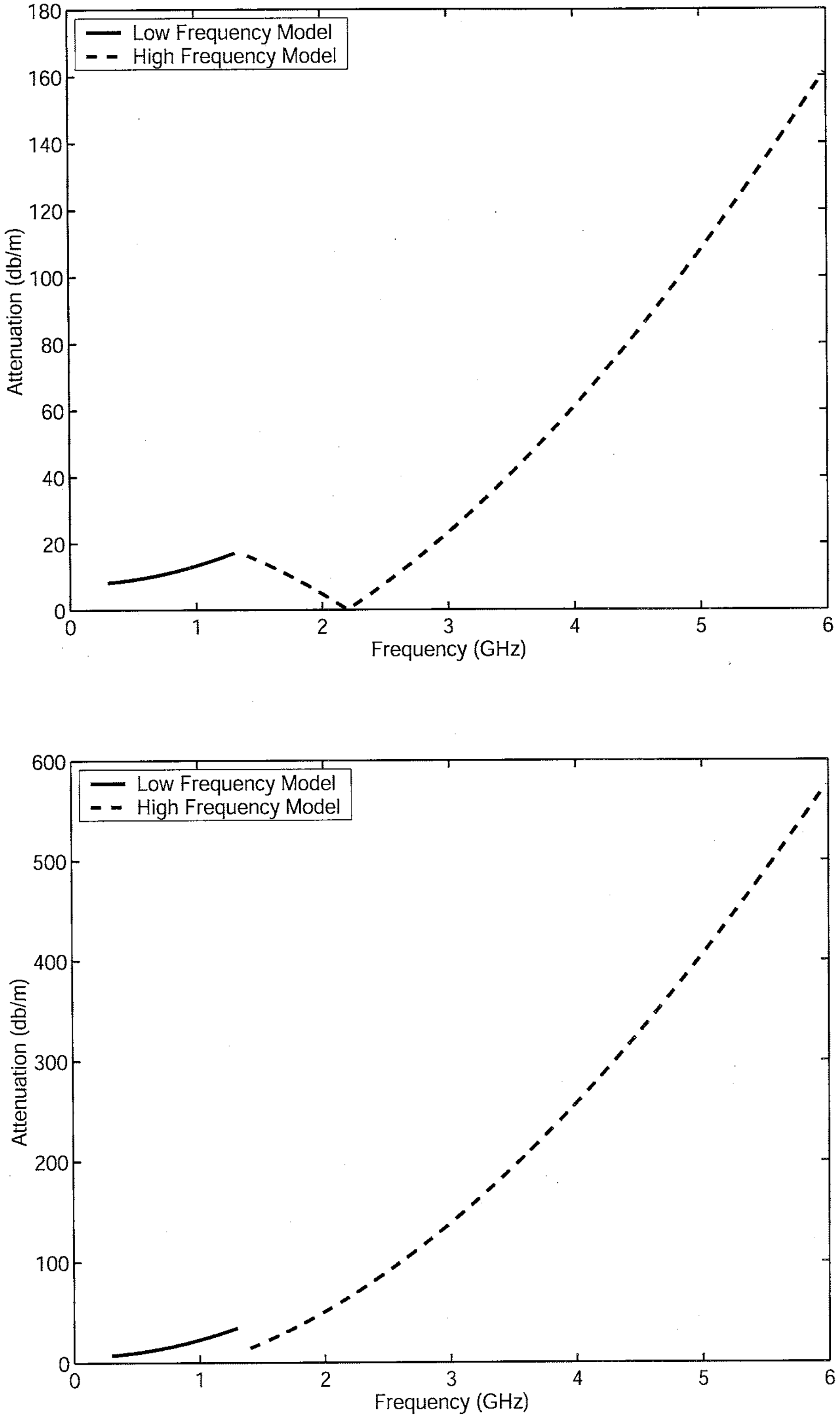

Figure 4.17 **Attenuation versus frequency for the Sevilleta silt soil at 9% (upper plot) and 38% (lower plot) volumetric soil water contents.**

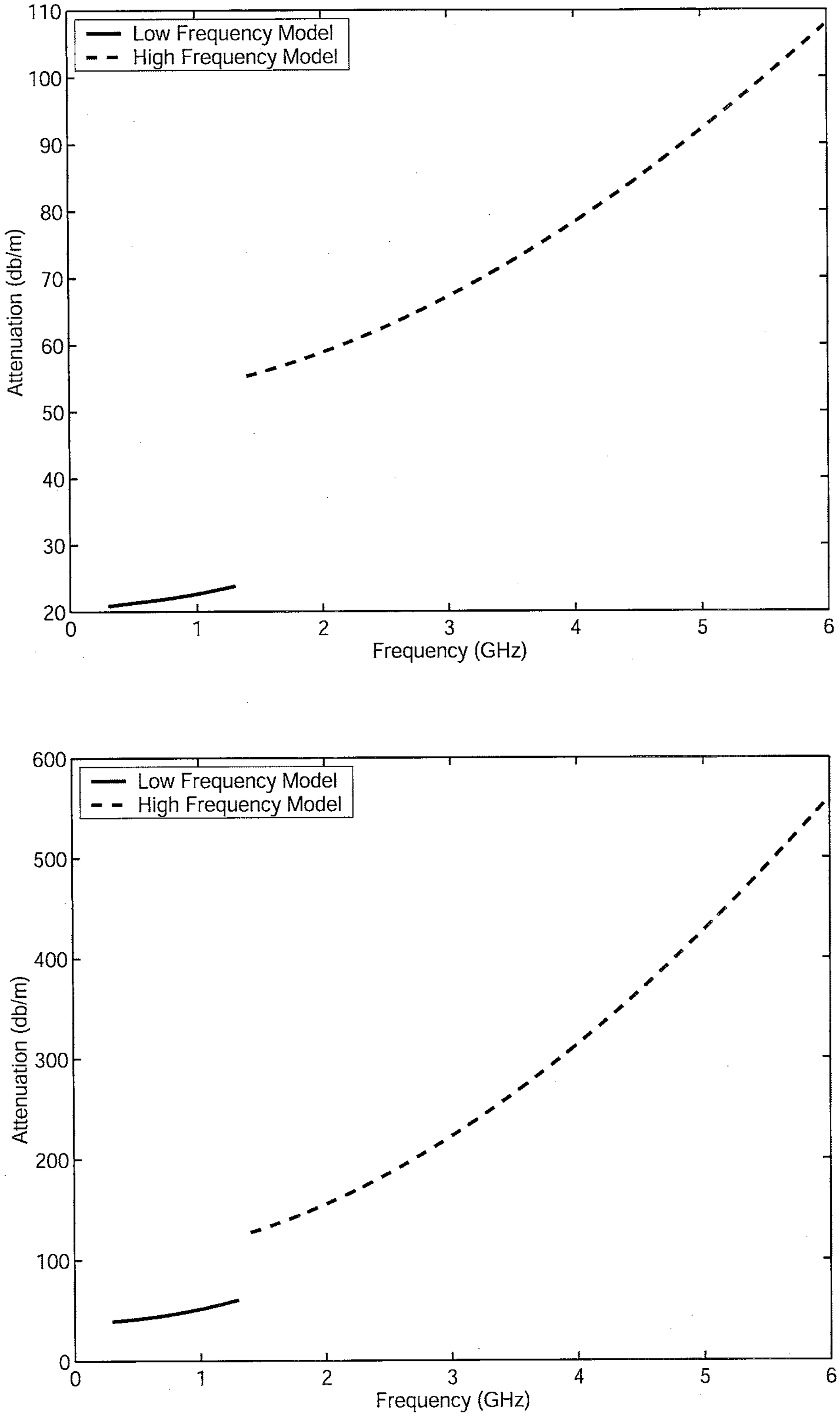

Figure 4.18 **Attenuation versus frequency for the Bosque Del Apache clay soil at 5% (upper plot) and 42% (lower plot) volumetric soil water contents.**

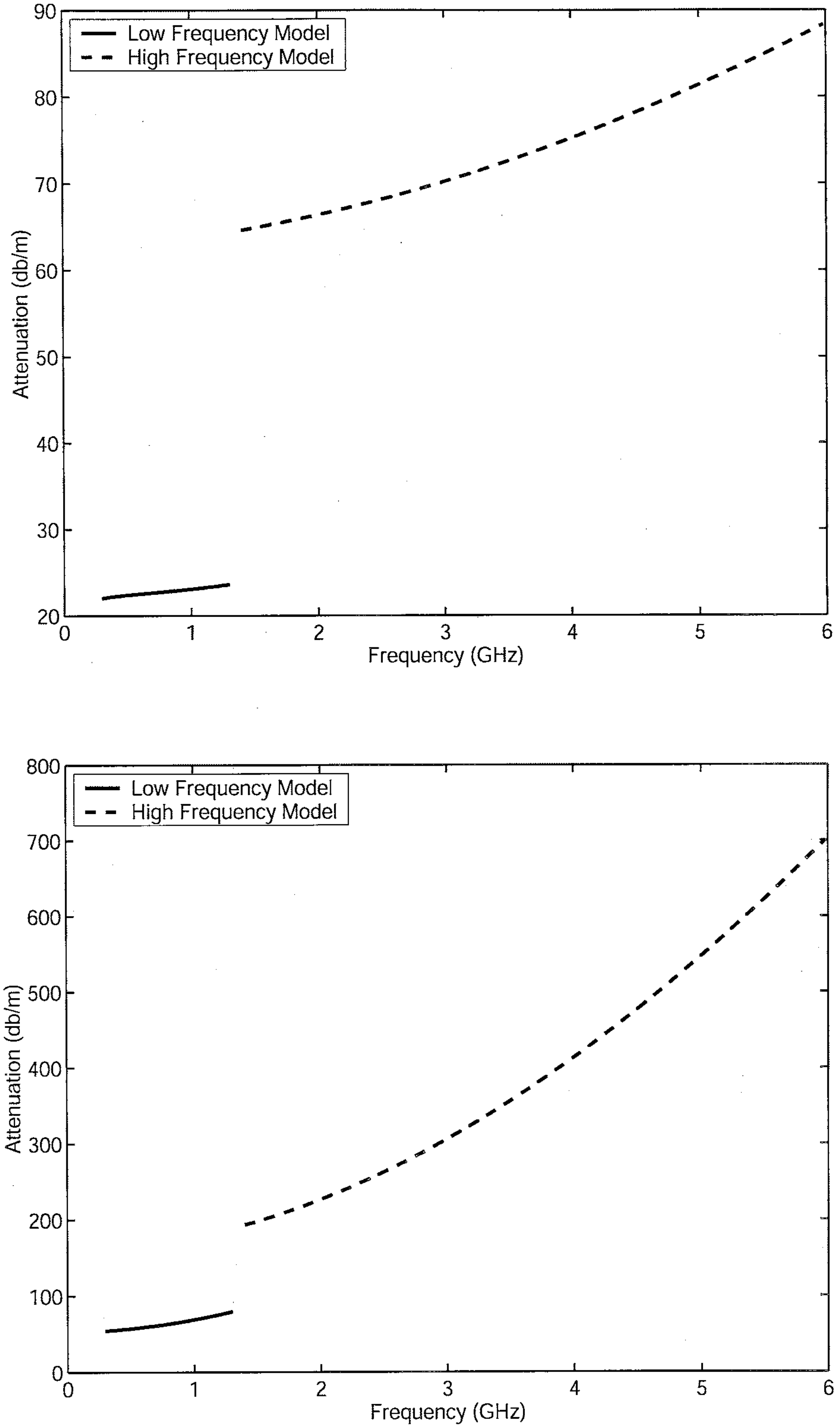

4.2 Field Results

4.2.1 Results from Socorro, NM Test Sites

This section presents GPR wiggle trace plots of the simulant landmines buried in the field soils described in Section 3.4. However, before the field data is presented a brief introduction and explanation of how GPR detects buried objects is presented. Figure 4.19 (A) shows a radar system being moved along the surface of the earth with numbers 1 through 5 representing locations where traces are collected. Figure 4.19 (B) shows the resulting wiggle trace plot representing the two dimensional cross section of the buried landmine. In this figure, tracing out the first arrivals from the buried landmine at each trace forms a hyperbola, this line is seen in Figure 4.19 (B). This hyperbola shape is formed because the first arrivals at points 1 and 5 take the longest time, the first arrivals at points 2 and 4 take an intermediate time, and the first arrival at point 3 take the least amount of time to reflect off the mine. In the following images presented this hyperbola shape is seen in some of the images, however, a line has not been drawn representing this feature. Instead an arrow points to the location of the buried landmine.

At each of the sites where GPR data was collected, TDR measurements of volumetric soil water content were also collected. Figure 4.20 shows the soil water content profile above and below the buried landmine. The top two measurements (3 and 8 cm) were averaged and this value was reported for the volumetric soil water content in each GPR profile.

Figure 4.21 is a profile of the Sevilleta sand site prior to landmine burial. Figure 4.22 is a profile of the same soil after the landmine had been buried for 1 day. The volumetric soil water content above the landmine in this profile is 7%. The simulant

Figure 4.19 **Conceptual illustration of radar reflection from buried landmine (A) and resulting GPR wiggle trace plot (B).**

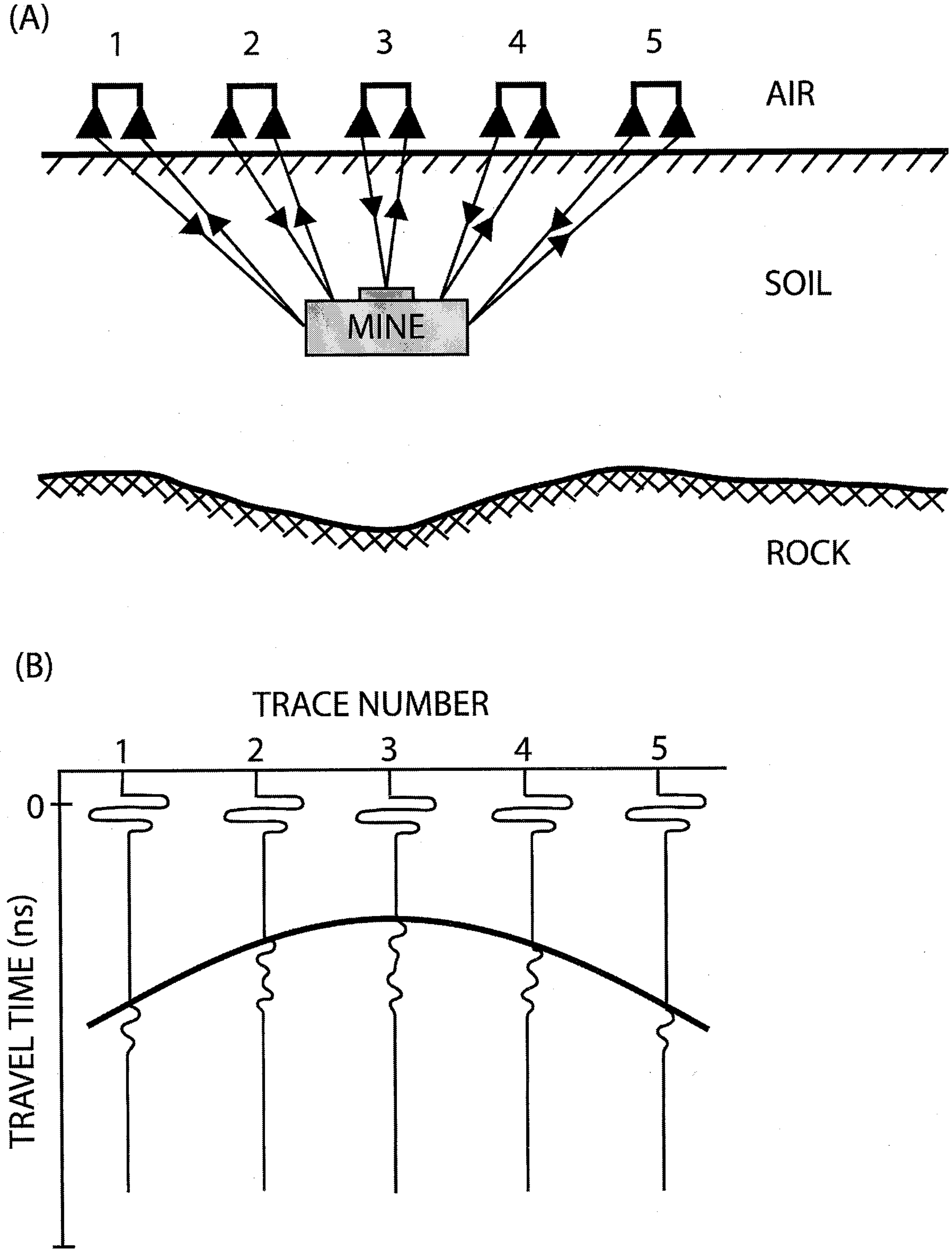

Figure 4.20 A sequence of plots showing the volumetric soil water contents above and below the buried landmine at each of the landmine test sites.

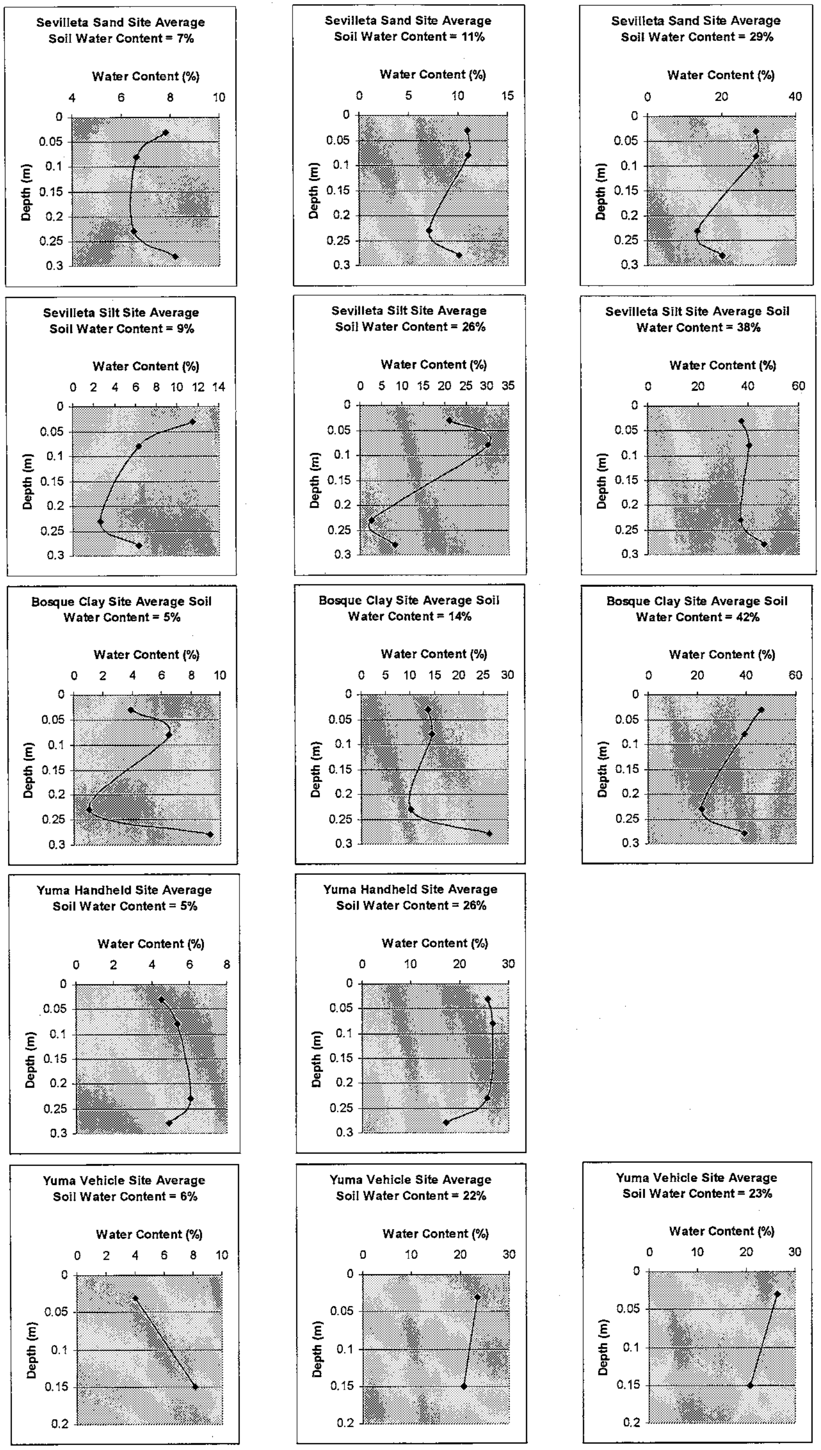

Sevilleta Sand Site Average Soil Water Content = 7%

Sevilleta Sand Site Average Soil Water Content = 11%

Sevilleta Sand Site Average Soil Water Content = 29%

Sevilleta Silt Site Average Soil Water Content = 9%

Sevilleta Silt Site Average Soil Water Content = 26%

Sevilleta Silt Site Average Soil Water Content = 38%

Bosque Clay Site Average Soil Water Content = 5%

Bosque Clay Site Average Soil Water Content = 14%

Bosque Clay Site Average Soil Water Content = 42%

Yuma Handheld Site Average Soil Water Content = 5%

Yuma Handheld Site Average Soil Water Content = 26%

Yuma Vehicle Site Average Soil Water Content = 6%

Yuma Vehicle Site Average Soil Water Content = 22%

Yuma Vehicle Site Average Soil Water Content = 23%

landmine in this figure is indicated by the hyperbolic feature below the twenty trace mark on the horizontal scale. Figure 4.23 is a profile of the same site after the volumetric soil water content above the landmine was raised to 11%. This profile was captured 14 days after the landmine was buried. The simulant landmine is again indicated by the hyperbolic feature under the twenty trace mark. Figure 4.24 shows the same profile but after raising the volumetric soil water content above the landmine to 29%. This image was also taken 14 days after the landmine was buried and the landmine is again indicated by the hyperbolic feature under the twenty trace mark. Both GPR profiles seen in Figures 4.23 and 4.24 were imaged within the same day of water application. These figures clearly demonstrate that raising the volumetric soil water content of dry sandy soils can enhance the ability of the GPR to image landmines buried in these soils, which is in agreement with what our model suggests.

Figure 4.25 shows a GPR wiggle trace plot of the Sevilleta silt loam site before the landmine was buried. This profile was imaged under dry field conditions, at approximately 9% volumetric soil water content. Figure 4.26 was also imaged under the same volumetric soil water content and after the simulant landmine was buried for 1 day. The landmine in the figure plot is difficult to see, showing only a slight indication of a diffraction tail below the 20 trace mark. This is because of the low contrast between the bulk dielectric constant of the soil and the dielectric constant of the landmine. Figure 4.27 was imaged after raising the volumetric soil water content above the landmine to 26% and 14 days after landmine burial. Again, the landmine is difficult to image. Figure 4.28 shows a very clear hyperbola directly under the 20 trace mark. This image was taken after the volumetric soil water content was raised to 38% above the buried simulant landmine and 15 days after its burial. In both Figures 4.27 and 4.28, the GPR profile was captured within the same day of water application. These figures demonstrate that for dry silt loam soils, the image of buried landmines can be improved by increasing the soil water content above the landmine.

Applying water to very dry clay soils, however, does not appear to enhance detection. Figure 4.29 shows a GPR wiggle trace plot from the Bosque Del Apache clay soil site before the landmine was buried. Figure 4.30 is an image taken during dry field conditions, with 5% volumetric soil water content above the landmine and one day after burial. The landmine is detectable under the dry clay soil conditions shown in this figure. The landmine in this figure is shown by the hyperbolic feature directly below the 35 trace mark on the horizontal scale. Figure 4.31 is an image that was taken after water was ponded for several weeks on the surface of the landmine test site, raising the volumetric soil water content to 14% above the landmine. The landmine in this figure is still detectable, but the strength of the signal is diminished (Compare Figures 4.30 to 4.31). Figure 4.32 shows an image of the same clay soil after ponding a total of 2700 liters of water over a 2 month period, raising the volumetric soil water content to 42% above the landmine. After application of large amounts of water, the landmine is clearly invisible to GPR. This is expected because in clay soils the electrical conductivity is high and adding water greatly increases the attenuation of the radar, as our model suggests (Refer to Figure 4.15).

Figure 4.21 Wiggle trace plot of the Sevilleta sand soil site at 7% volumetric soil water content preceding landmine burial, imaged using a 900 MHz GPR system.

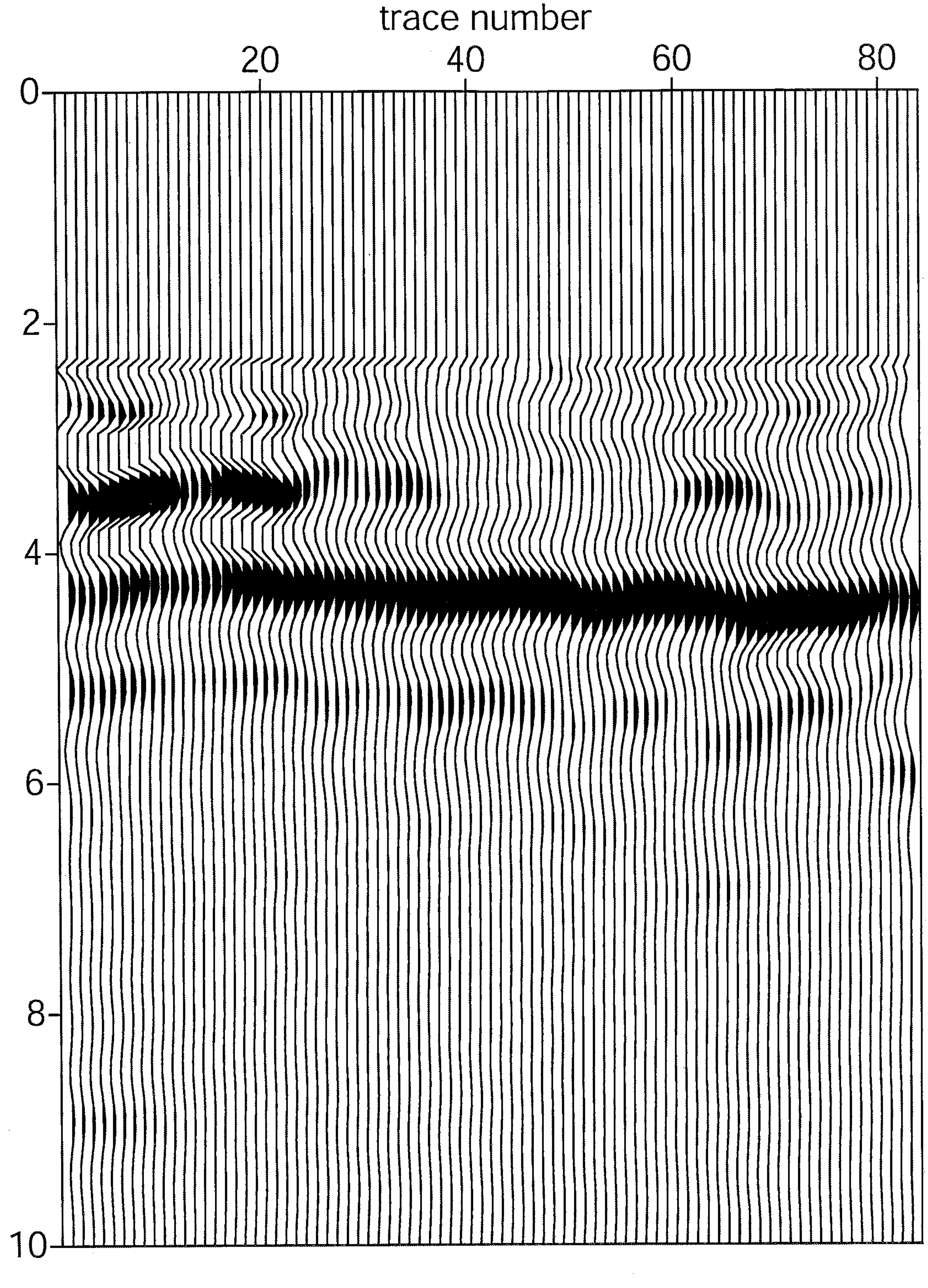

Figure 4.22 Wiggle trace plot of a silicon rubber simulant antitank landmine buried 11 cm below the ground surface in the Sevilleta sand soil at 7% volumetric soil water content, imaged one day after burial using a 900 MHz GPR system.

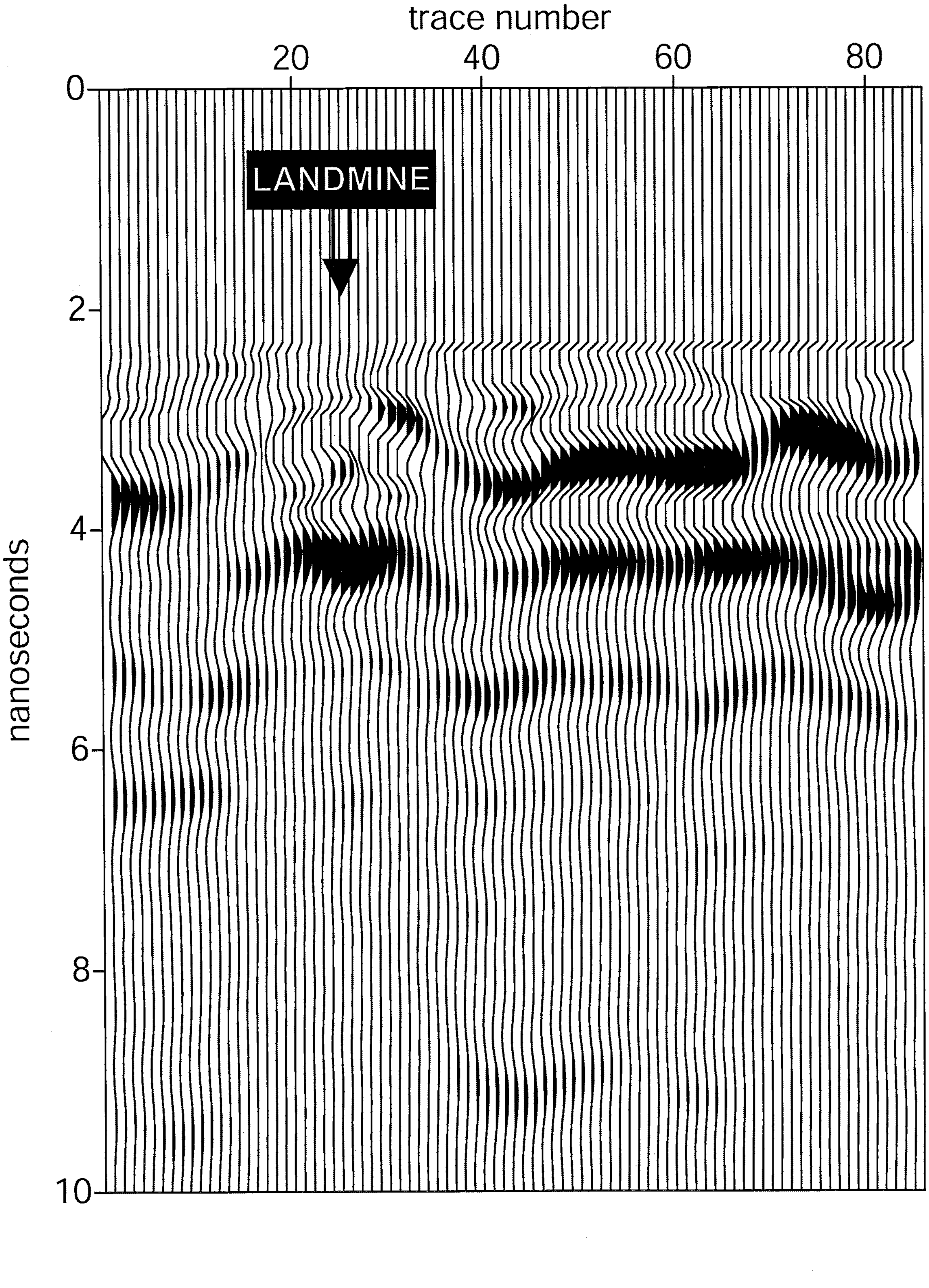

Figure 4.23 Wiggle trace plot of a silicon rubber simulant antitank landmine buried 11 cm below the ground surface in the Sevilleta sand soil at 11% volumetric soil water content, imaged 14 days after burial using a 900 MHz GPR system.

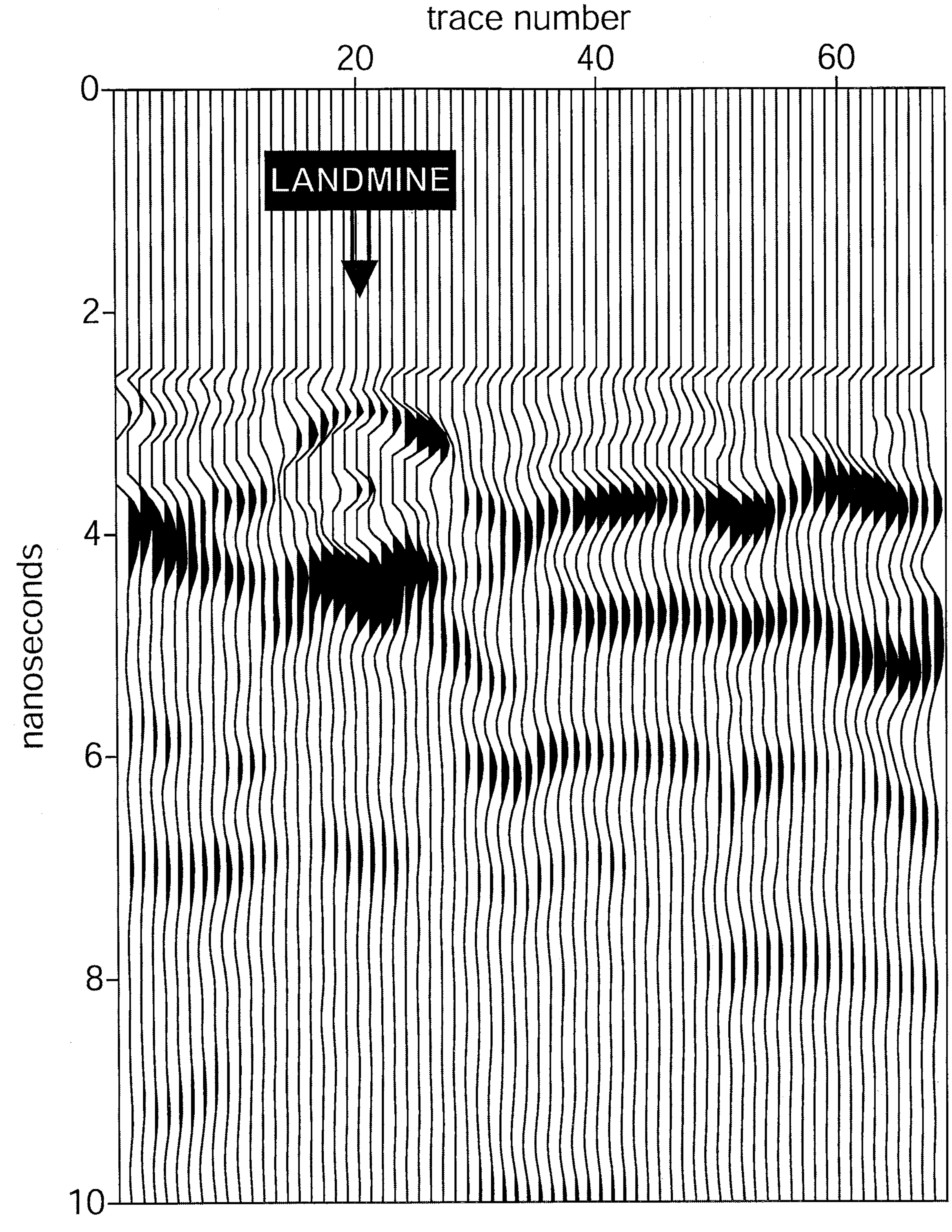

Figure 4.24 Wiggle trace plot of a silicon rubber simulant antitank landmine buried 11 cm below the ground surface in the Sevilleta sand soil at 29% volumetric soil water content, imaged 14 days after burial using a 900 MHz GPR system.

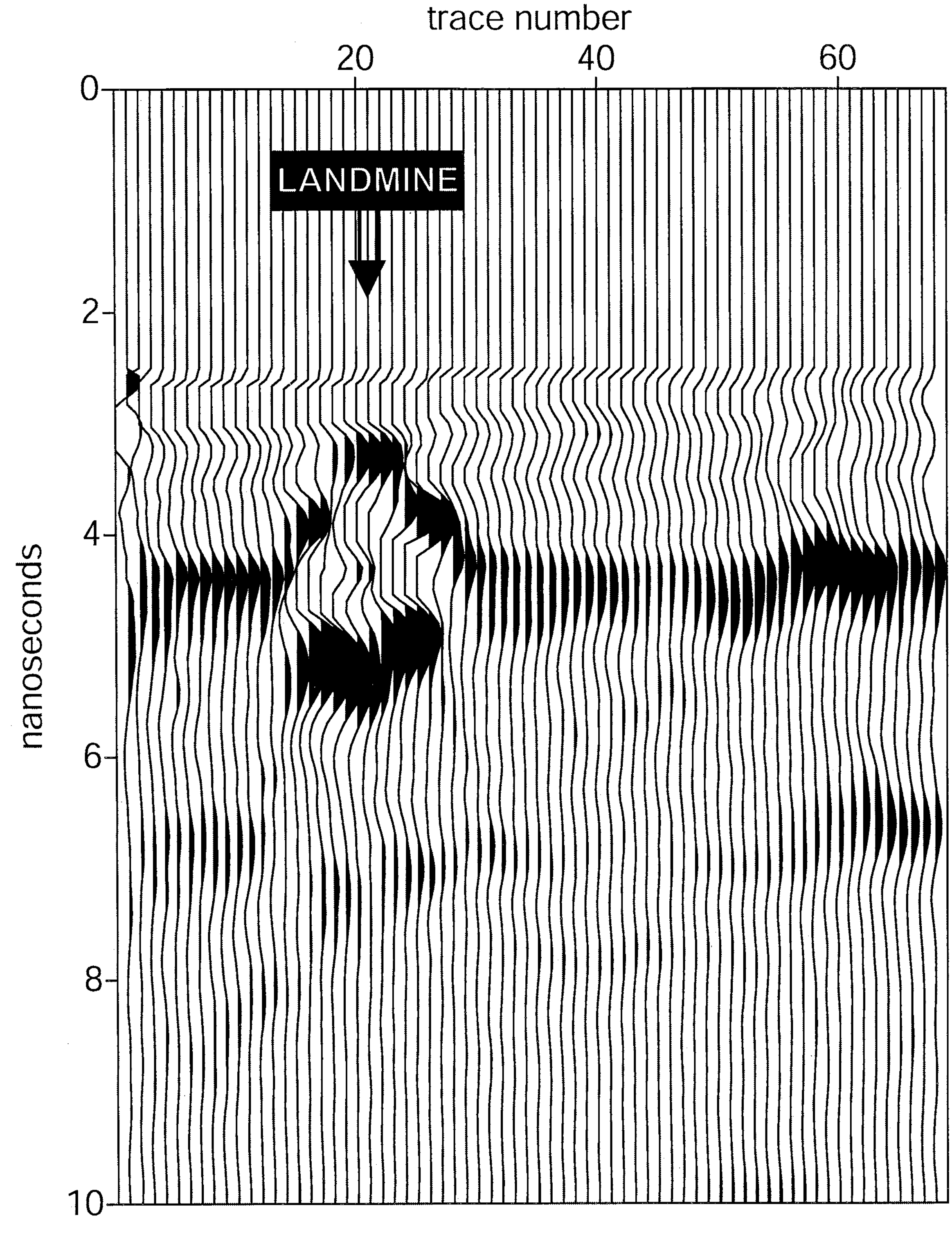

Figure 4.25 Wiggle trace plot of the Sevilleta silt loam soil site at 9% volumetric soil water content preceding landmine burial, imaged using a 900 MHz GPR system.

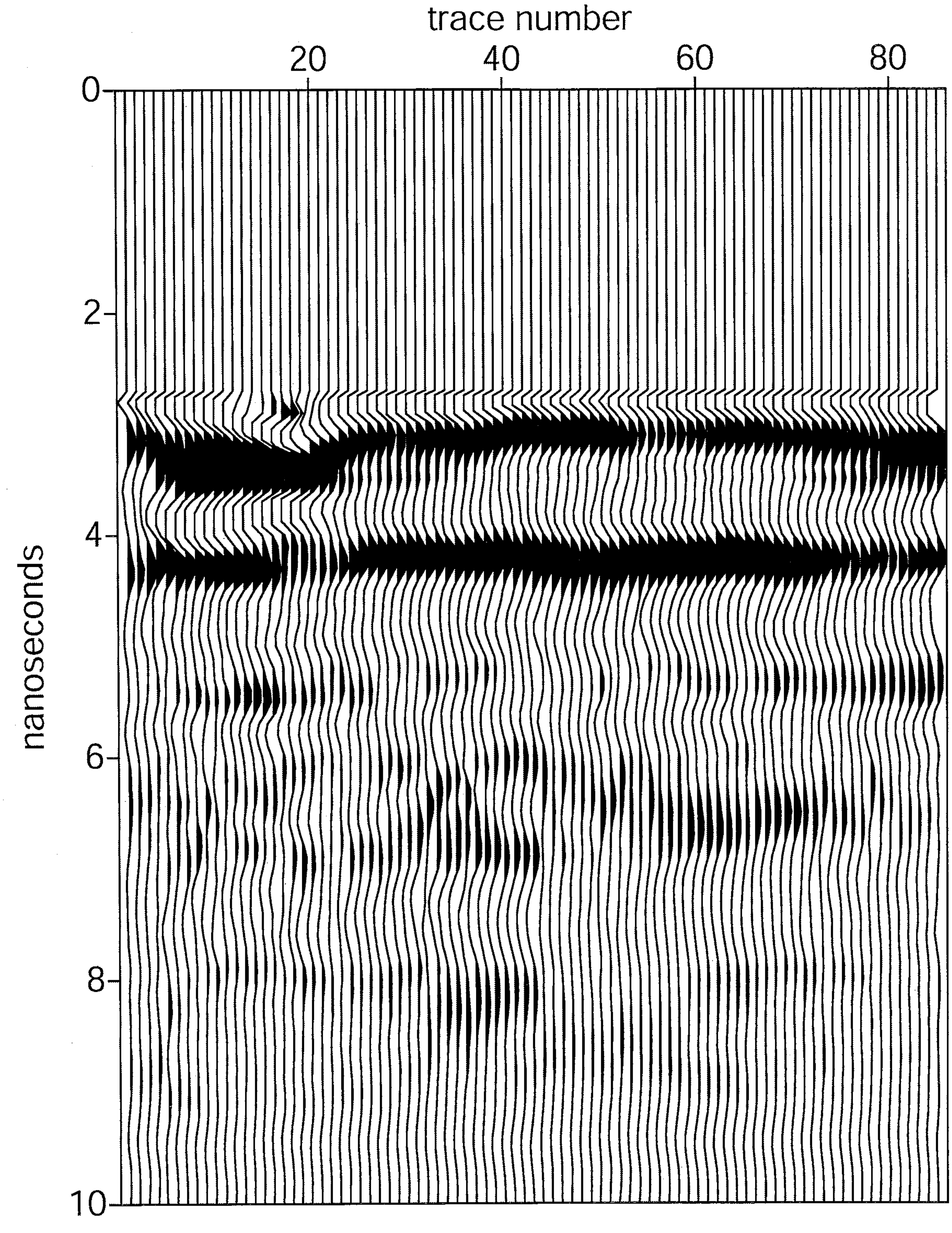

Figure 4.26 Wiggle trace plot of a silicon rubber simulant antitank landmine buried 11 cm below the ground surface in the Sevilleta silt loam soil at 9% volumetric soil water content, imaged one day after burial using a 900 MHz GPR system.

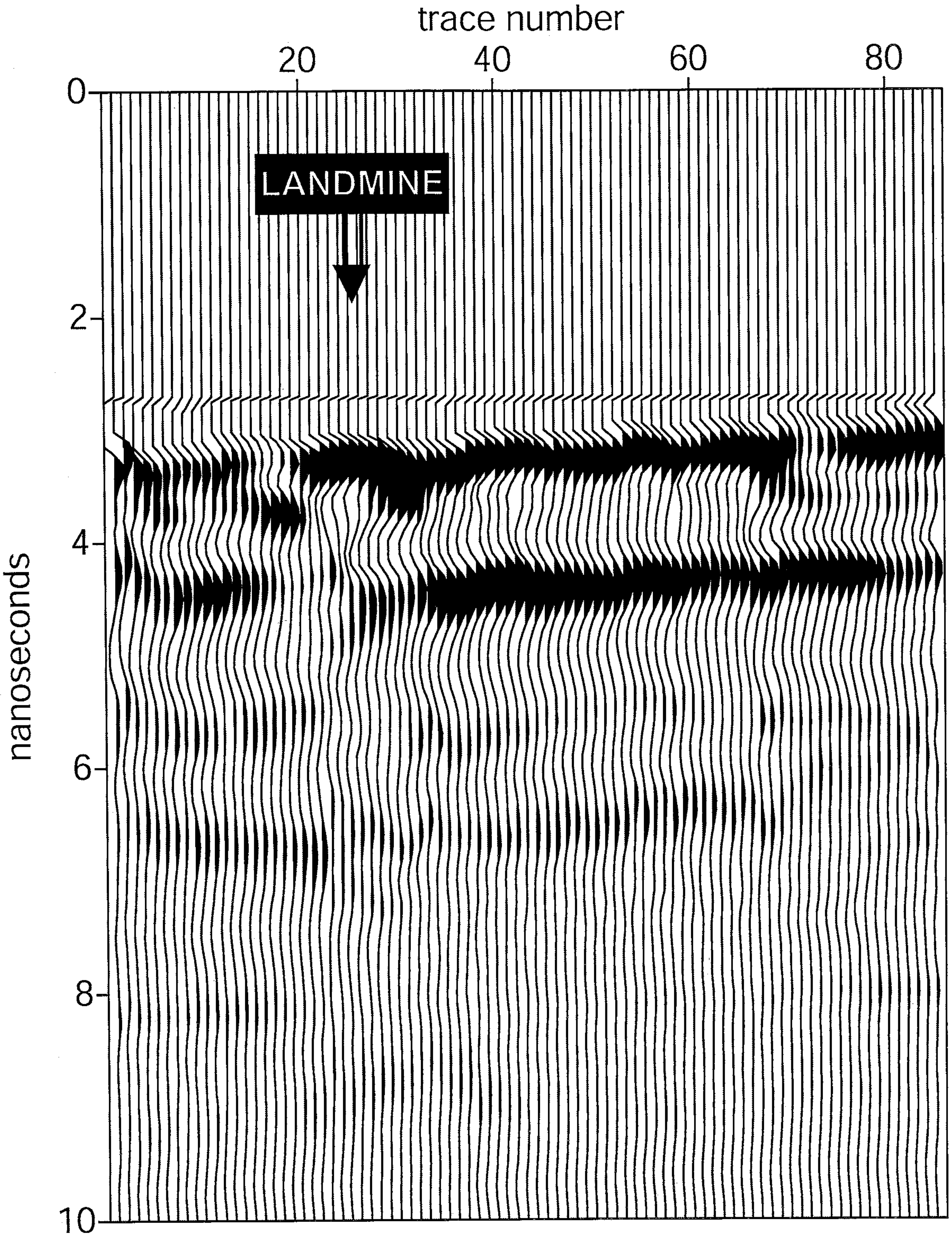

Figure 4.27 Wiggle trace plot of a silicon rubber simulant antitank landmine buried 11 cm below the ground surface in the Sevilleta silt loam soil at 26% volumetric soil water content, imaged 14 days after burial using a 900 MHz GPR system.

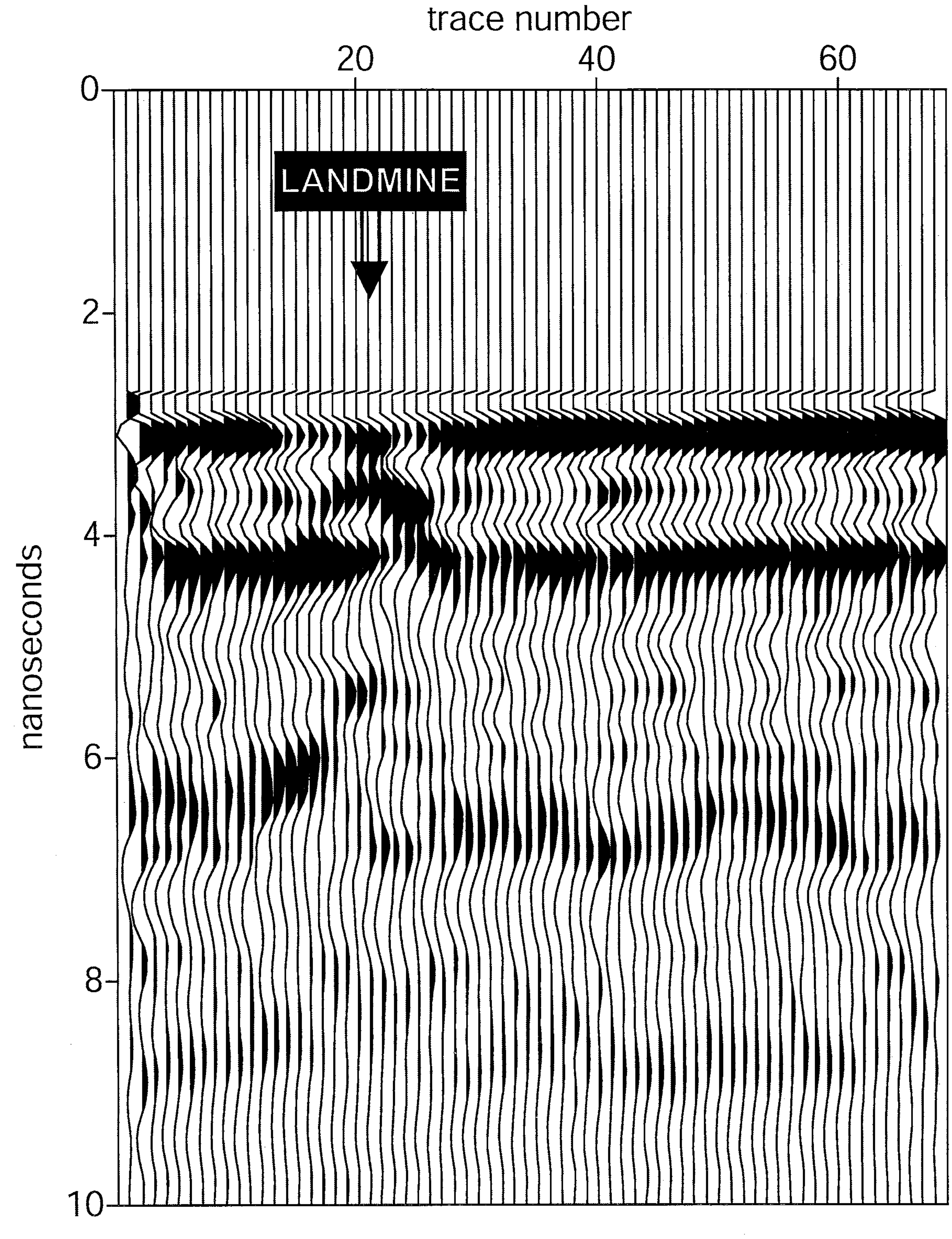

Figure 4.28 Wiggle trace plot of a silicon rubber simulant antitank landmine buried 11 cm below the ground surface in the Sevilleta silt loam soil at 38% volumetric soil water content, imaged 15 days after burial using a 900 MHz GPR system.

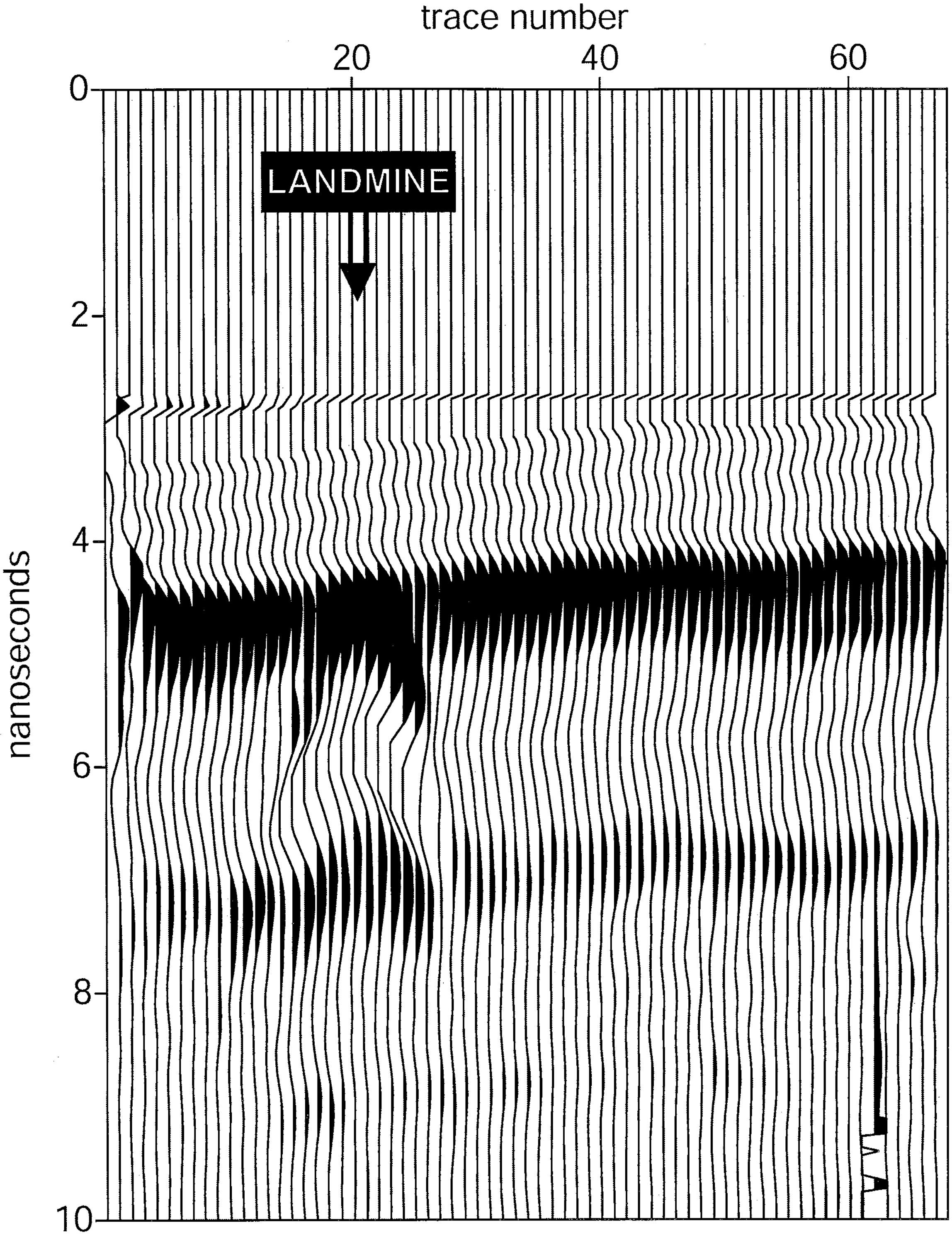

Figure 4.29 Wiggle trace plot of the Bosque clay soil site at 5% volumetric soil water content preceding landmine burial, imaged using a 900 MHz GPR system.

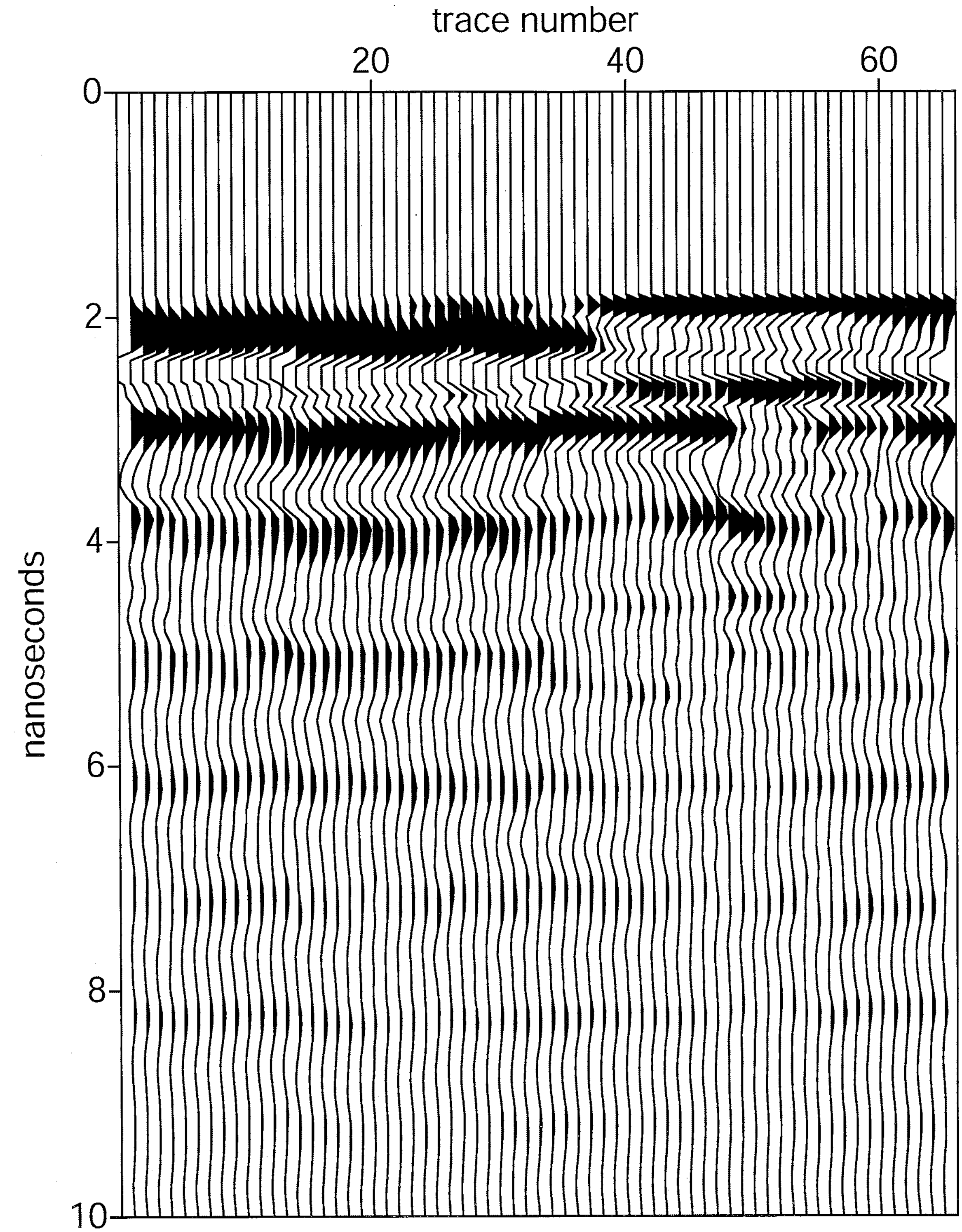

Figure 4.30 **Wiggle trace plot of a silicon rubber simulant antitank landmine buried 11 cm below the ground surface in the Bosque clay soil at 5% volumetric soil water content, imaged one day after burial using a 900 MHz GPR system.**

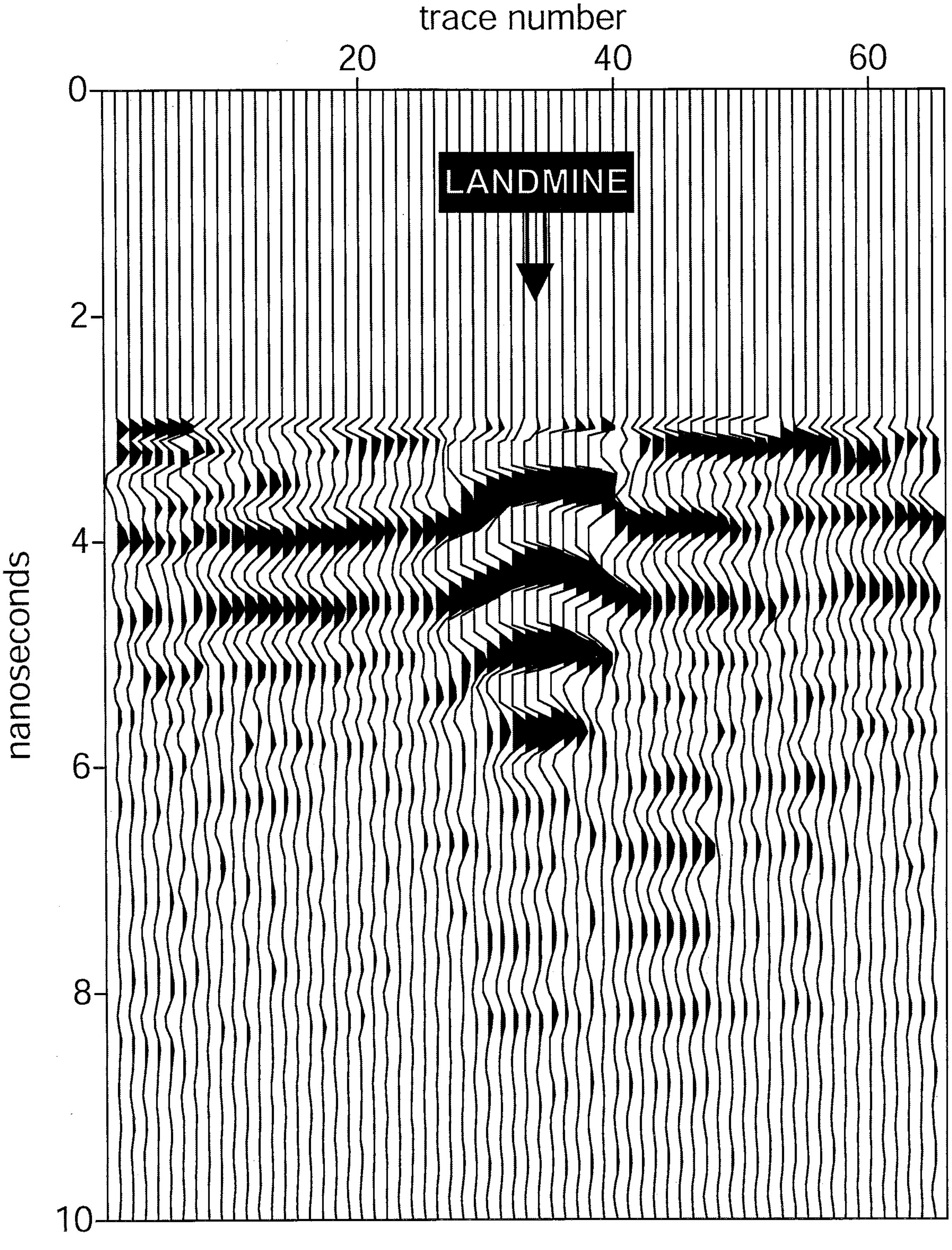

Figure 4.31 Wiggle trace plot of a silicon rubber simulant antitank landmine buried 11 cm below the ground surface in the Bosque clay soil at 14% volumetric soil water content, imaged about 2 weeks after burial using a 900 MHz GPR system.

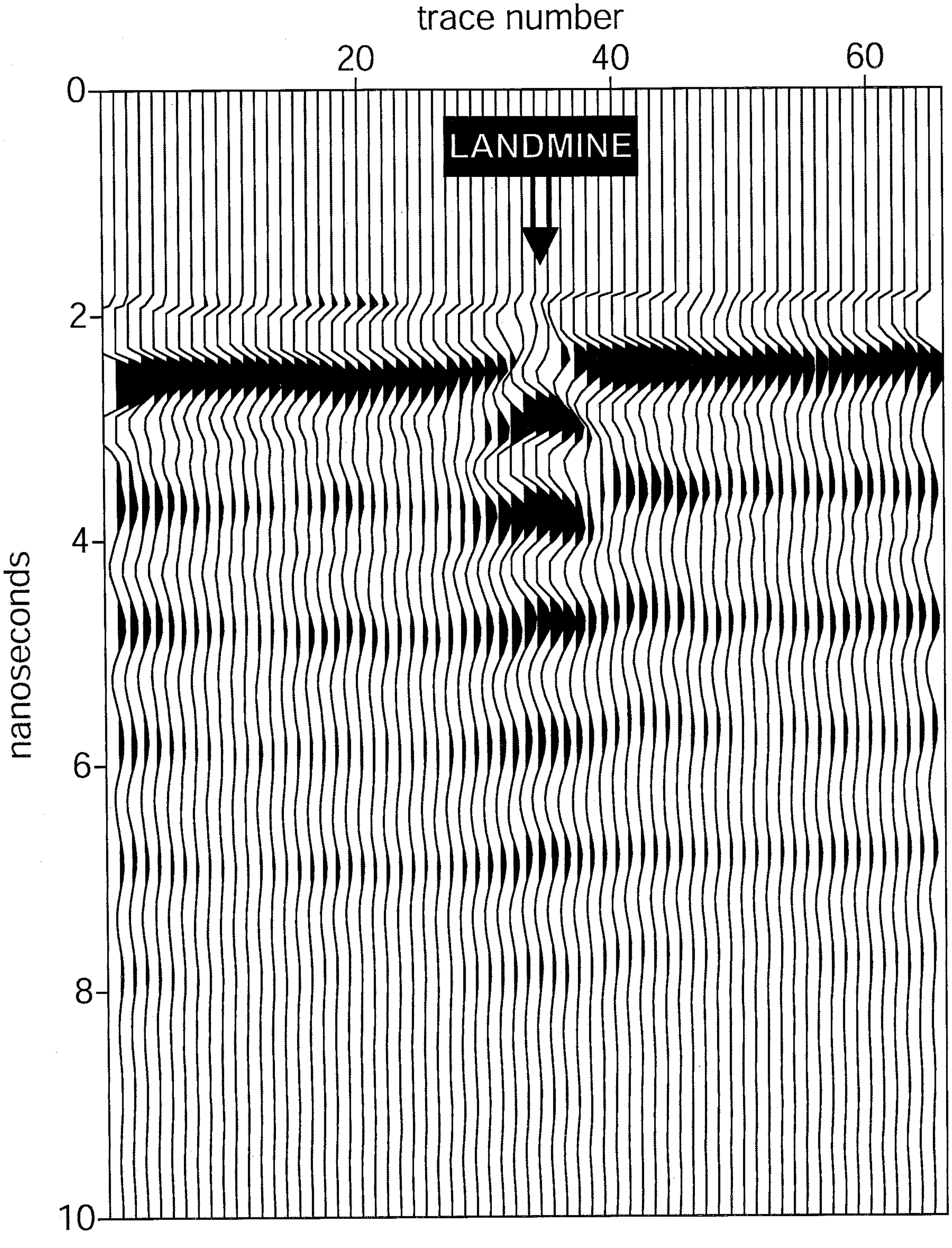

Figure 4.32 **Wiggle trace plot of a silicon rubber simulant antitank landmine buried 11 cm below the ground surface in the Bosque clay soil at 42% volumetric soil water content, imaged about 2 months after burial using a 900 MHz GPR system.**

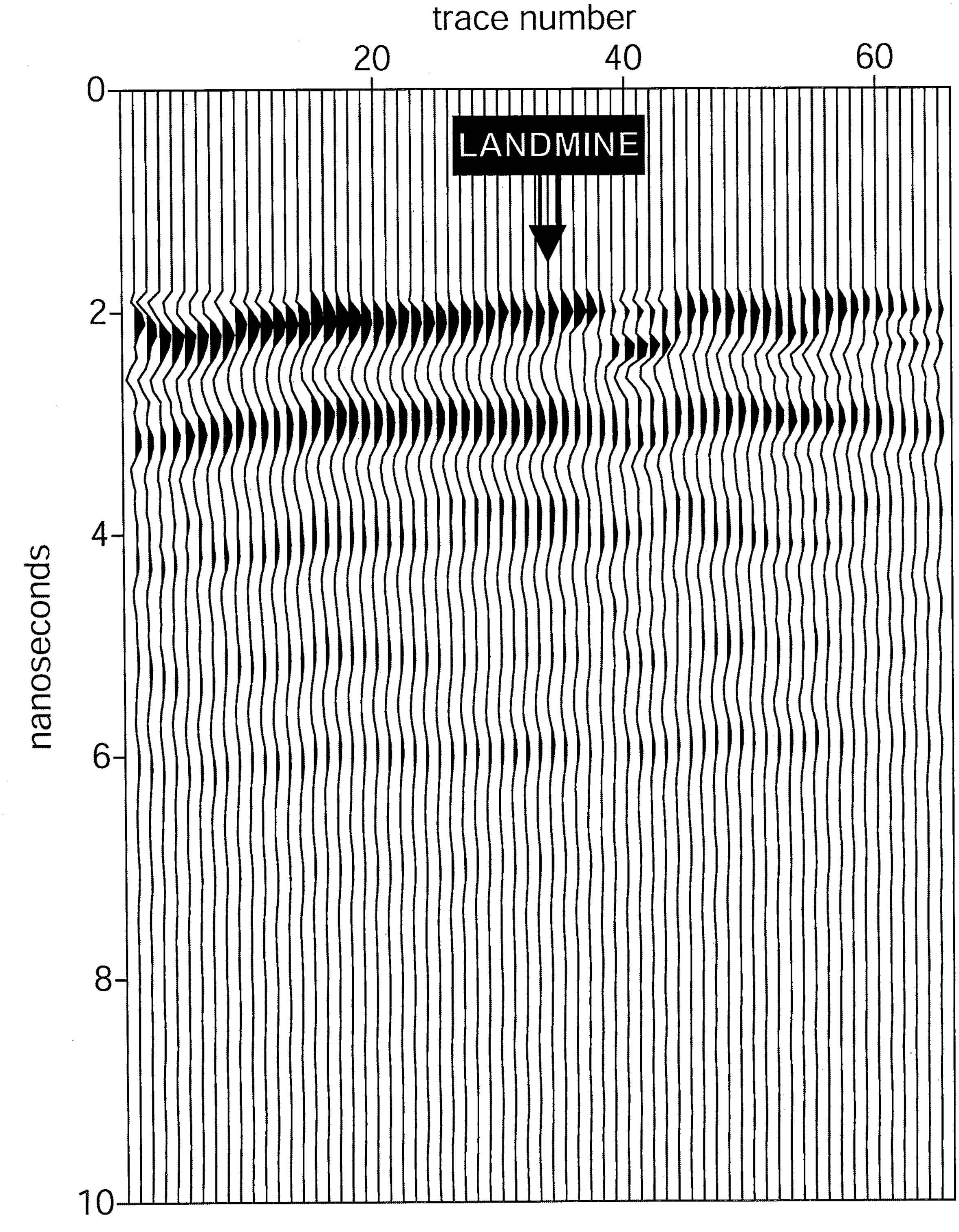

4.2.2 Results from the Saline Water Infiltration

In this section, the results from the saline water infiltration experiment are presented. The purpose of this experiment was to simulate a beach environment with buried landmines and then test the response of the GPR under these conditions.

Figure 4.33 is a GPR wiggle trace plot of the buried landmine prior to the infiltration of salt water. The landmine in this figure is seen in the center of the profile and denoted by the two black bands directly under the 45th trace. Figure 4.34 is a profile of the same site after 660 liters of salt water with a concentration of 31.8 g/L was applied to the site with the sprinkler system. The TDR system does not work in highly saline soils, thus exact soil water content was impossible to obtain. Therefore, it was estimated from our previous experiments at the same site. From our previous water application study, 660 liters of water was enough to saturate the soil above the landmine, so Figure 4.34 represents saturated conditions. The landmine is clearly undetectable with GPR instruments due to the increased soil electrical conductivity. Figure 4.35 shows the same area after an additional 660 liters of salt water with a concentration of 34.1 g/L was applied to the site. The landmine is still undetectable with the GPR system. Figure 4.36 is a profile that was collected after the site had dried for 17 days. During this time interval, approximately 2.9 mm of water was applied to the site in the form of rainfall.

These figures demonstrate that landmine detection is impossible in wet saline sandy soils, but under dry conditions it is possible. This phenomenon is due to the increase in the loss term (ε'') of the complex dielectric constant as the electrical conductivity of the soil is increased through application of saline water.

Figure 4.33 Saline water infiltration site prior to infiltration, at 2.6% volumetric soil water content.

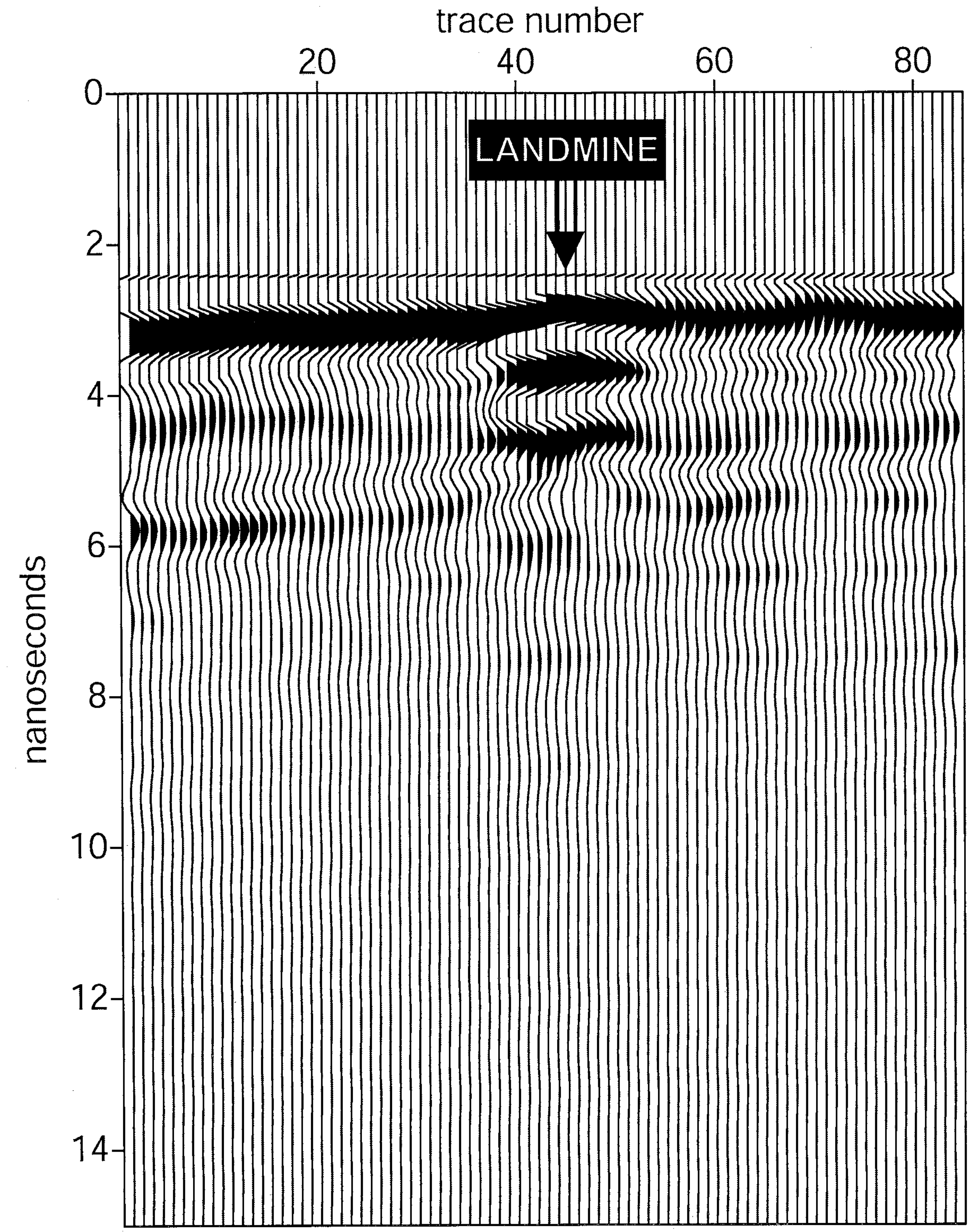

Figure 4.34 Saline water infiltration site after addition of 7.4 cm of 31.8 g/L saline water.

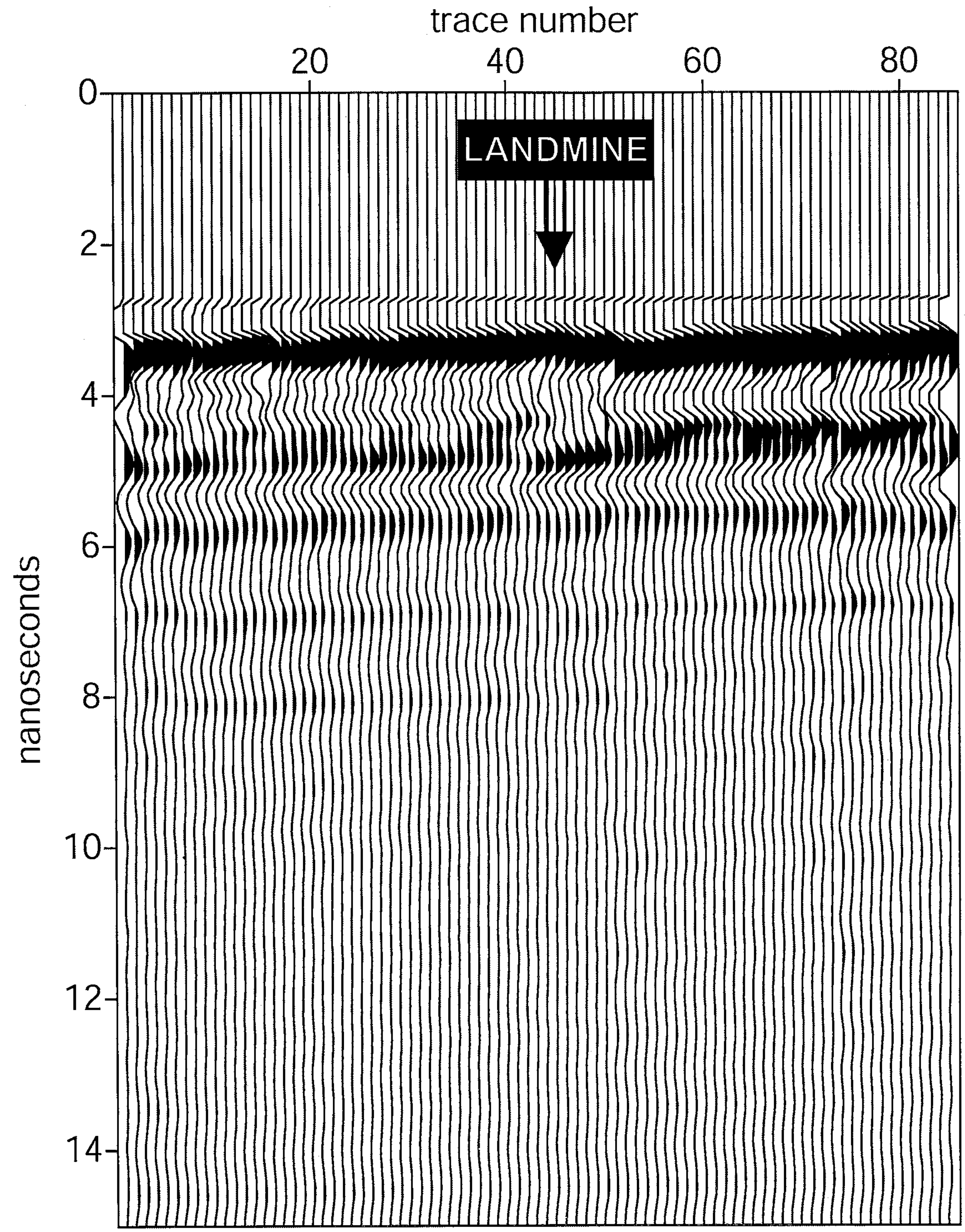

Figure 4.35 **Saline water infiltration site after addition of 14.8 cm of 34.1 g/L saline water.**

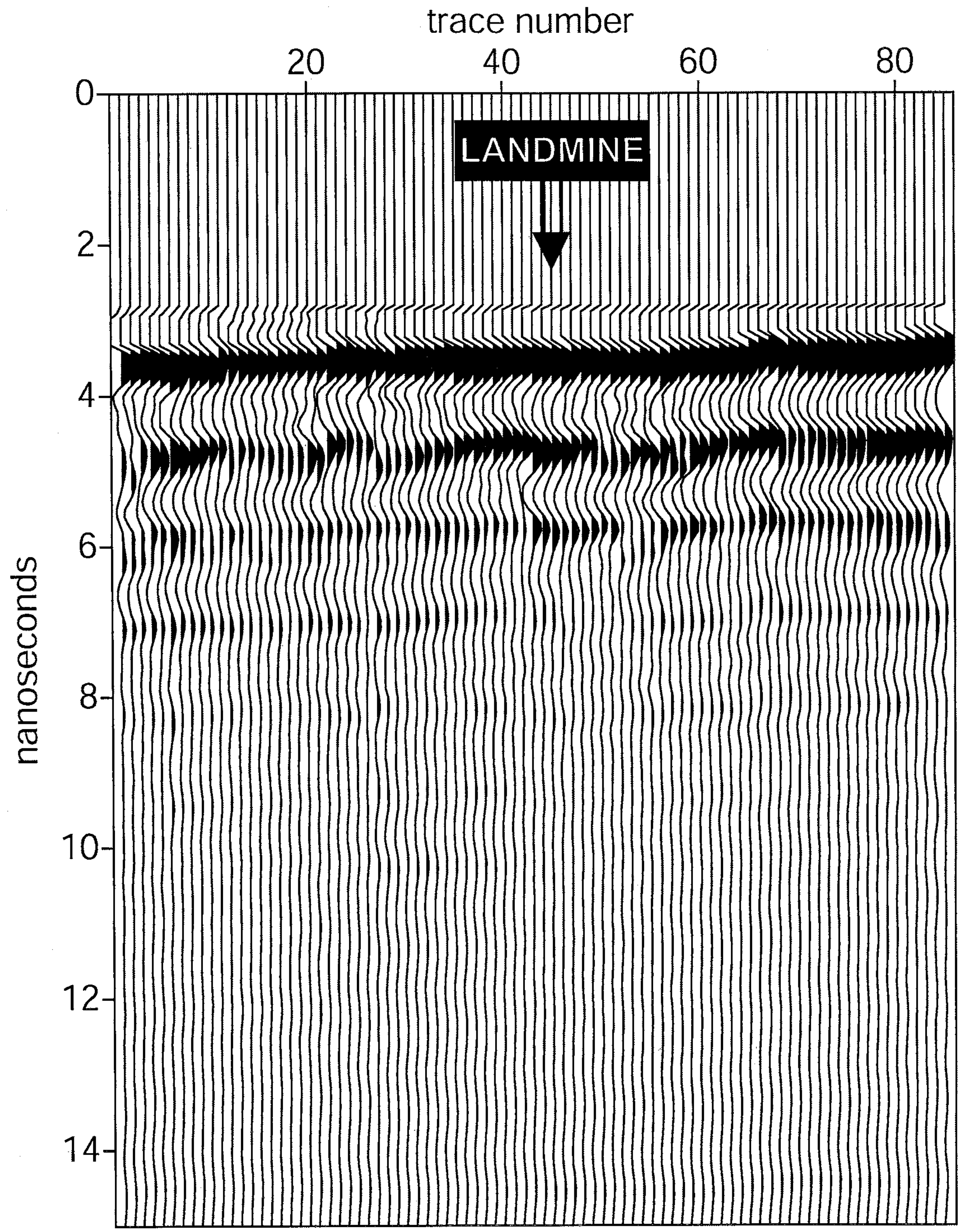

Figure 4.36 **Saline water infiltration site after 17 days of drying and 2.9 mm of rain.**

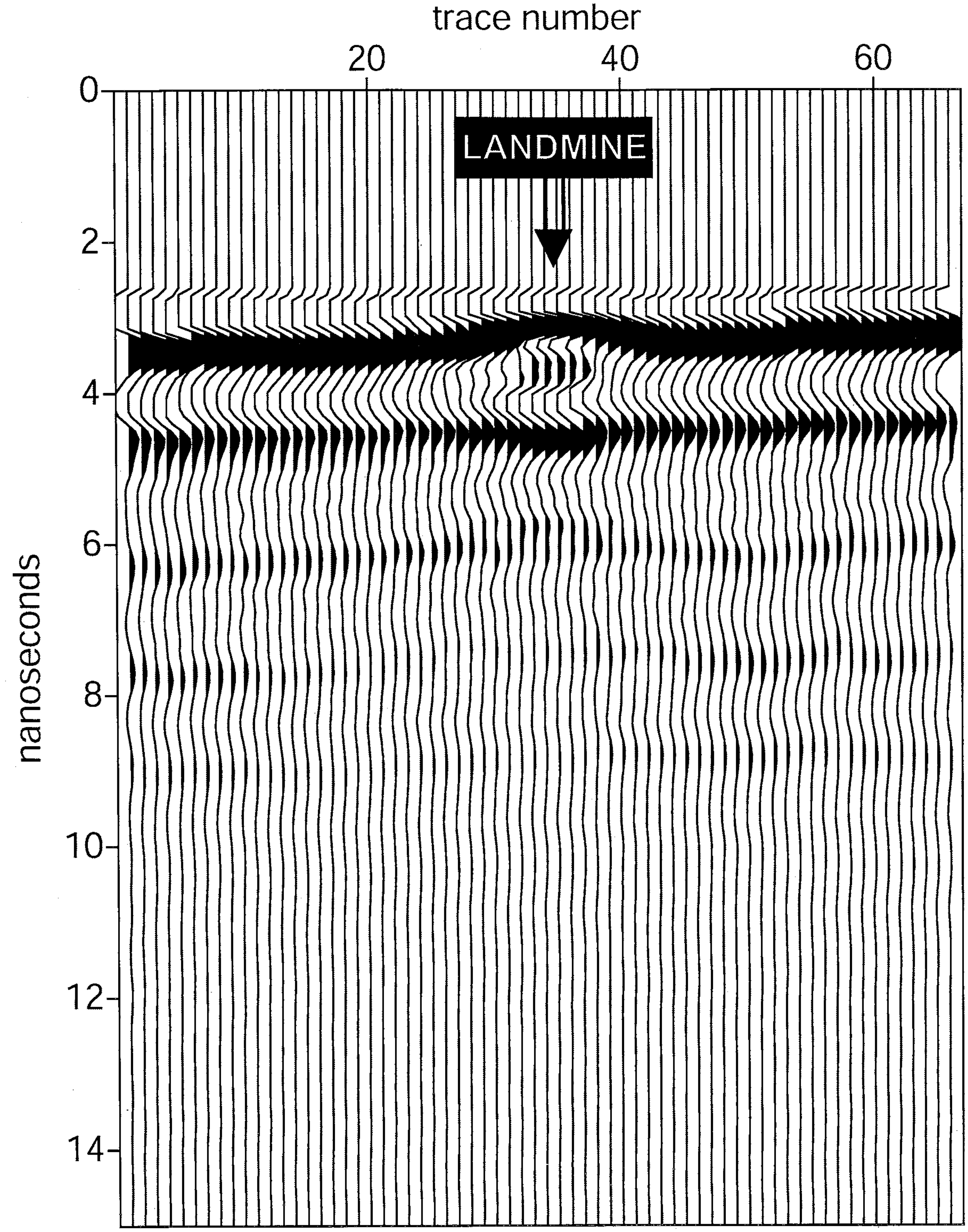

4.2.3 Results from Yuma, AZ Test Sites

In this section the results from the Yuma Proving Grounds landmine test range are presented. The first eight figures (Figure 4.37 through Figure 4.44) show GPR images of buried antitank landmines from the Handheld test range, and the last four (Figure 4.45 through Figure 4.48) show buried antitank landmines from the Vehicle test range under both dry and saturated soil conditions. Figure 4.37 is a wiggle trace plot of a VS – 1.6 antitank landmine buried 7.62 cm deep in dry loamy sand soil. The VS – 1.6 is a low metal antitank landmine and contains a high explosive main charge with a surrogate RTV-3110 silicon rubber booster. The detonator shaft is the only metallic component of the landmine. In this figure a small reflection from the top of the landmine can be seen at the 34th trace. The contrast in the dielectric constant between the landmine and the surrounding soil is not large enough to produce a significant reflection, so detection is difficult. Figure 4.38 is an image of the same landmine after the soil water content was raised to 26%. A stronger reflection is produced from the landmine and detection is enhanced.

Figure 4.39 is an image of a VS – 2.2 nonmetallic antitank landmine buried 7.62 cm deep in dry loamy sand. The VS – 2.2 is very similar to the VS – 1.6 in dimensions and composition, and only differing in its thickness. The radar image of this landmine is similar, showing a small reflection under dry field conditions (See Figure 4.39). When the soil above the landmine is saturated, a stronger reflection is produced from the surface of the landmine and the hyperbolic limbs can be see extending down (See Figure 4.40).

Figure 4.41 is an image of a TM62M metallic landmine buried in dry loamy sand soil. This figure shows a very strong reflection from the landmine when the soil is dry, since metallic landmines should produce perfect reflection because their reflection coefficients are equal to unity. Figure 4.42 is a radar image of the same landmine after the soil water content was raised to 26% above the landmine. The landmine in this figure would most likely not be detectable with the GPR at greater soil water contents. This figure shows how attenuation can increase due to elevated soil water conditions. Metallic landmines have dielectric constants that are very large, approaching infinity, so the contrast between these types of landmines and the soil is also very large which should always produce significant reflections as stated before. However, as seen in this example applying water in certain situations will not enhance detection, rather it produces the opposite effect.

Figure 4.43 is a radar image of a TM62P3 antitank landmine buried in dry loamy sand soil. The TM62P3 is identical to the TM62M in explosive composition and dimensions, however it is nonmetallic. The reflection from it, seen in Figure 4.43, is weak indicating a low contrast between it and the surrounding soil. After applying water to the site with the sprinkler system, a slightly stronger reflection is produced from its surface (See Figure 4.44). The reflection is not as strong as anticipated and may be the result of increased attenuation or not enough contrast between the soil and landmine dielectric constants.

Figure 4.45 is a GPR profile of a M19 nonmetallic antitank landmine buried in sandy loam soil. Under dry field conditions a clear hyperbolic reflection is produced for the surface of the landmine (See Figure 4.45). However, when the soil water content is increased to 22% above the landmine the detection is not enhanced. Figure 4.47 is an image of a M15 metallic antitank landmine buried in sandy loam soil. The metallic landmine in this figure produces a very clear reflection when the soil is dry. This is due the large dielectric contrast between the mine and the soil. After soil water content was increased to 23% above the mine, the image quality decreases (See Figure 4.48). A reflection from the landmine is still seen but is not as strong as under dry soil conditions. This is the result of increased attenuation caused by the elevated soil water conditions.

Figure 4.37 GPR profile of a VS – 1.6 nonmetallic antitank landmine buried 7.62 cm deep in loamy sand soil at 5% volumetric soil water content.

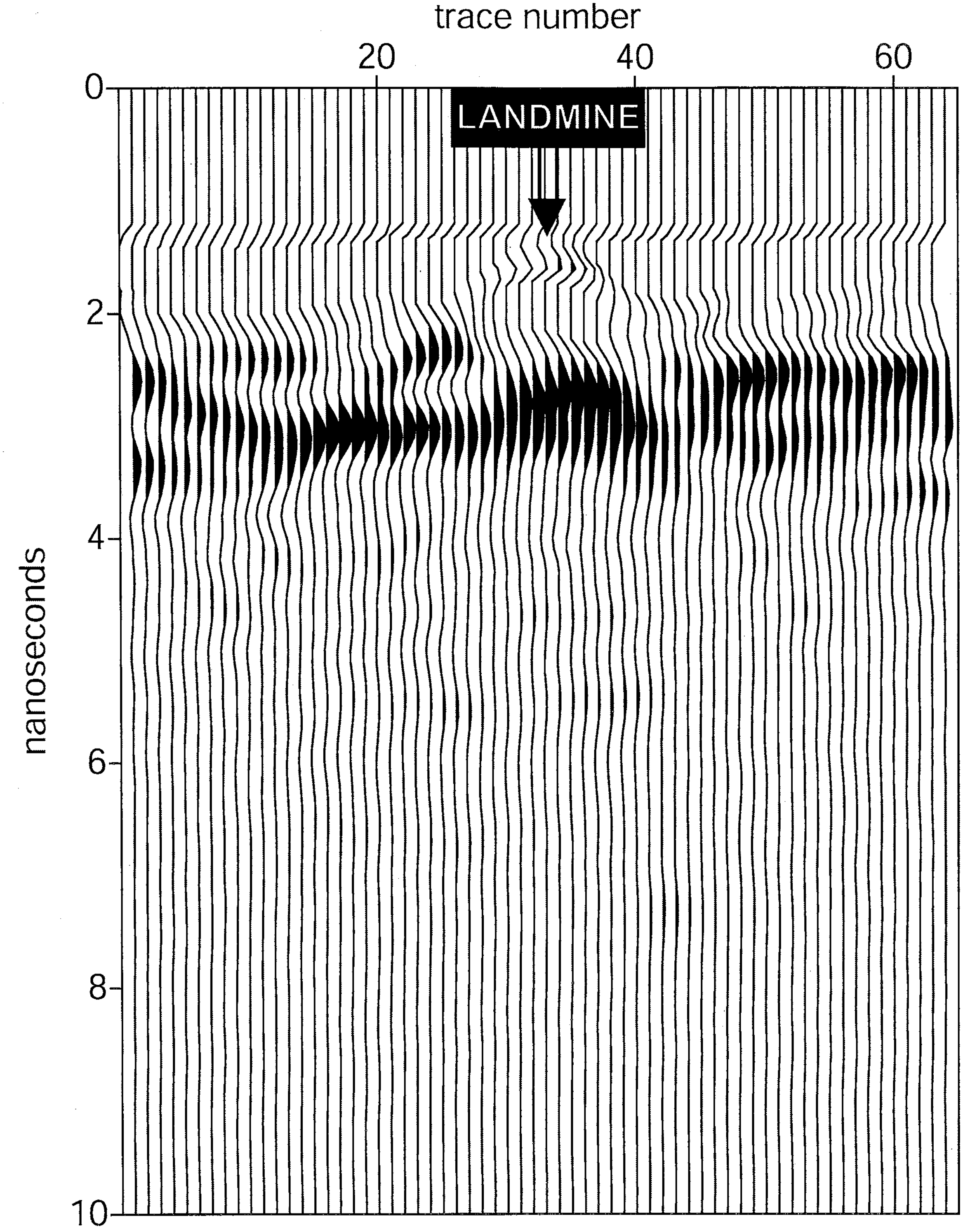

Figure 4.38 **GPR profile of a VS – 1.6 nonmetallic antitank landmine buried 7.62 cm deep in loamy sand soil at 26% volumetric soil water content.**

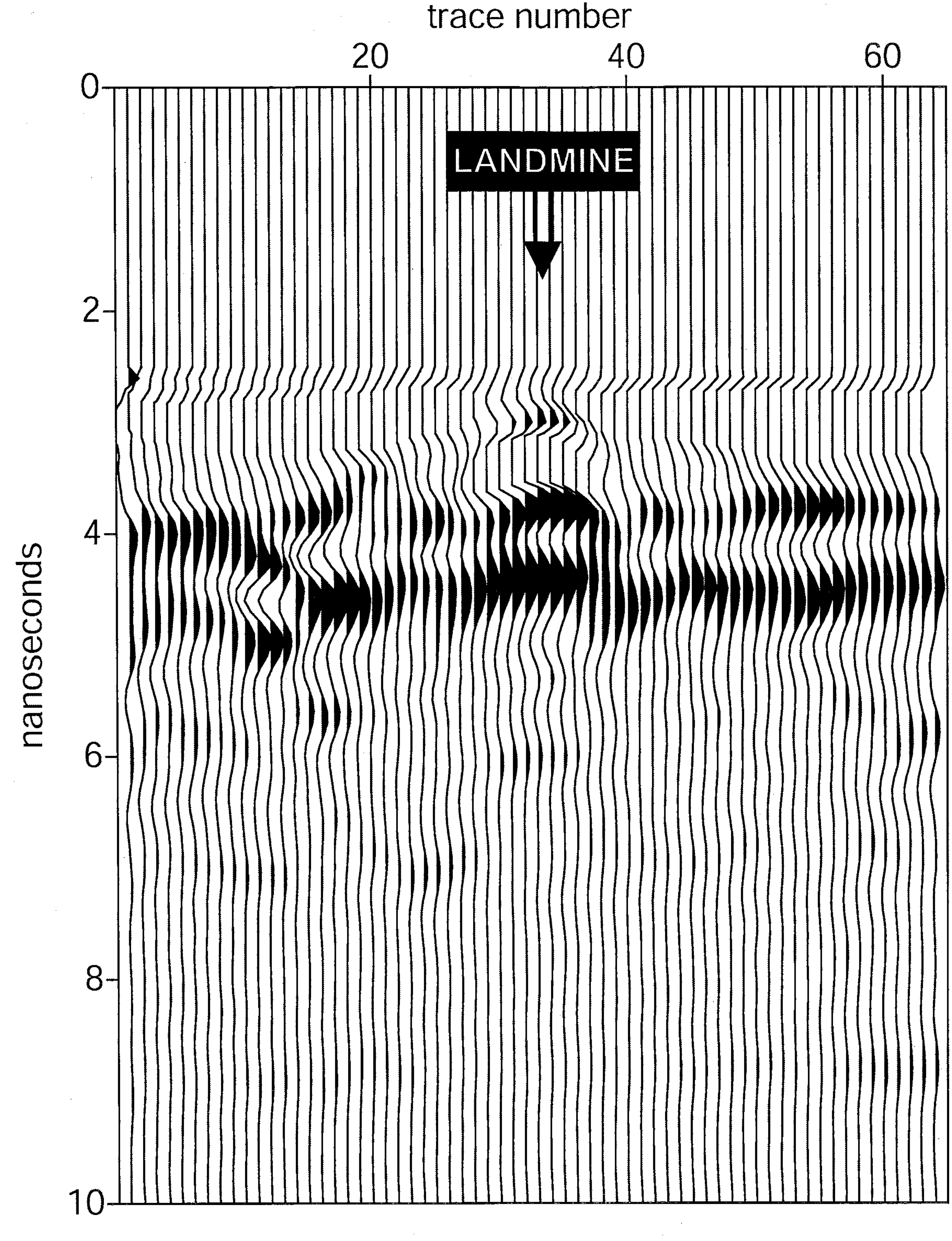

Figure 4.39 GPR profile of a VS – 2.2 nonmetallic antitank landmine buried 7.62 cm deep in loamy sand soil at 5% volumetric soil water content.

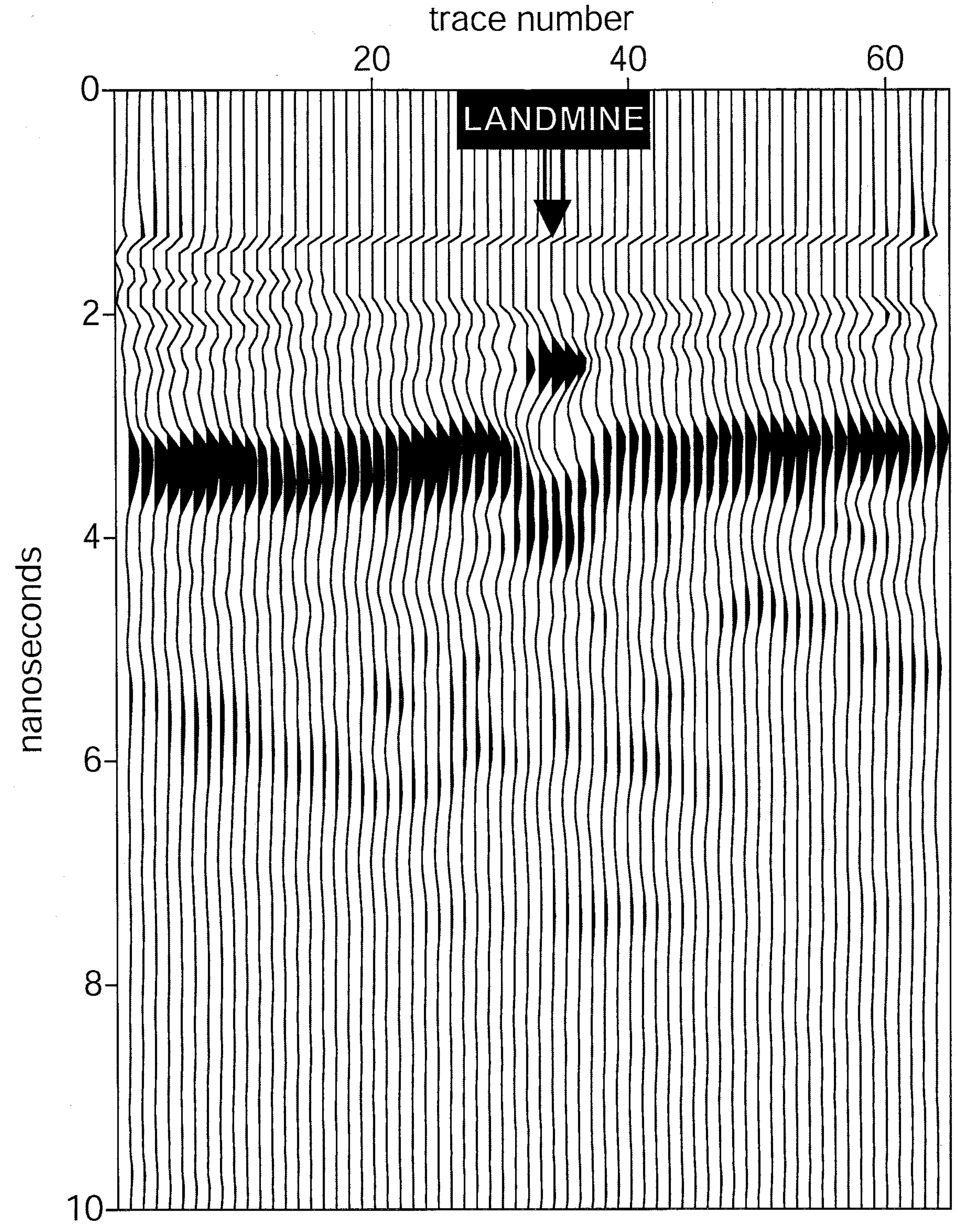

Figure 4.40 GPR profile of a VS – 2.2 nonmetallic antitank landmine buried 7.62 cm deep in loamy sand soil at 26% volumetric soil water content.

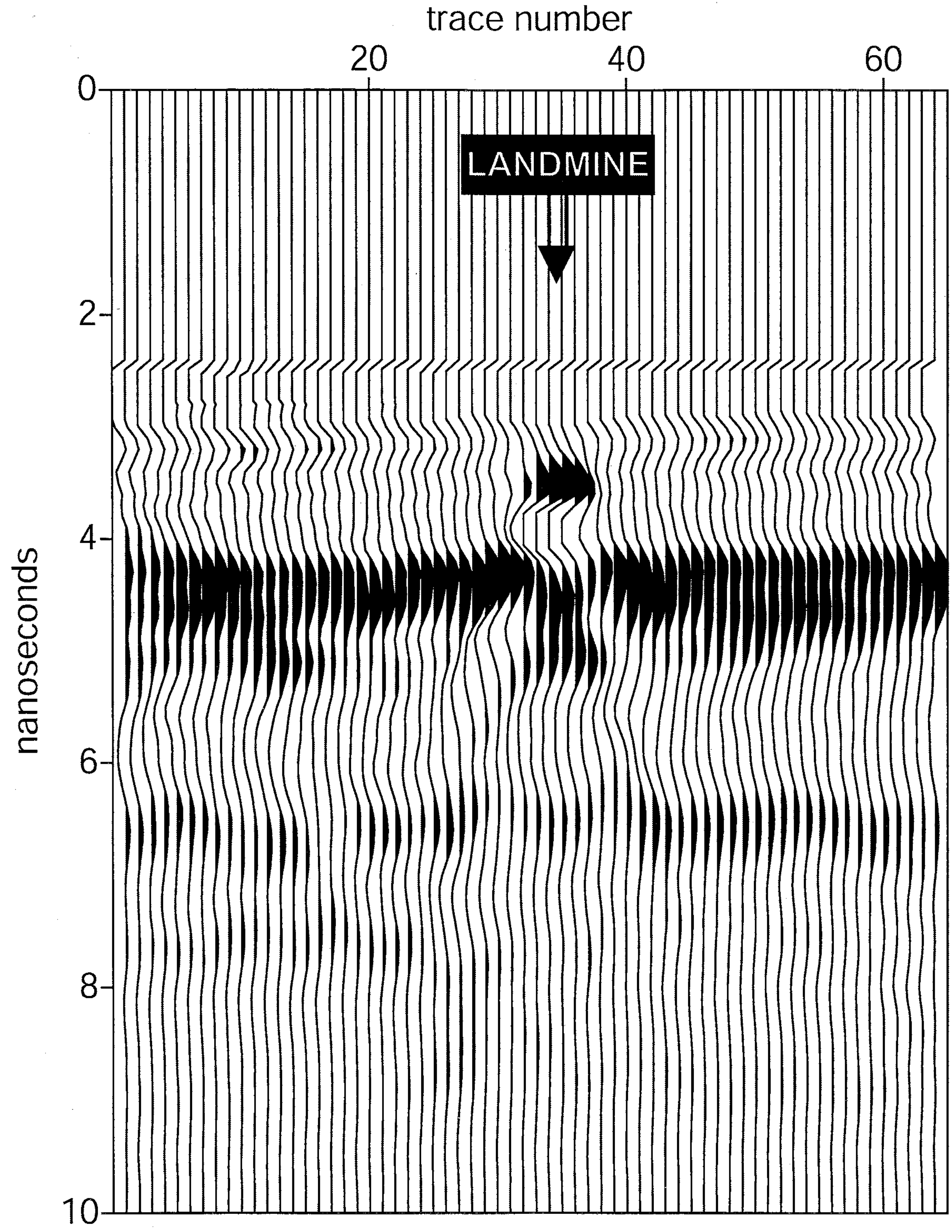

Figure 4.41 GPR profile of a TM62M metallic antitank landmine buried 12.7 cm deep in loamy sand soil at 5% volumetric soil water content.

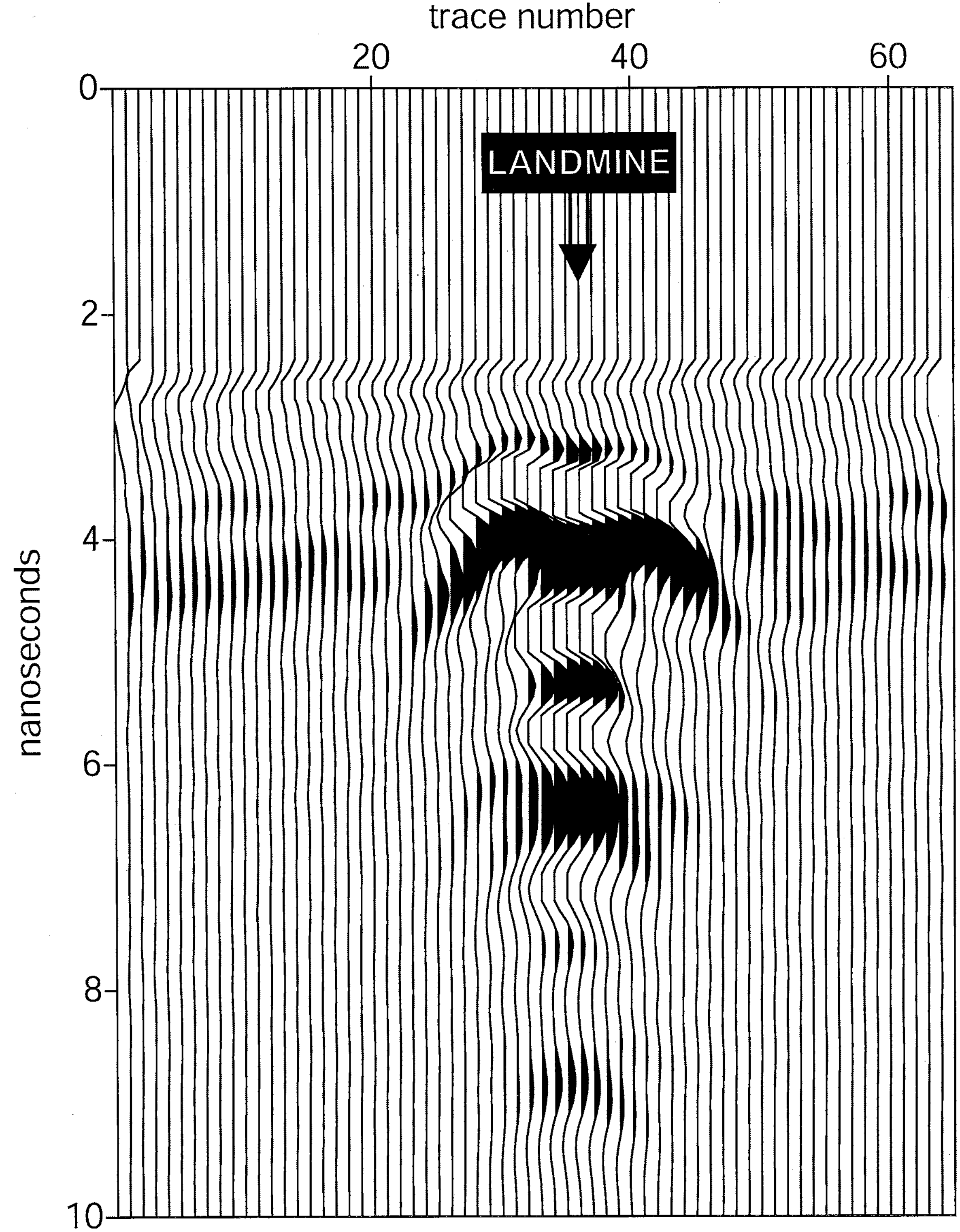

Figure 4.42 GPR profile of a TM62M metallic antitank landmine buried 12.7 cm deep in loamy sand soil at 26% volumetric soil water content.

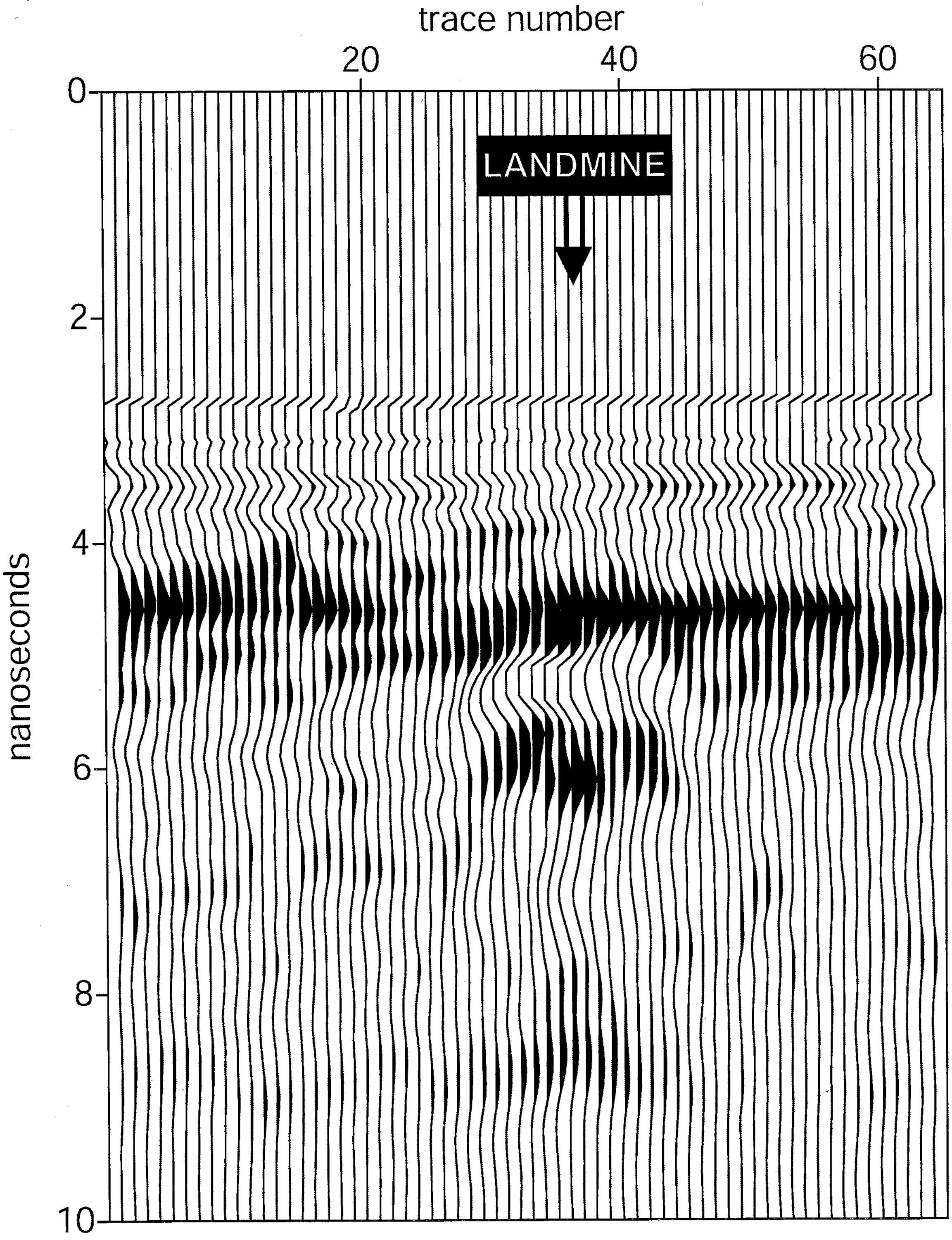

Figure 4.43 GPR profile of a TM62P3 nonmetallic antitank landmine buried 7.62 cm deep in loamy sand soil at 5% volumetric soil water content.

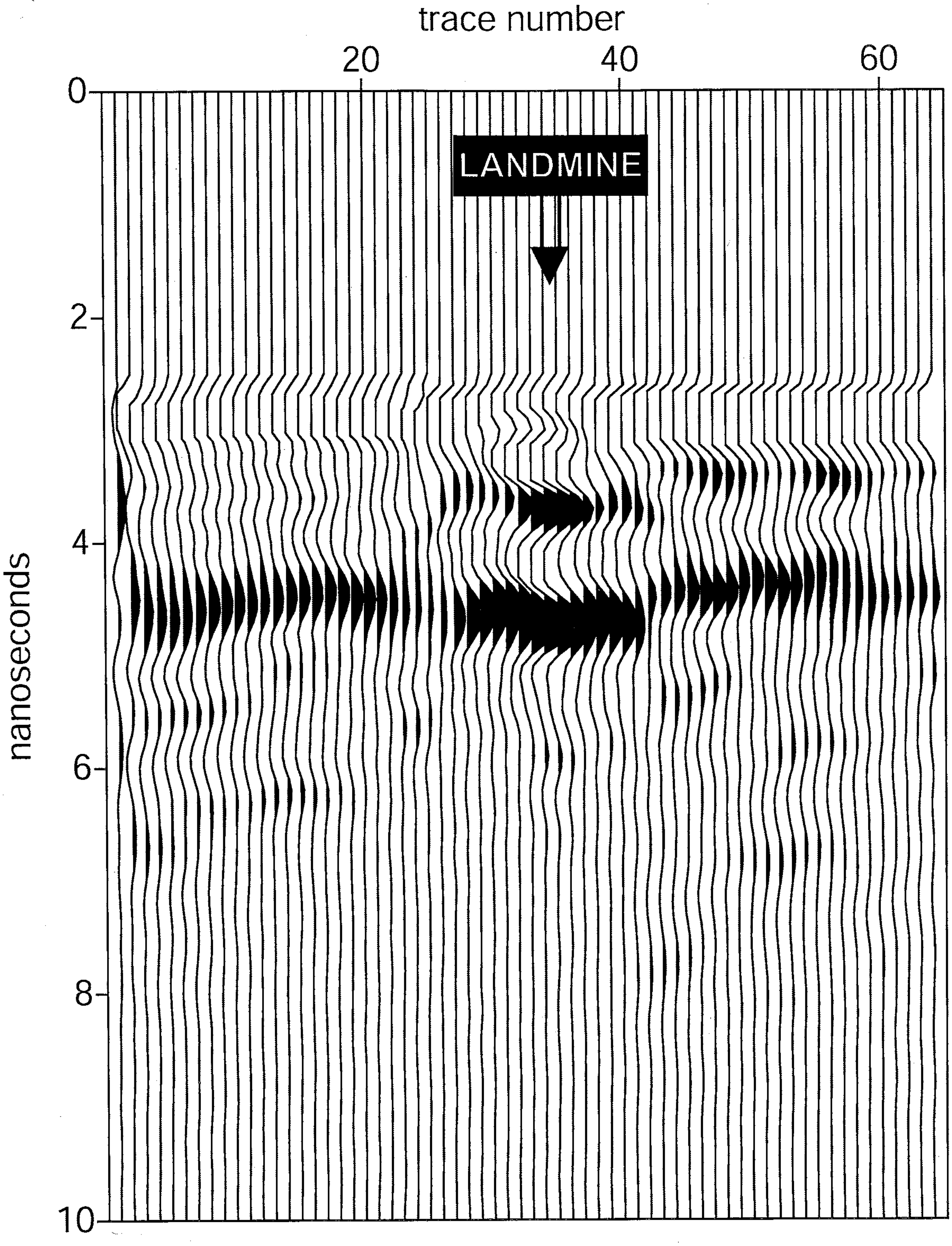

Figure 4.44 GPR profile of a TM62P3 nonmetallic antitank landmine buried 7.62 cm deep in loamy sand soil at 26% volumetric soil water content.

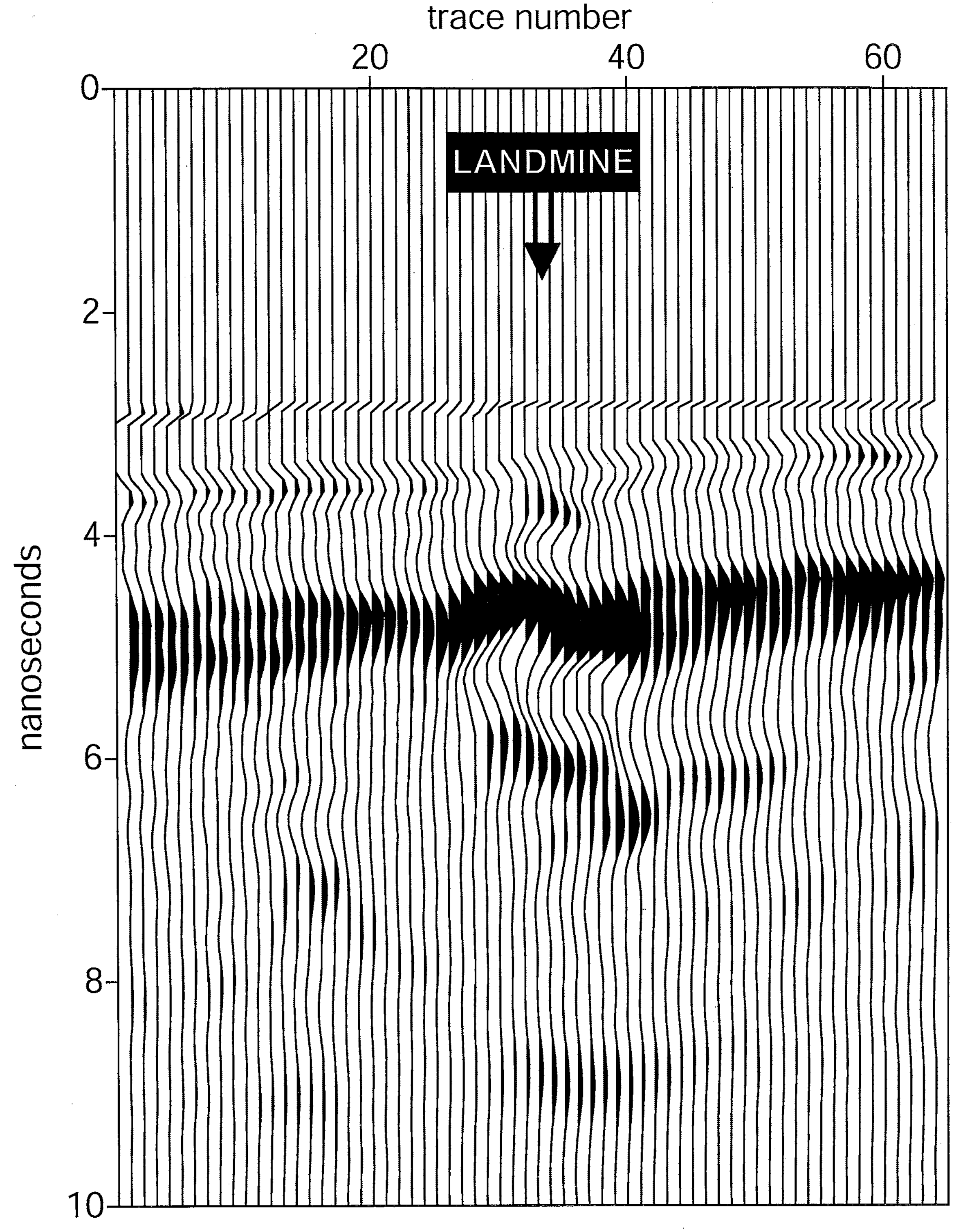

Figure 4.45 GPR profile of a M19 nonmetallic antitank landmine buried 7.62 cm deep in sandy loam soil at 6% volumetric soil water content.

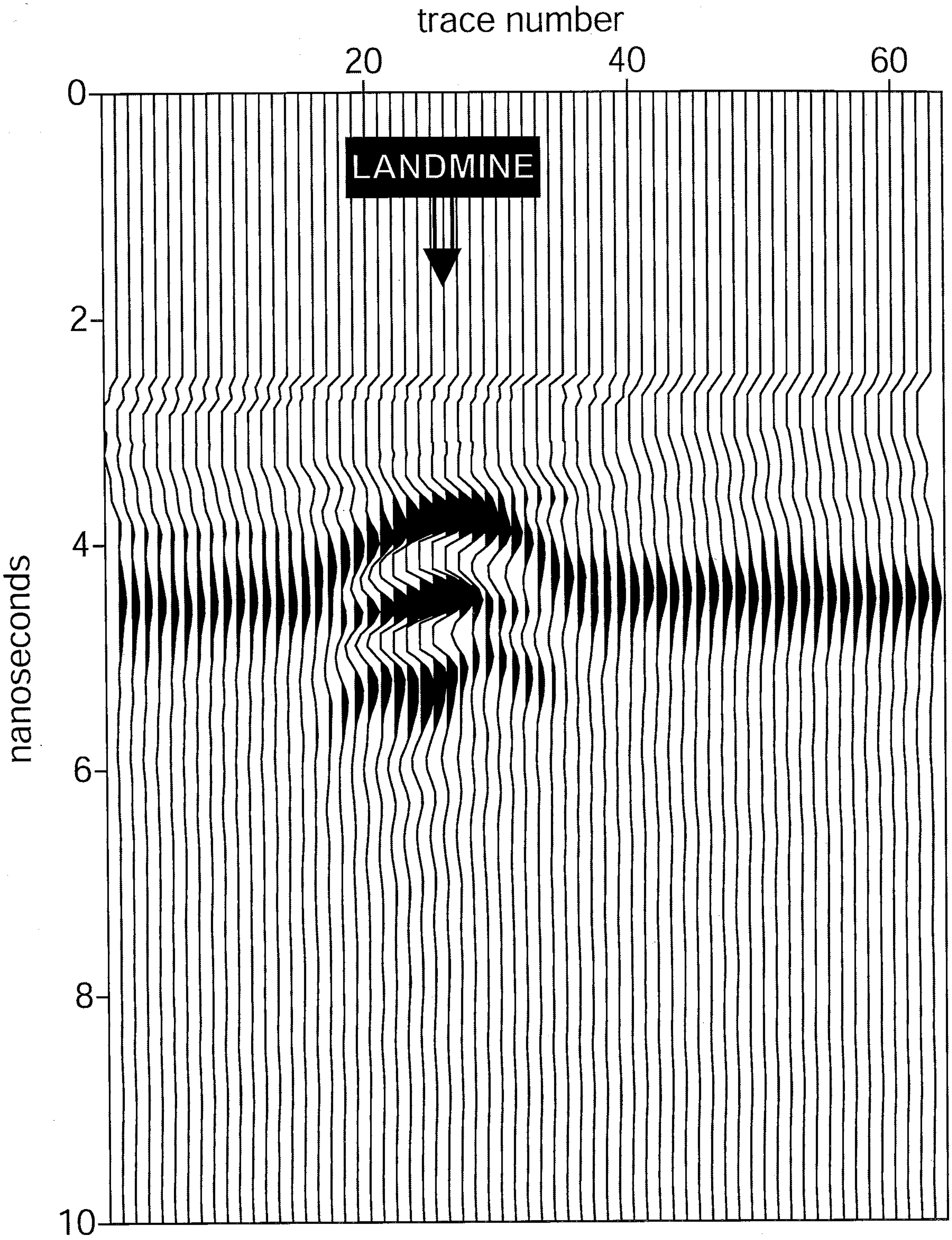

Figure 4.46 GPR profile of a M19 nonmetallic antitank landmine buried 7.62 cm deep in sandy loam soil at 22% volumetric soil water content.

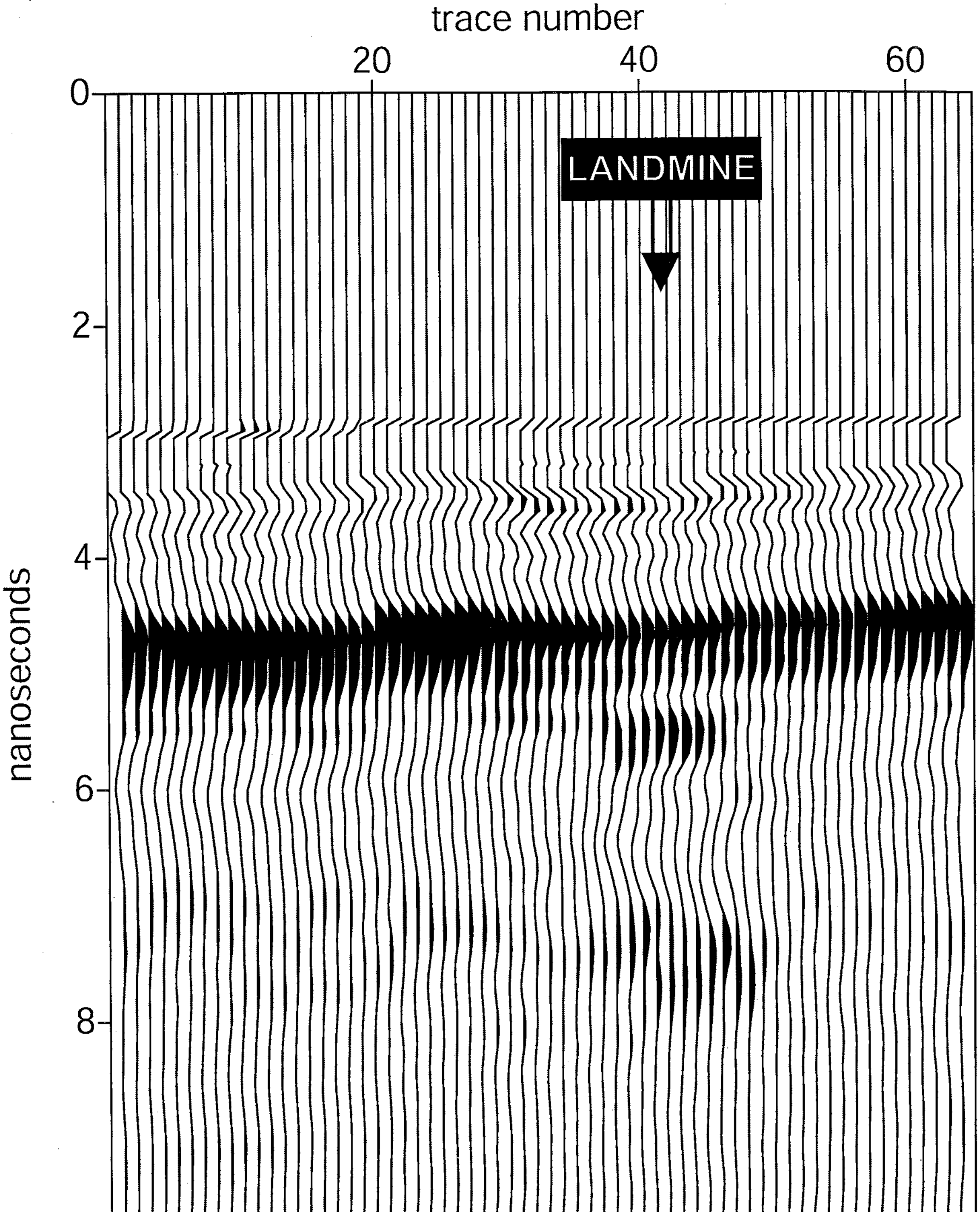

Figure 4.47 **GPR profile of a M15 metallic antitank landmine buried 12.7 cm deep in sandy loam soil at 6% volumetric soil water content.**

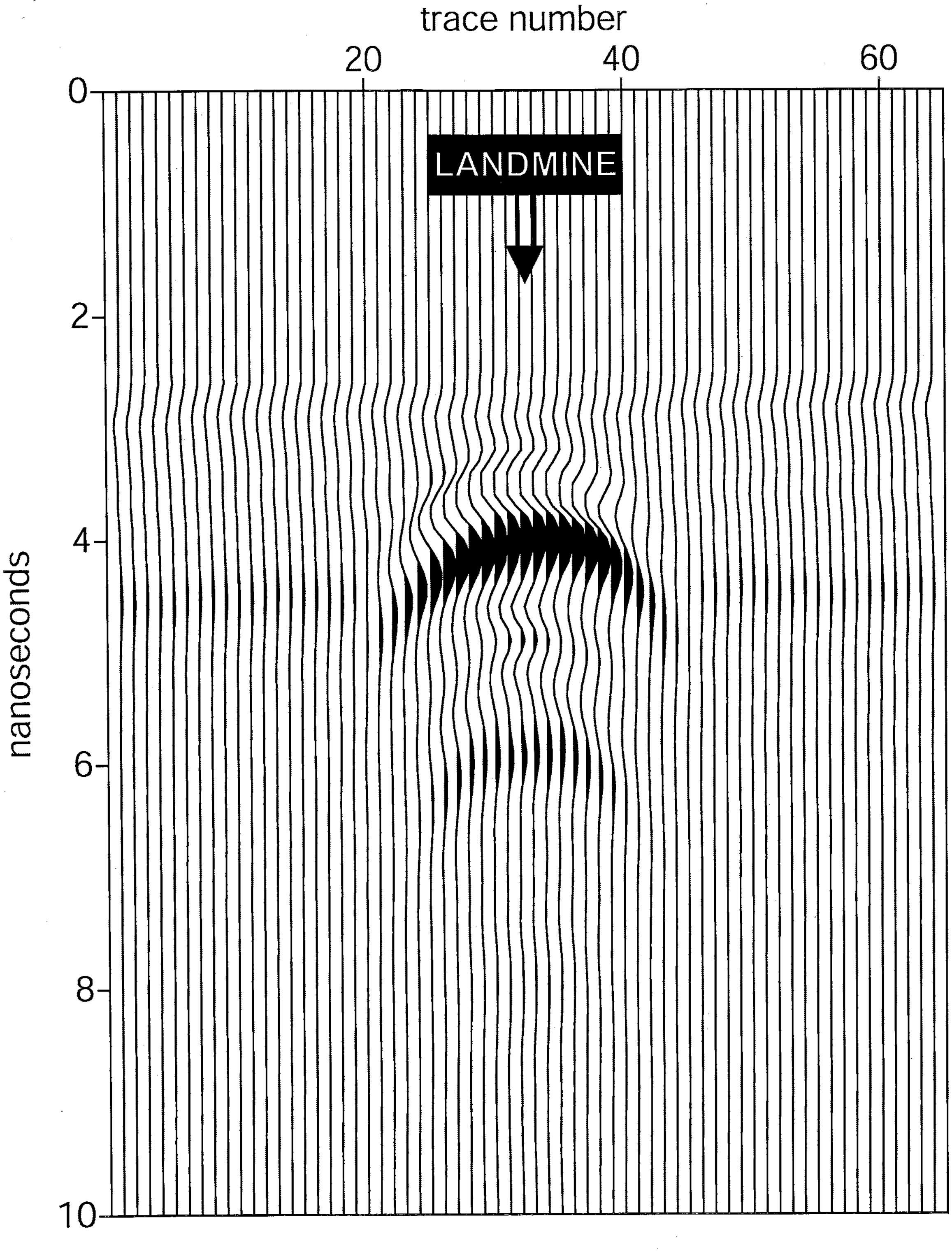

Figure 4.48 GPR profile of a M15 metallic antitank landmine buried 12.7 cm deep in sandy loam soil at 23% volumetric soil water content.

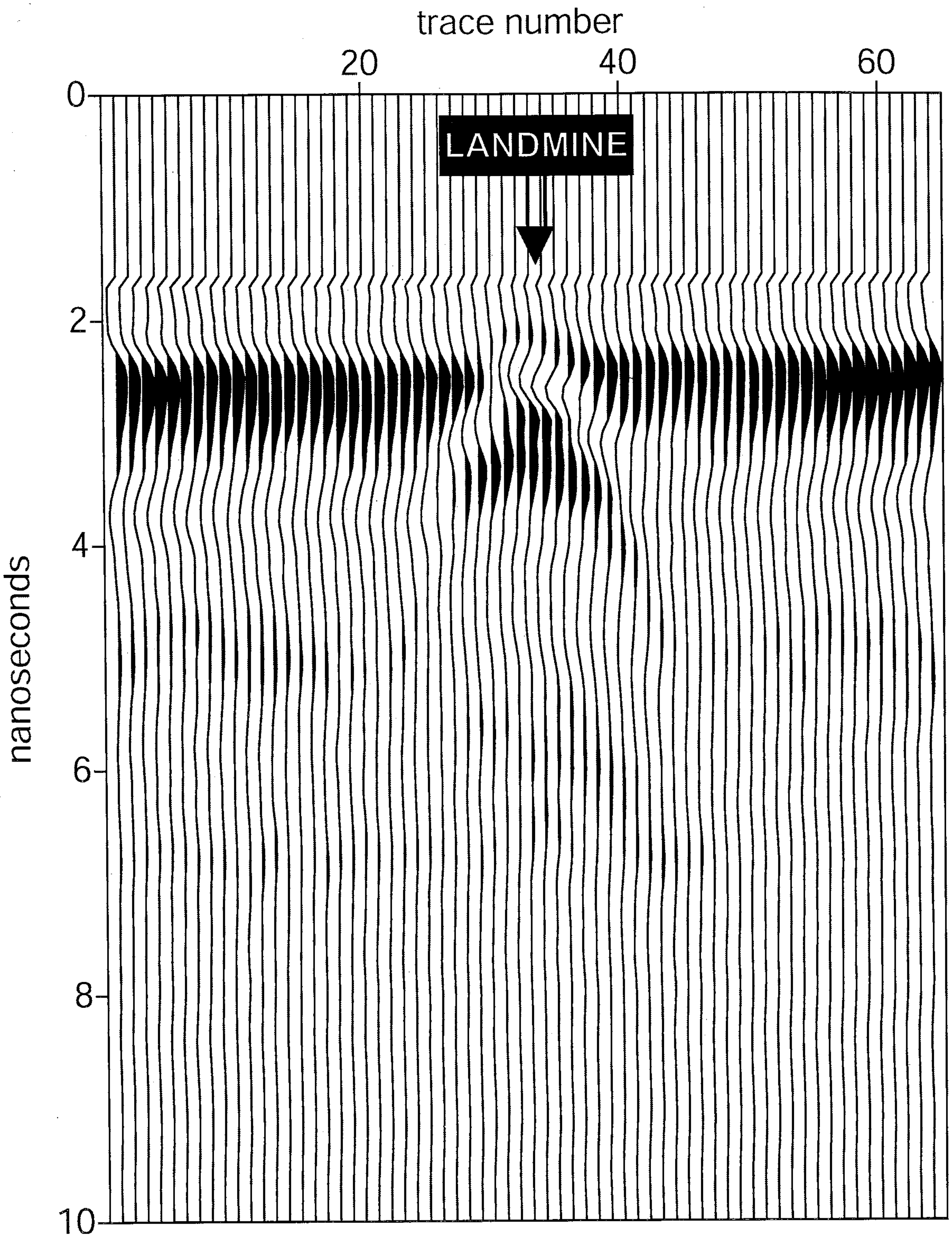

4.3 Comparisons Between TDR and GPR Measurements and the Peplinski Model Predictions

At each soil site where GPR was used to locate buried landmines, TDR probes were also installed to measure soil water content, as mentioned earlier. In this section the two-way travel time calculated from the dielectric constant measured with the TDR probes are compared with the two-way travel time from each GPR reflection. Table 4.1 shows this comparison. For most of the soils, the two-way travel times match very well, however there are some inconsistencies. These inconsistencies may be the result of heterogeneities in the soil and or difficulties in picking the correct arrival time from the GPR data. The first issue deals with the location of the TDR probes and the assumption that all the soil within the area, in some cases 10 m^2, was all uniform in composition and water content. The second issue deals with travel time estimates. Picking the correct travel time from the first arrivals was very difficult, so estimates of the travel time have an error of about ± 0.2 ns.

Table 4.2 shows the Peplinski model predictions for soil dielectric constants compared to the TDR measured value. The soil water content is also given in this table, and was calculated using Topp's equation (See Equation (2)). One important feature seen in Table 4.2 is the discrepancy between the Peplinski model and the TDR measured dielectric constant for the high sand soils, the Sevilleta sand, and the Yuma handheld soil. Both of these soils have more than 80% sand (See Figure 3.6). To model the dielectric constant of a soil, the Peplinski model uses the soil water content as an input. The soil water content used to calculate the dielectric constants seen in Table 4.2 was calculated

Table 4.1 **Comparisons of two-way travel times between field values measured with TDR and GPR. Travel times noted with (*) are uncertain because of large ground bounce.**

SOIL SITES	MINE TYPE	DEPTH TO MINE (CM)	ε TDR PROBE	TRAVEL TIME GPR (ns)	TRAVEL TIME TDR (ns)
Sevilleta Sand	NR26	11	4.7	2.7	2.1
	NR26	11	6.3	2.8	2.4
	NR26	10	16.1	3.3	3.5
Sevilleta Silt	NR26	11	5.4	2.2	2.2
	NR26	11	13.9	3.2	3.2
	NR26	11	23.9	4.1	4
Bosque Clay	NR26	11	3.8	2	1.9
	NR26	8	7.7	2*	2.5
	NR26	8	28.1	-	4.5
Yuma Handheld	VS-1.6	7.62	3.7	1.5	1.5
	VS-1.6	7.62	14.2	2.8	2.5
	VS-2.2	7.62	3.7	1.9	1.5
	VS-2.2	7.62	14.2	2.9	2.5
	TM62M	12.7	3.7	2.8	2.2
	TM62M	12.7	14.2	3.8	3.7
	TM62P3	7.62	3.7	2.5	1.5
	TM62P3	7.62	14.2	3	2.5
Yuma Vehicle	M19	7.62	4.2	1.9*	1.6
	M19	7.62	12.5	-	2.4
	M15	12.7	4.2	2.8	2.2
	M15	8	19.4	2.8	3.1

Table 4.2 **Comparsions between Peplinski model predictions for dielectric constants and TDR measured values.**

SOIL SITES	MINE TYPE	DEPTH TO MINE (CM)	WATER CONTENT	ε TDR PROBE	ε MODEL 900MHz
Sevilleta Sand	NR26	11	7%	4.7	9.6
	NR26	11	11%	6.3	13.1
	NR26	10	29%	16.1	29.3
Sevilleta Silt	NR26	11	9%	5.4	4.5
	NR26	11	26%	13.9	12.7
	NR26	11	38%	23.9	21.2
Bosque Clay	NR26	11	5%	3.8	3.9
	NR26	8	14%	7.7	7.6
	NR26	8	42%	28.1	26.9
Yuma Handheld	VS-1.6	7.62	5%	3.7	6.6
	VS-1.6	7.62	26%	14.2	23.5
	VS-2.2	7.62	5%	3.7	6.6
	VS-2.2	7.62	26%	14.2	23.5
	TM62M	12.7	5%	3.7	6.6
	TM62M	12.7	26%	14.2	23.5
	TM62P3	7.62	5%	3.7	6.6
	TM62P3	7.62	26%	14.2	23.5
Yuma Vehicle	M19	7.62	6%	4.2	6
	M19	7.62	22%	12.5	16.8
	M15	12.7	6%	4.2	6
	M15	8	23%	19.4	17.6

using Topp's equation, so it is hypothesized that Topp's equation may be estimating incorrect soil water contents for very sandy soils.

To test this hypothesis, Sung-Ho Hong (a New Mexico Tech student) carried out an experiment where fixed amounts of water were added to industrial sand (100% sand) and TDR measurements of the dielectric constant were taken at each soil water content level (See Table 4.3). From this experiment, it was determined that Topp's equation under predicts the true soil water content for sandy soils. So using Topp's equation to estimate the soil water content and then inputting this into the Peplinski model will lead to erroneous results. However, this under prediction in soil water content should lead to an under prediction in dielectric constant from the Peplinski model, since water content and dielectric constant are both directly proportional. The results in Table 4.2 show the Peplinski model over predicting the dielectric constant of sandy soil instead of the expected under prediction arrived at through this experiment. Table 4.3 also shows the values of the dielectric constant that the Peplinski model would predict given as inputs both the real soil water content and the water content predicted using Topp's equation. The dielectric constant predicted for soil water content is clearly higher than what is predicted for the Topp soil water content at every soil water content level. So from this we conclude that the Peplinski model is very inaccurate in predicting the dielectric constant of very sandy soils. This is indeed possible since Peplinski did not use soils with high sand contents to derive his model (Refer to Figure 1.1).

The next step was to compare the dielectric constant estimates from the GPR two-way travel times utilizing Equation (10) to estimate the dielectric constant of the soils and comparing these estimates with the measured TDR values. This comparison is seen in

Table 4.3 **Comparisons between soil water content measured volumetrically and calculated from TDR probes using Topp's equation (Equation (2)) for industrial sand (100% sand).**

WATER CONTENT (measured)	WATER CONTENT (Topp)	ε TDR PROBE	ε MODEL 900MHz (Topp)	ε MODEL 900MHz (measured)
3.9%	2.5%	2.83	5.65	7.02
4.6%	2.8%	2.93	5.95	7.68
7.8%	5.3%	3.91	8.34	10.7
9.1%	6.1%	4.22	9.08	11.8
11.7%	8.1%	5.06	10.9	14.2
13.7%	9.6%	5.67	12.3	16.0
15.7%	11.6%	6.54	14.1	17.9
18.2%	14.2%	7.73	16.4	20.1
19.6%	15.0%	8.09	17.2	21.4
23.5%	18.4%	9.8	20.3	25.0
27.4%	22.4%	11.92	24	28.6
28.1%	23.1%	12.36	24.6	29.3
31.3%	28.9%	15.85	30	32.2
35.1%	29.2%	16.07	30.2	35.8
42.2%	38.4%	23.41	38.9	42.5

Table 4.4. These values do not match well. Figure 4.49 provides an explanation to this problem. In this figure, it is shown that small variances in the two-way travel time produce large variances in the dielectric constant estimate. Take for example the case where the two-way travel time is estimated as 3.6 ns, estimated from trace inspection on the radar image, now if the reflection is at 3.8 ns then the dielectric constant will be 15 but if the travel time is 3.4 it will produce a dielectric constant of about 20. Small errors in the travel time are inherent in first arrival estimates from radar images and seismograms, so this is most likely what is causing the discrepancies seen in Table 4.3.

Table 4.4 **Comparisons between GPR estimates for dielectric constant and TDR measured values.**

SOIL SITES	MINE TYPE	DEPTH TO MINE (CM)	WATER CONTENT	ε TDR PROBE	ε GPR 900MHz
Sevilleta Sand	NR26	11	7%	4.7	8.7
	NR26	11	11%	6.3	9.5
	NR26	10	29%	16.1	16.8
Sevilleta Silt	NR26	11	9%	5.4	5.3
	NR26	11	26%	13.9	13
	NR26	11	38%	23.9	23.2
Bosque Clay	NR26	11	5%	3.8	4.1
	NR26	8	14%	7.7	7.4
	NR26	8	42%	28.1	-
Yuma Handheld	VS-1.6	7.62	5%	3.7	3.6
	VS-1.6	7.62	26%	14.2	19
	VS-2.2	7.62	5%	3.7	7
	VS-2.2	7.62	26%	14.2	20.8
	TM62M	12.7	5%	3.7	7.3
	TM62M	12.7	26%	14.2	14.8
	TM62P3	7.62	5%	3.7	14.3
	TM62P3	7.62	26%	14.2	22.6
Yuma Vehicle	M19	7.62	6%	4.2	22.6
	M19	7.62	22%	12.5	-
	M15	12.7	6%	4.2	7.3
	M15	8	23%	19.4	18.9

Figure 4.49 **How uncertainty in GPR two-way travel time greatly affects the dielectric constant estimate of soils. Equation (10) was used to generate this plot.**

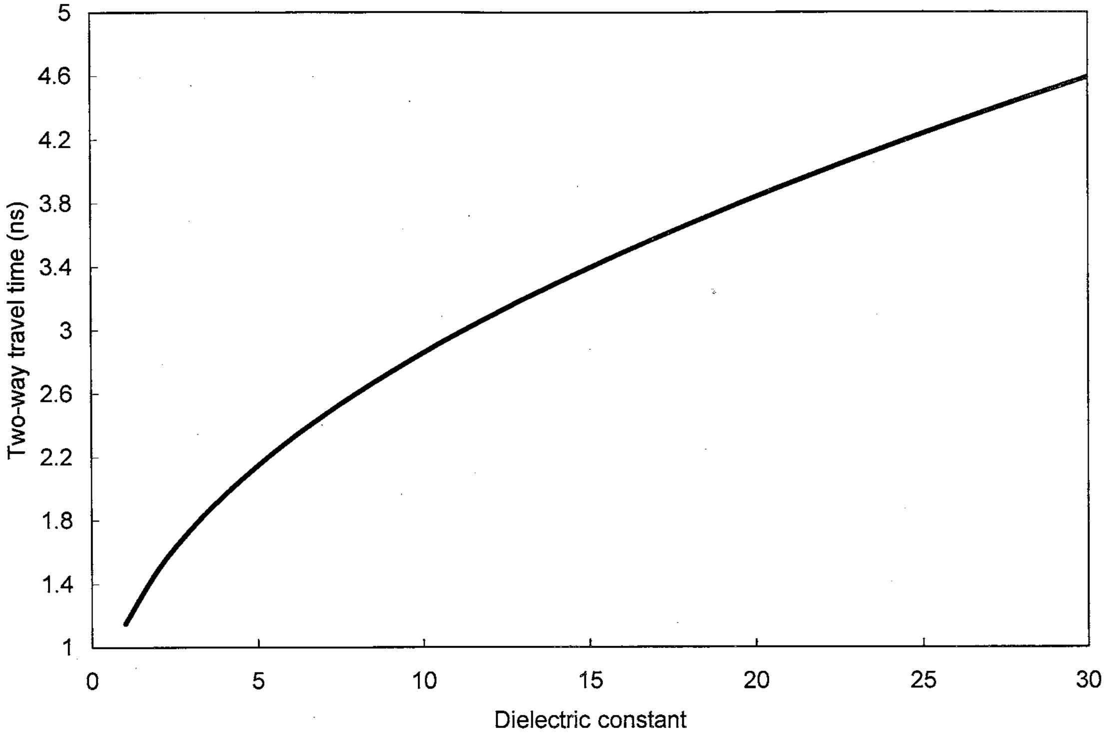

5 – CONCLUSIONS

The main goal of this study was to test the ability of ground penetrating radar to locate buried antitank landmines in field soils at varying levels of soil water content. To accomplish this, the expected response of the radar system was predicted using semi-empirical equations from the literature. Then a ground penetrating radar system was tested in various field soils and at various soil water conditions with a diversity of real and simulant antitank landmines. My work has led to the following conclusions:

Model Conclusions

- In sand and silt soils, over the 900 MHz frequency range, the Peplinski model predicts that the real part of the dielectric constant will increase rapidly as the soil water content is increased. In addition, the total attenuation for these types of soils is relatively low. This suggests that for these soils there will be enough dielectric contrast between the landmine and the soil at elevated soil water conditions to detect landmines. It also suggests that the attenuation will be low in these soils which will not hinder detection of landmines.
- In clay soils at 900 MHz, the real part of the dielectric constant increases rapidly as the soil water content is increased from dry soil to saturated soil. However, the total attenuation in clay soils is very large, approaching 65 db/m at 40% soil water content. This suggests that landmine detection will not improve at elevated soil water conditions in this type of soil due to the large amount of attenuation.

- The Peplinski model appears to be predicting consistent values for dielectric constants of the silt and clay soils when compared with TDR measurements, but tends to over predict the dielectric constants of very sandy soils.
- Topp's equation relating soil water content to measured dielectric constant appears to be under predicting the soil water content for very sandy soils.

GPR Conclusions

- GPR profiles of buried simulant nonmetallic antitank landmines in sandy and silty soils at 900 MHz become clearer as the soil water content is increased to saturation.
- GPR profiles of buried simulant nonmetallic antitank landmines in clay soils at 900 MHz do not become clearer as the soil water content is increased to saturation.
- GPR profiles of buried simulant nonmetallic antitank landmines taken in saline water saturated sandy soils at 900 MHz show that images tend to degenerate as the salinity of the pore fluid is increased. Evidence also shows that after these soils dry, the simulant landmine is again detectable.
- GPR profiles of buried metallic antitank landmines in sandy and silty soils at 900 MHz do not become clearer as the soil water content is increased to saturation.
- There is good agreement between GPR and TDR measurements of two-way travel time.

6 – FUTURE WORK

In this research it was found that a limiting factor was not knowing the variability of the soil water content within the entire test area. We took point measurements of the soil water content above and below the observation landmine located approximately 1.5 meters from the target landmine; however, it would have been more useful if the soil water content was measured at more then one place inside the test area. Further, it would have also helped if the soil water content was continuously measured with some type of data logger setup instead of the single point measurements.

Future work could include more GPR images taken at a wider range of soil water conditions. Our work consisted of taking GPR images at dry, intermediate and saturated soil water conditions and this validated our general hypothesis about the enhancement of image quality; however, an improved study could be done where a GPR image is taken at increments of 5% water content up to saturation.

From our work we found that the Peplinski model over predicts the complex dielectric constant of very sandy soils (greater than 80% sand), so this model needs to be recalibrated for these types of soils. This type of work would consist of dielectric measurements of sandy soils over a range of soil water contents and then adjustments could be made to the empirical equations used in the Peplinski model.

7 - REFERENCES

J. G. Ackenhusen, Q. A. Holmes, K. Colin, and J. A. Wright, "IRIA State of the Art Reports: Detection of Mines and Minefields," Infrared Information Analysis Center, Ann Arbor, MI, Nov. 2001.

A.P. Annan, "Ground Penetrating Radar Workshop Notes," Sensors & Software Inc., Mississauga, ON, Sept. 2001.

B. Borchers, J. M. H. Hendrickx, and B. S. Das, "Modeling Distributions of Water and Dielectric Constants Around Landmines in Homogeneous Soils," in *Proc. SPIE*, vol. 3710, pp. 728-738, 1999.

B. Borchers, J. M. H. Hendrickx, B. S. Das, and S. Hong, "Enhancing dielectric contrast between landmines and the soil environment by watering: modeling, design, and experimental results," in *Proc. SPIE*, vol. 4038, pp. 993-1000, 2000.

J. B. Campbell, *Introduction to Remote Sensing*. New York: Guilford Press, 1996.

B. S. Das, J. M. H. Hendrickx, and B. Borchers, "Modeling transient water distributions around landmines in bare soils," *Soil Science*, vol. 166~No. 3, pp. 163-173, Mar. 2001.

J.L. Davis, and A.P. Annan, "Ground-penetrating radar for high-resolution mapping of soil and rock stratigraphy," *Geophysical Prospecting*, vol. 37, pp. 531-551, 1989.

M. C. Dobson, F. T. Ulaby, , M. T. Hallikainen, , and M. A. El-rayes, "Microwave Dielectric Behavior of Wet Soil-Part II: Dielectric Mixing Models," *IEEE Trans. Geosci. Remote Sensing*, vol. GE-23, pp. 35-46, 1985.

M. Fritzsche, "Detection of buried landmines using ground penetrating radar," in *Proc. SPIE*, vol. 2496, pp. 100-109, 1995.

M. T. Hallikainen, F. T. Ulaby, M. C. Dobson, M. A. El-rayes, and L.Wu, "Microwave Dielectric Behavior of Wet Soil-Part I: Empirical Models and Experimental Observations," *IEEE Trans. Geosci. Remote Sensing*, vol. GE-23, pp. 25-32, 1985.

J.M.H. Hendrickx, P.J. Wierenga, and M.S. Nash, "Variability of soil water tension and soil water content," *Agricultural Water Management*, vol. 18, pp. 135-148, 1990.

D. Hillel, *Environmental Soil Physics*. San Diego, CA: Academic Press, 1998.
J. E. Hipp, "Soil Electromagnetic Parameters as Functions of Frequency, Soil Density, and Soil Moisture," in *Proc. IEEE*, vol. 62~No. 1, pp.98-103, 1995.

P. Hoekstra, and A. Delaney, " Dielectric Properties of Soils at UHF and Microwave Frequencies," *Journal of Geophysical Research*, vol. 79~No. 11, pp.1699-1708, 1974.

P.G. Johnson, and P. Howard, "Performance results of the EG&G vehicle mounted mine detector," in *Proc. SPIE*, vol. 3710, pp. 1149-1159, 1999.

W. A. Jury, W. R. Gardener, W. H. Gardener, *Soil Physics*. New York: Wiley, 1991.

Koh, Gary, "Ultra-wideband FMCW radar for detection of anti-personnel mines buried at shallow depth," in *Proc. SPIE*, vol. 4038, pp. 976-982, 2000.

A. Klute, "Methods of Soil Analysis - Part 1 Physical and Mineralogical Methods," 2nd ed., Agronomy Monograph No. 9, *Soil Science Society of America*, Madison, WI, 1986.

D. Langmuir, *Aqueous Environmental Geochemistry*. Upper Saddle River, New Jersey: Prentice Hall, 1997.

J. K. Mitchell, *Fundamentals of Soil Behavior*. New York: Wiley, 1976.

M. N. Nabighian, "Electromagnetic methods in applied geophysics," vol. 1, Tulsa: Society of Exploration Geophysicists, pp. 131-311, 1987.

N. R. Peplinski, F. T. Ulaby, M. C. Dobson, "Dielectric Properties of Soils in the 0.3-1.3-GHz Range," *IEEE Trans. Geosci. Remote Sensing*, vol. 33~No. 3, pp. 803-807, 1995.

J. M. Reynolds, *An Introduction to Applied and Environmental Geophysics*. Chichester, England: Wiley, pp.682-749, 1997.

B. Scheers, M. Acheroy, and V. A. Vorst. "Time domain modeling of UWB GPR and its application on landmine detection," in *Proc. SPIE*, vol. 4038, pp. 1452-1460, 2000.

Sensors & Software, "pulseEkko 1000 RUN-User's Guide," Version 1.2, Sensors & Software Inc., Mississauga, Canada, 1996.

J. W. Stockwell, and J. K. Cohen, "Seismic Unix User's Manual," Version 3.0, Colorado School of Mines, Golden, CO, 2001.

Tektronix, "Tektronix metallic TDR's for cable testing -- Application note," Tektronix Inc., Beaverton, Oregon, 1987.

G. C. Topp, J. L. Davis, A.P. Annan, "Electromagnetic Determination of Soil Water Content: Measurements in Coaxial Transmission Lines," *Water Resources Research*, vol. 16, pp. 574-582, 1980.

A.H. Trang, “Simulation of mine detection over dry soil, snow, ice, and water,” in *Proc. SPIE*, vol. 2765, pp. 430-440, 1996.

F. T. Ulaby, R. K. Moore, and A. K. Fung, “Microwave remote sensing : active and passive,” vol. 3, Dedham, MA: Artech House, 1986.

US Department of State, “Hidden Killers: The Global Landmine Crisis,” *Dep. of State Publication 10225*, Dec. 1994.

J. R. Wang, and T. J. Schmugge, “An Empirical Model for the Complex Dielectric Permittivity of Soils as a Function of Water Content,” *IEEE Trans. Geosci. Remote Sensing*, vol.GE-18~No. 4, pp. 288-295, 1980.

D. Wobschall, “A theory of the complex dielectric permittivity of soil containing water, the semidisperse model,” *IEEE Trans. Geosci. Electron.*, vol. 15, pp. 49-58, 1977.

D . F. Zoldoske, K. H. Solomon, and E. M. Norum, “Uniformity Measurements for Turfgrass: What's Best?,” California State University, Fresno, CA, November 1994.

This thesis is accepted on behalf of the
Faculty of the Institute by the following committee:

Hendricks

Advisor

Brian Borchers

Robert S. Bowman

8/16/02

Date

I release this document to the New Mexico Institute of Mining and Technology.

Timothy W. Miller 8/16/02

Student's Signature Date